Roles of the Lenses

Gun Lens

Helps form probe

Condenser Lens

Mainly controls:
Spot Size
hence total beam current

Objective Lens

Mainly controls focus

Diffraction/Intermediate Lens

Controls Mode

Projector Lens

Magnification

Most TEM/STEM have 7-8 Lenses

2 Condensers
1 Objective
1-2 Intermediate
2 Projectors

Most instruments have only Electromagnetic Round Lenses

Note the locations of the various Apertures.

Optimum aperture sizes are needed for various imaging functions.

Transmission Electron Microscopy

Conventional Imaging

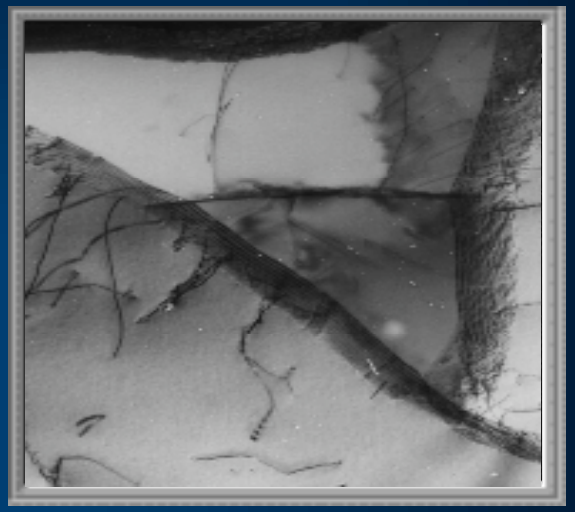

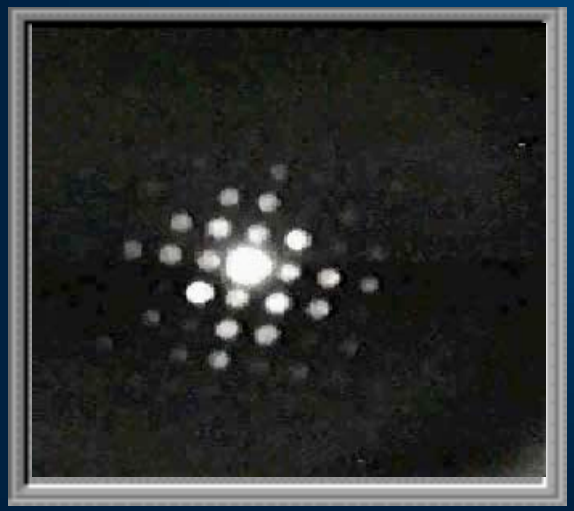

High Resolution Imaging

Diffraction

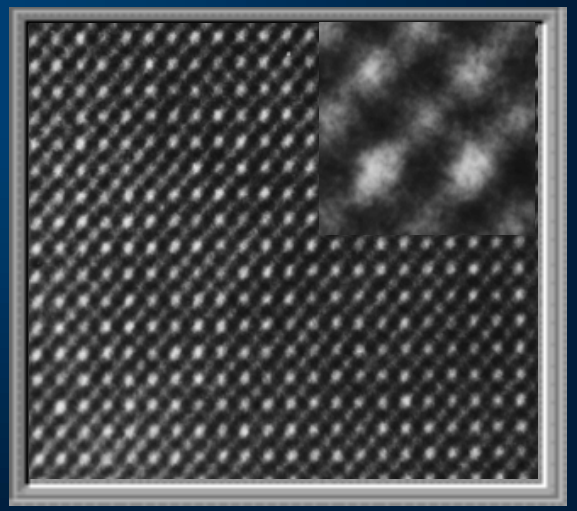

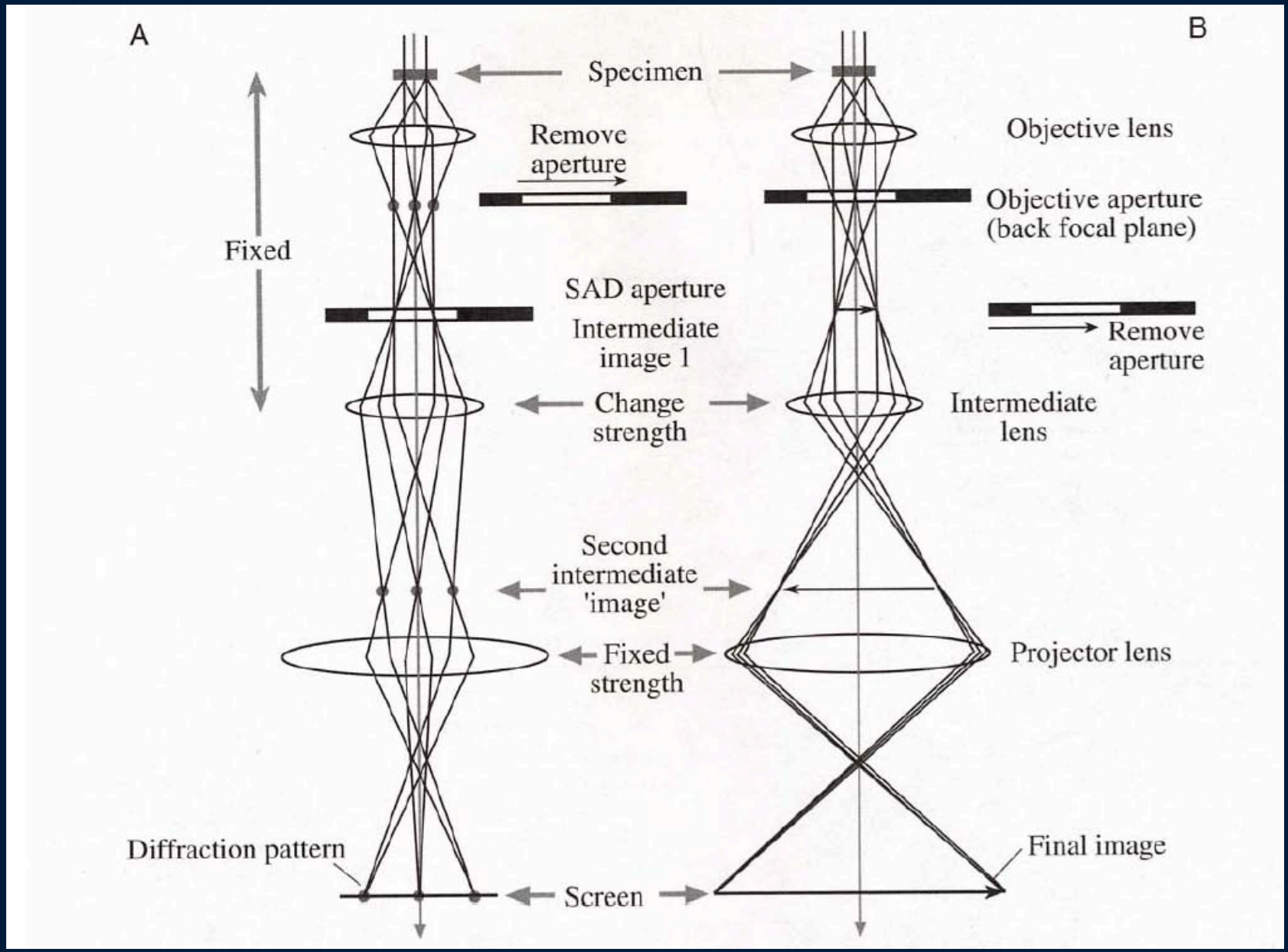
A
B
Specimen
Remove aperture
Objective lens
Objective aperture (back focal plane)
Fixed
SAD aperture
Intermediate image 1
Remove aperture
Change strength
Intermediate lens
Second intermediate 'image'
Fixed strength
Projector lens
Diffraction pattern
Screen
Final image

Major Factors affecting TEM Image Contrast

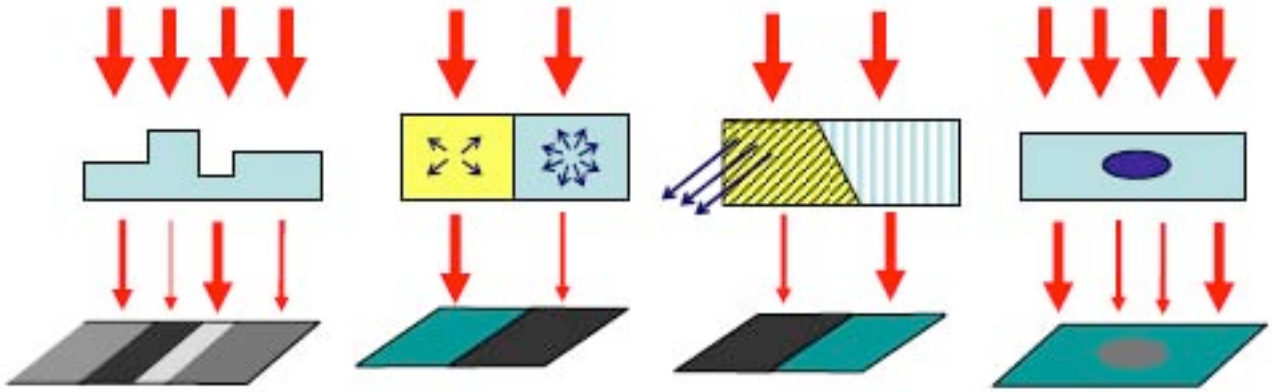

Thickness	Atomic number	Orientation	Defects
Scattering	*Scattering*	*Diffraction*	*Scattering & diffraction*

Contrast in the TEM

- Mass contrast
  - Varying mass of sample attenuates the beam differently.
- Diffraction contrast
  - Bragg scattered beams are removed.
- Phase contrast
  - Bragg scattered beams interfere with each other.

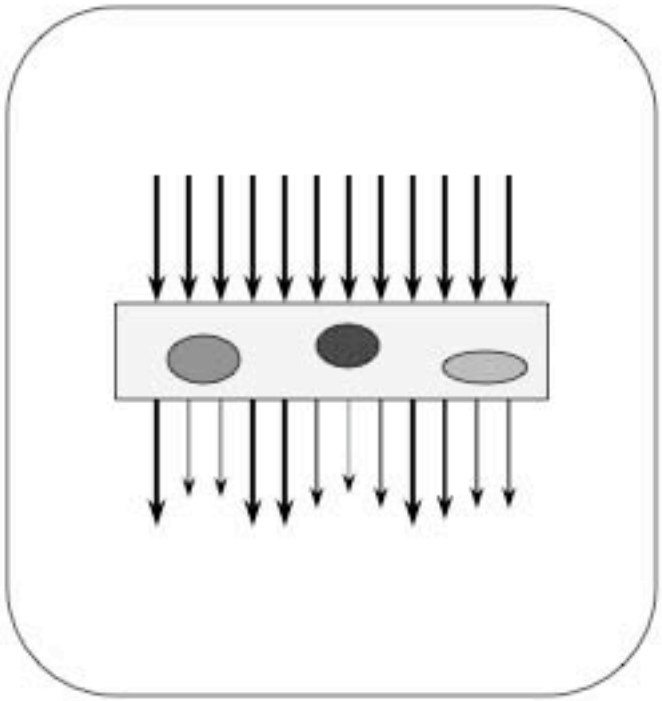

Elastic Scattered Intensity

Amorphous Solids:

$$I(\theta) \sim |f(\theta)|^2 \cdot \left\{1 + \frac{\sin(kR)}{kR}\right\}$$

$$k = \frac{4\pi}{\lambda}\sin(\theta)$$

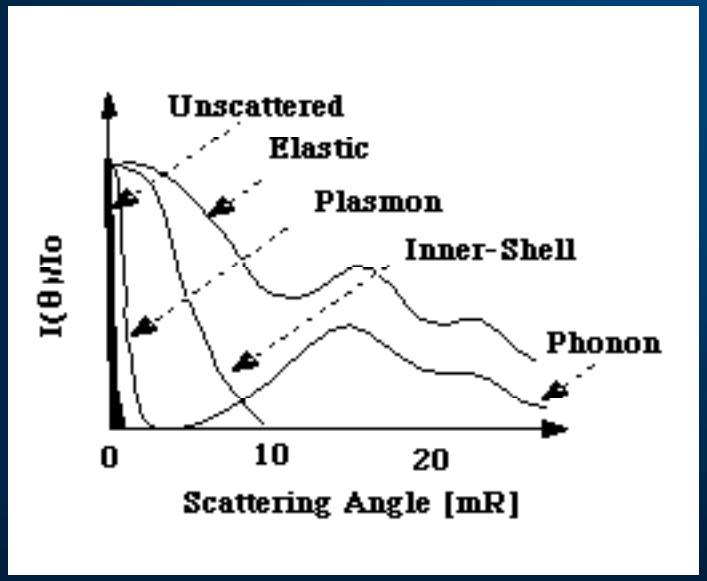

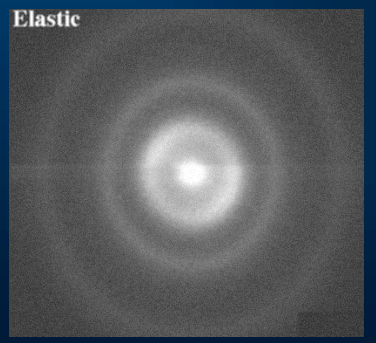

Mass-Thickness Contrast

- This is the most important type of contrast for biological specimen imaging. In particular, for imaging non-crystalline materials such as tissues, cells, and polymers.
- It is expected that high-Z (i.e., high-mass) regions of a specimen scatter more electrons than low-Z regions of the same thickness.
- Similarly, thicker regions will scatter more electrons than thinner regions of the same average Z, all other factors being constant.
- Therefore, for the case of a BF image, thicker and/or higher-mass areas will appear darker than thinner and/or lower-mass areas. The reverse will be true for DF image.

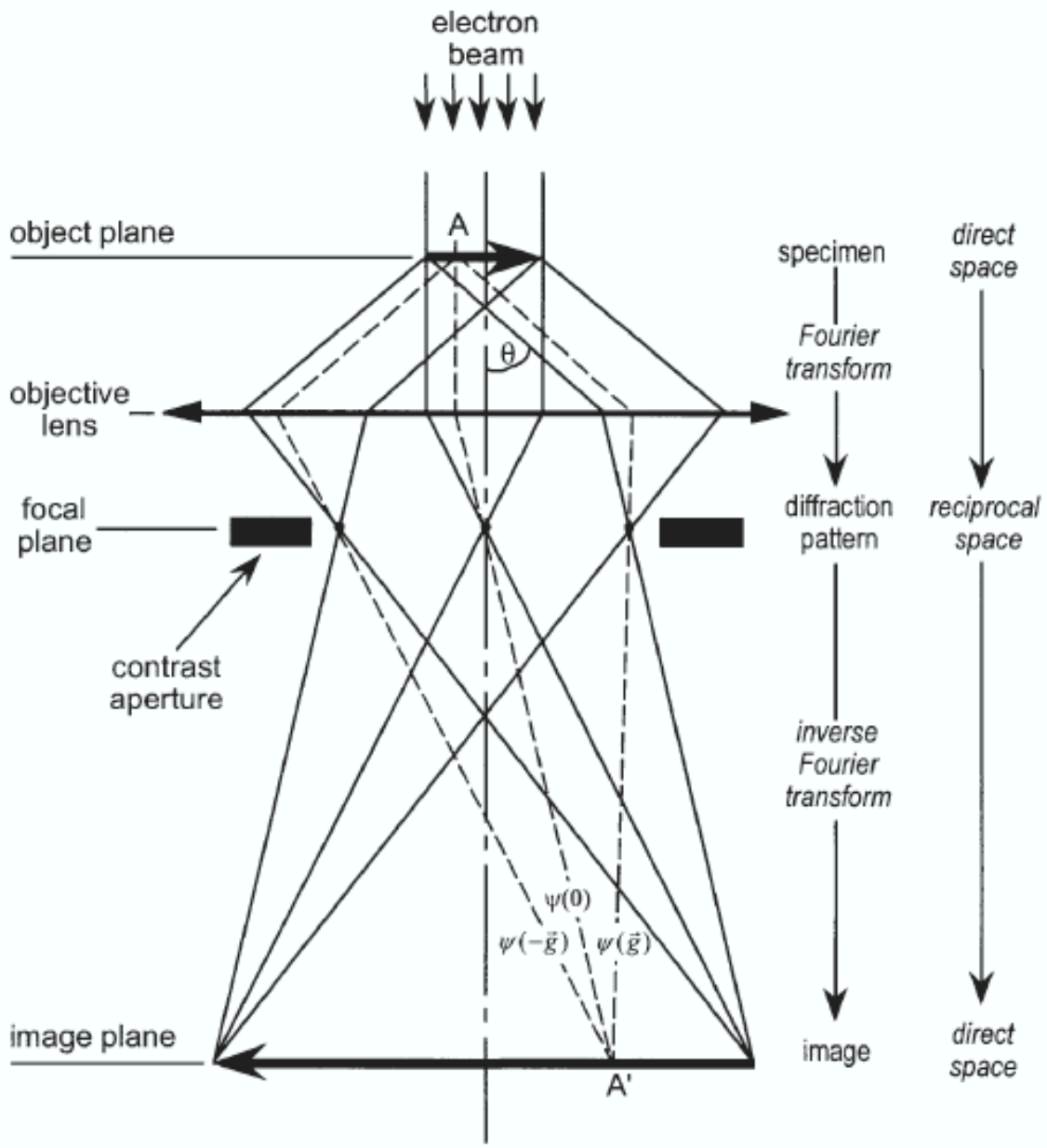
electron
beam
object plane
A
specimen
direct
space
Fourier
transform
θ
objective
lens
focal
plane
diffraction
pattern
reciprocal
space
contrast
aperture
inverse
Fourier
transform
ψ(0)
ψ(−g⃗)
ψ(g⃗)
image plane
image
direct
space
A'

$$\nabla^2\phi + \frac{8\pi^2 m}{h^2}(E + eV_0)\phi = 0$$

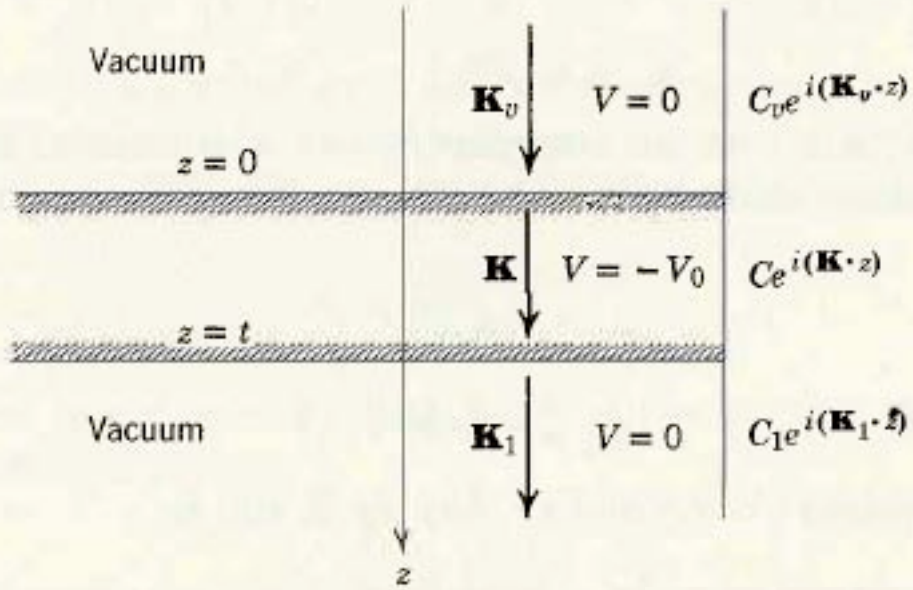

$$\phi_v = C_v e^{i(\mathbf{K}_v \cdot \mathbf{r})}$$

$$\phi_1 = C_v e^{i\mathbf{K}_v z} e^{i(\pi V_0 / \lambda V_a)t} e^{-(Q/2)t}$$

$$\phi_1 \phi_1^* = |C_v|^2 e^{-Qt}$$

$$I = I_0 e^{-Qt}$$

Amplitude Contrast - in the unscattered beam

Positive Staining

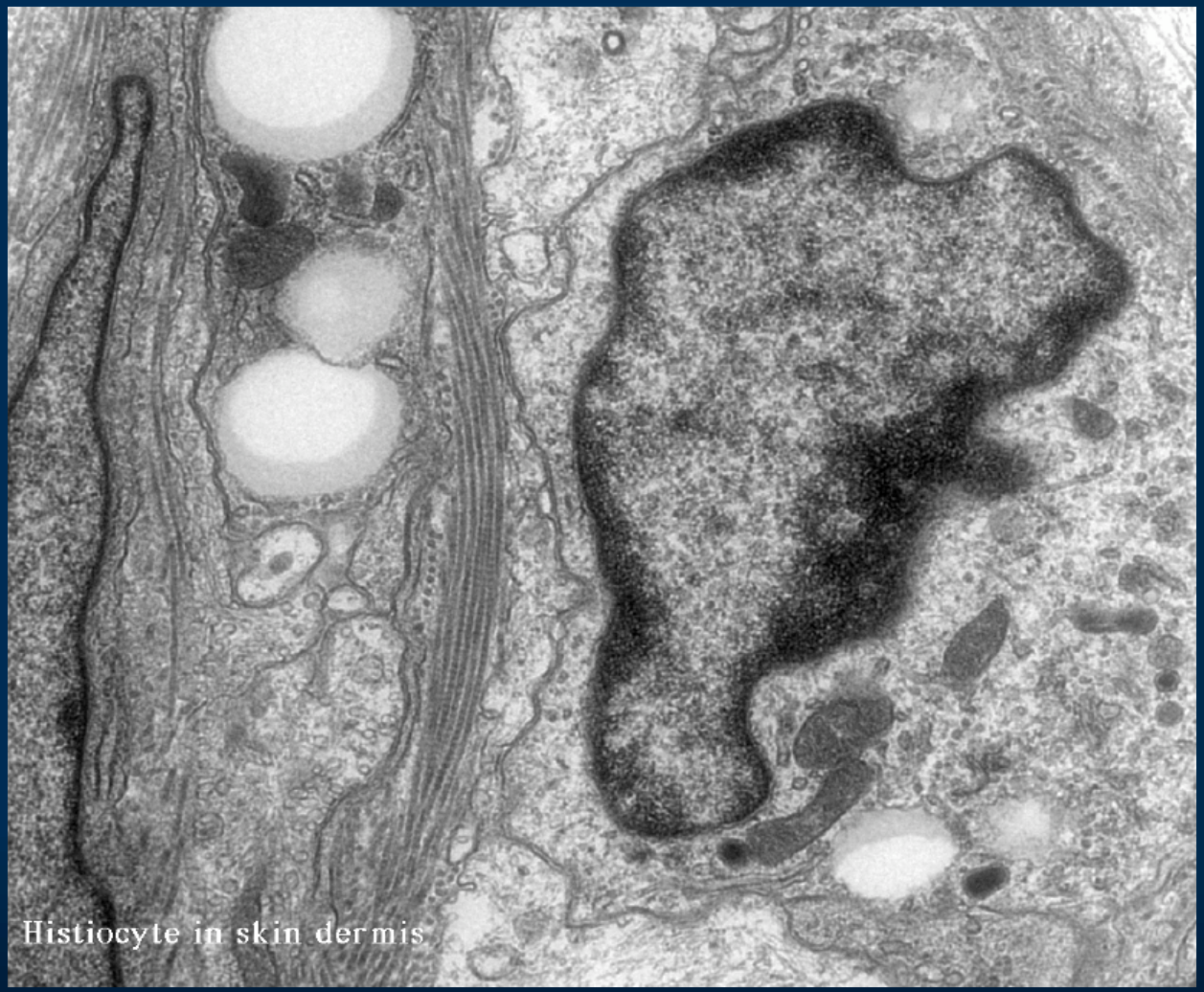

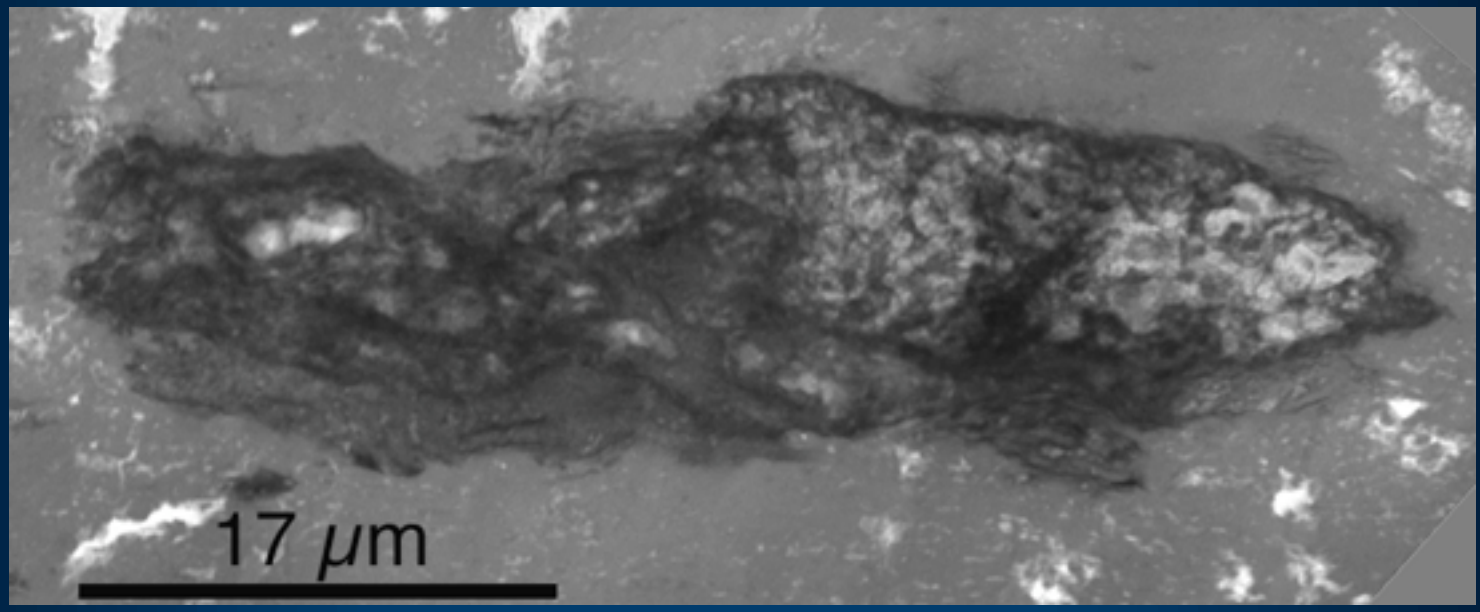
17 μm

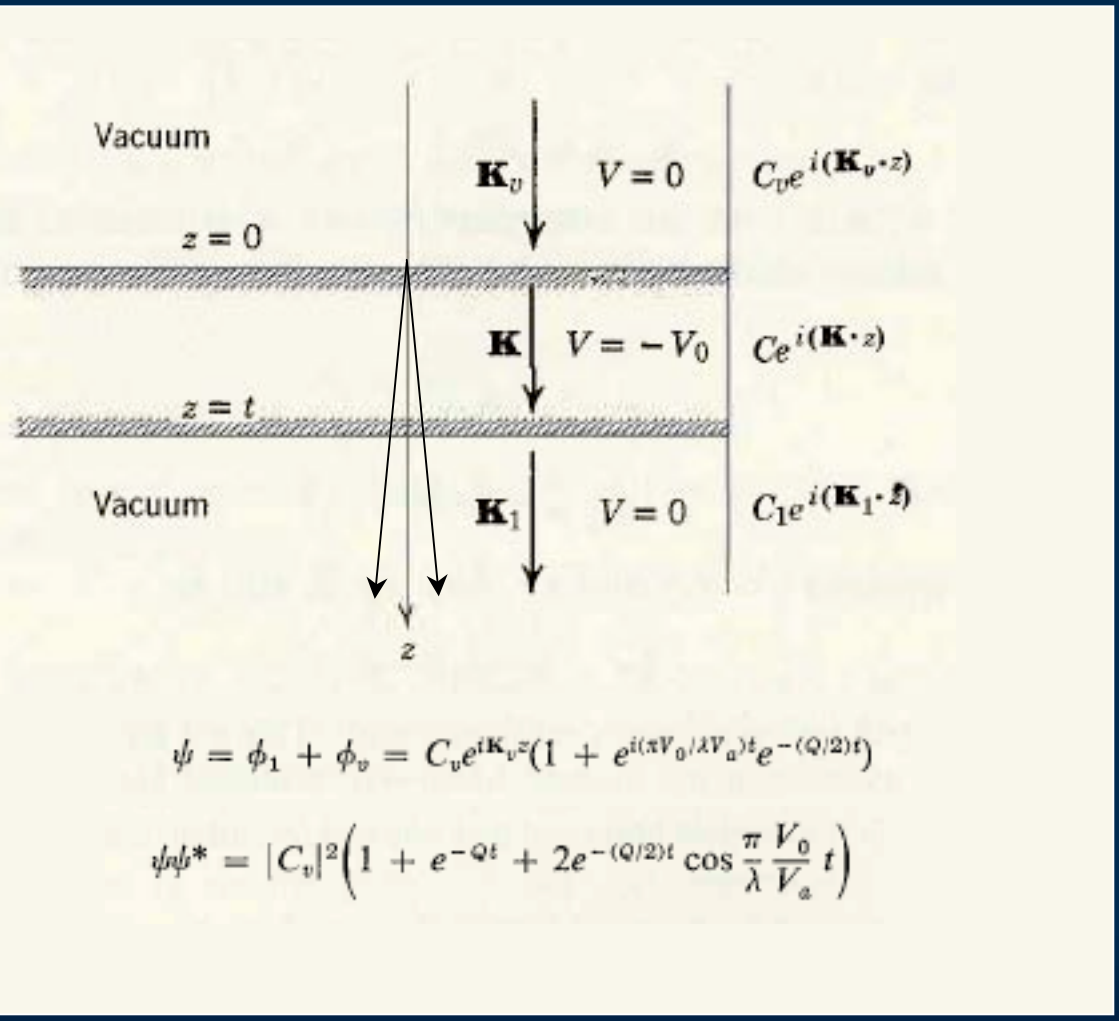

$$\psi = \phi_1 + \phi_v = C_v e^{i\mathbf{K}_v z}(1 + e^{i(\pi V_0/\lambda V_a)t} e^{-(Q/2)t})$$

$$\psi\psi^* = |C_v|^2\left(1 + e^{-Qt} + 2e^{-(Q/2)t} \cos \frac{\pi}{\lambda}\frac{V_0}{V_a} t\right)$$

Phase Contrast results from interference with a scattered wave

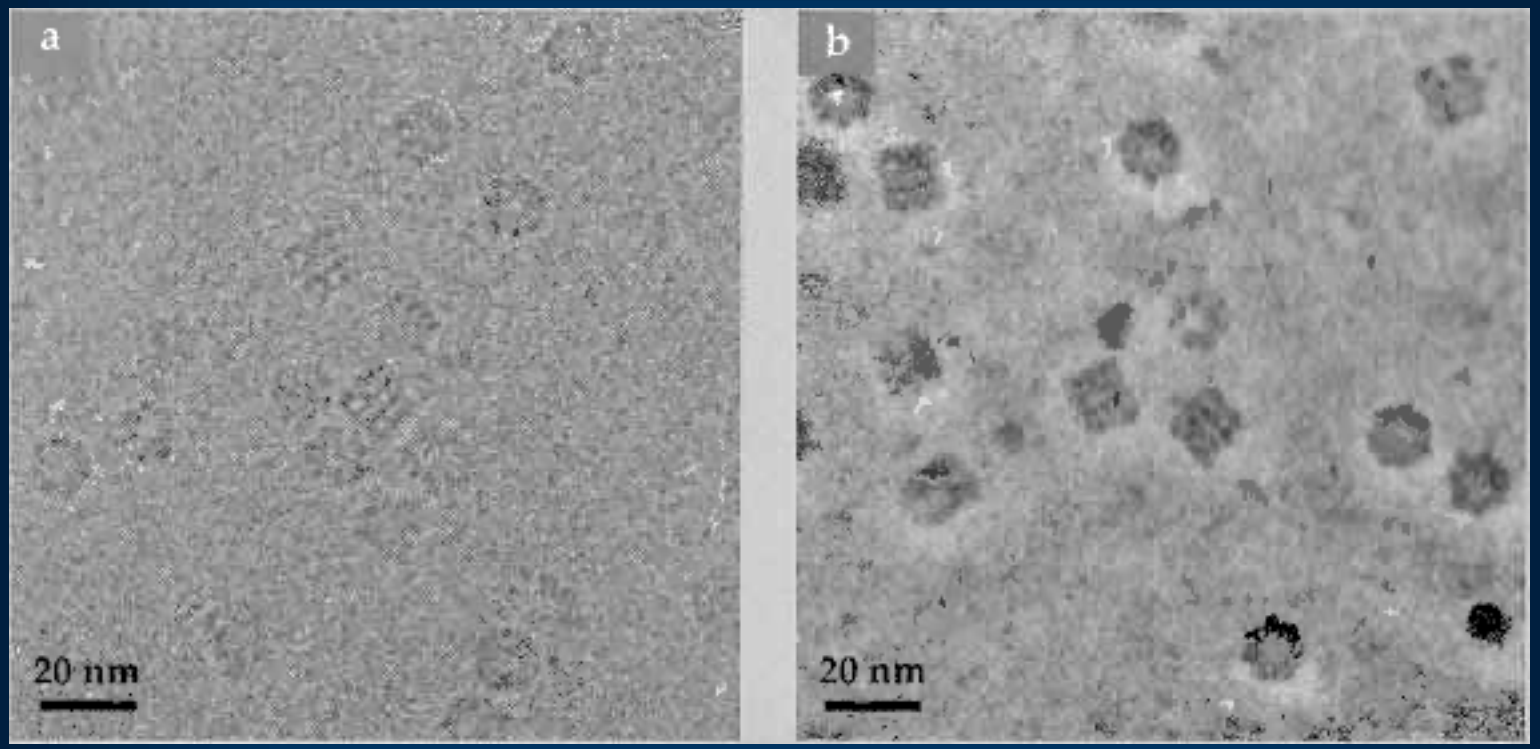

Mainly Amplitude Contrast

Contrast Enhanced
With Phase Contrast

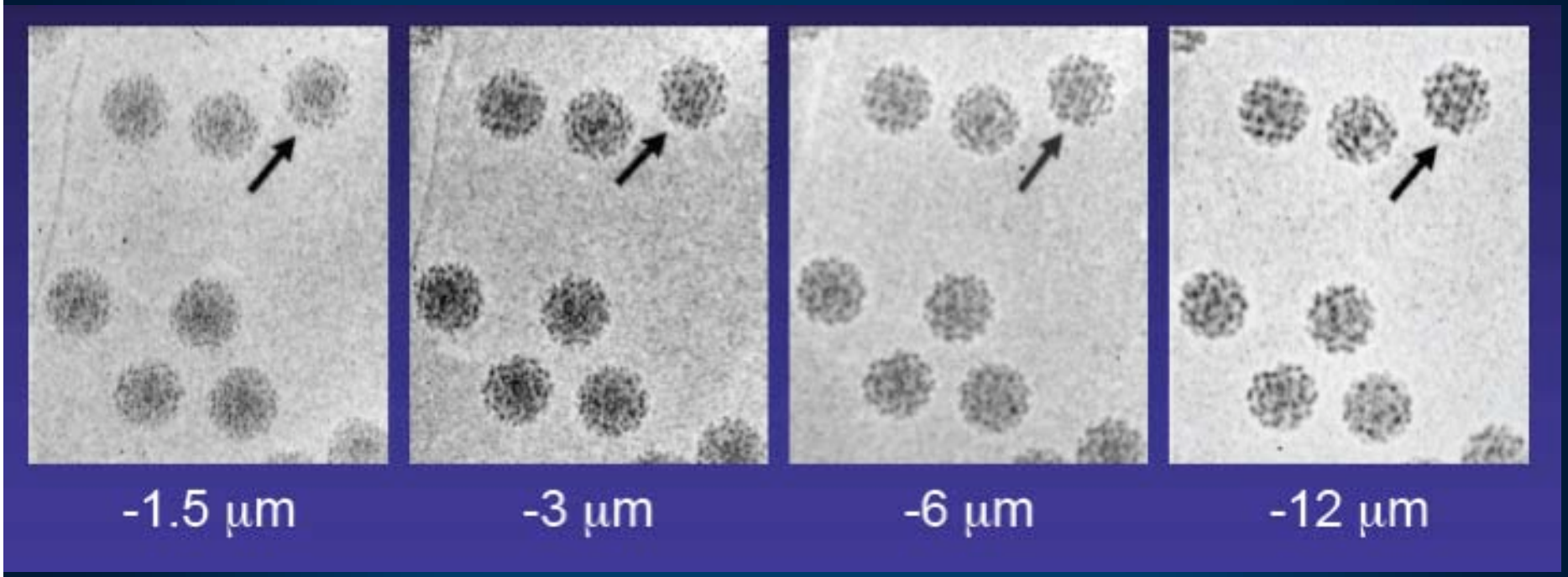

Phase Contrast is Increased by defocusing
But the “image resolution” degrades due to Fresnel Diffraction

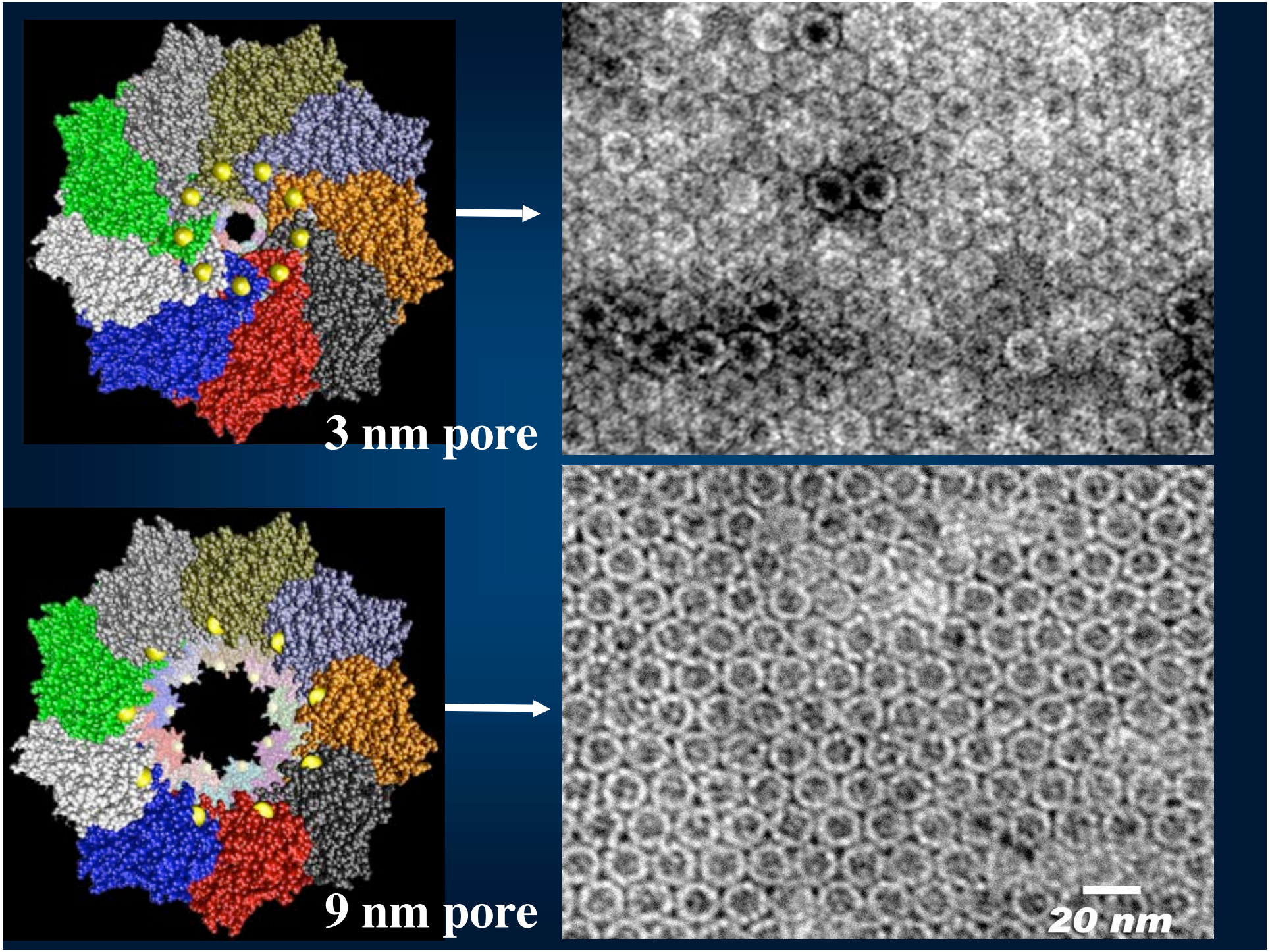
3 nm pore
9 nm pore
20 nm

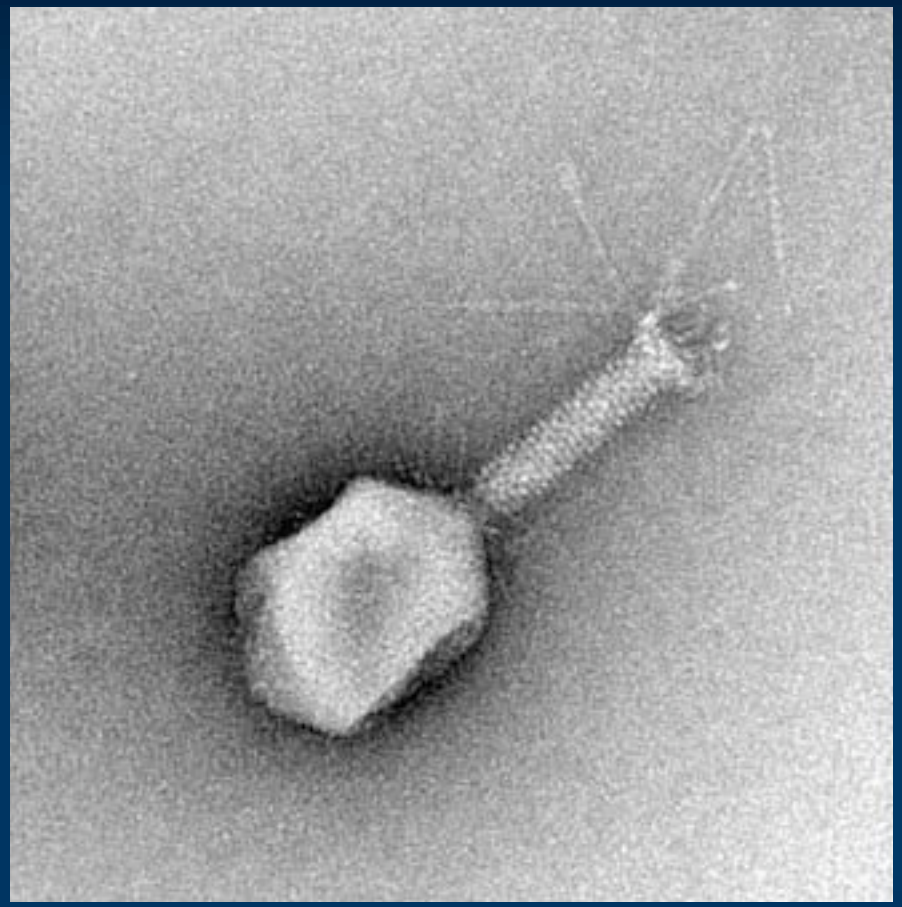

T4 Bacteriophage

www.physicstoday.org
physics today
January 2008

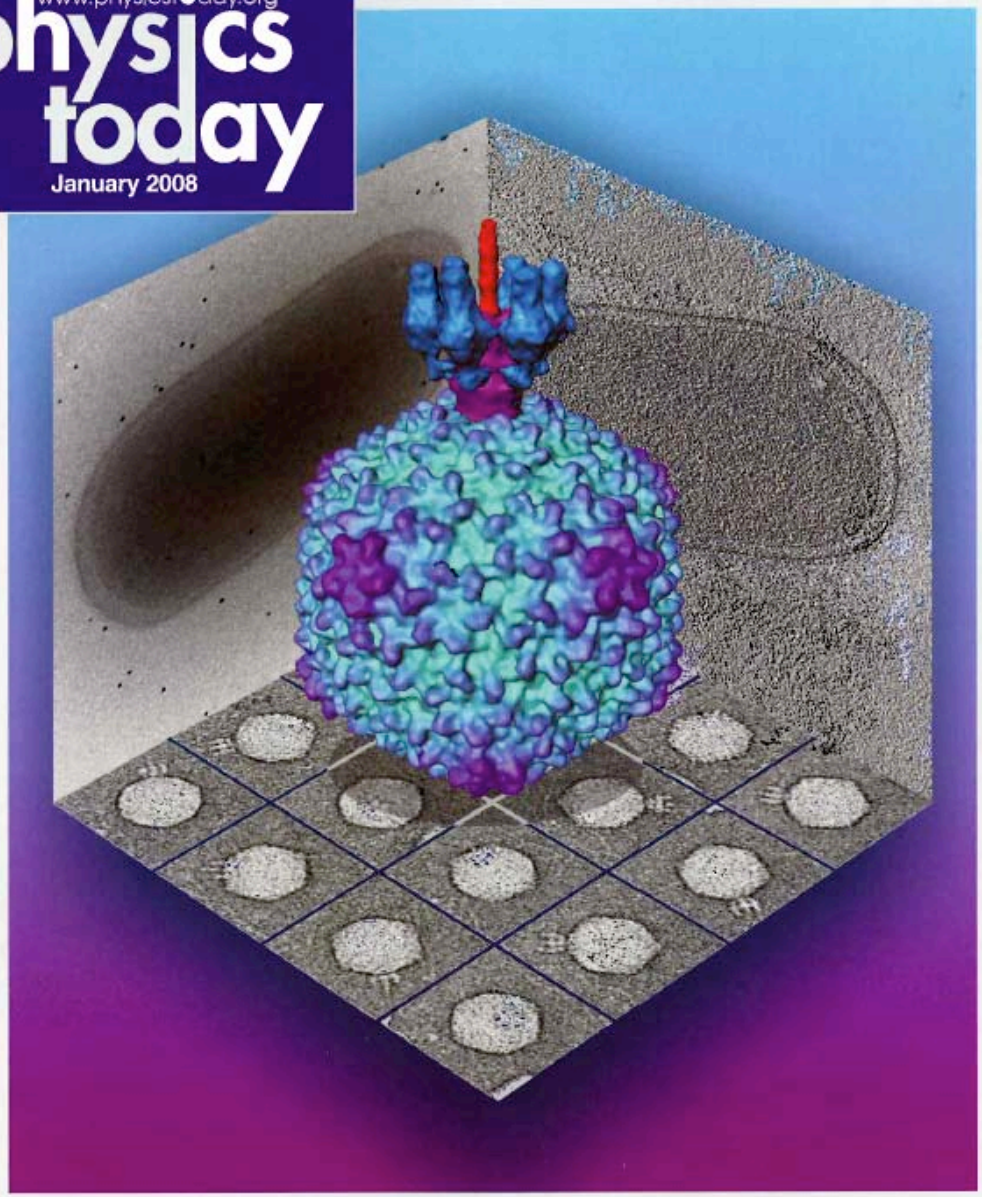

Electron Cryo-Microscopy

Other Methods: Negative Staining

Paramecium bursaria Chlorella virus

Stained with Uranyl acetate

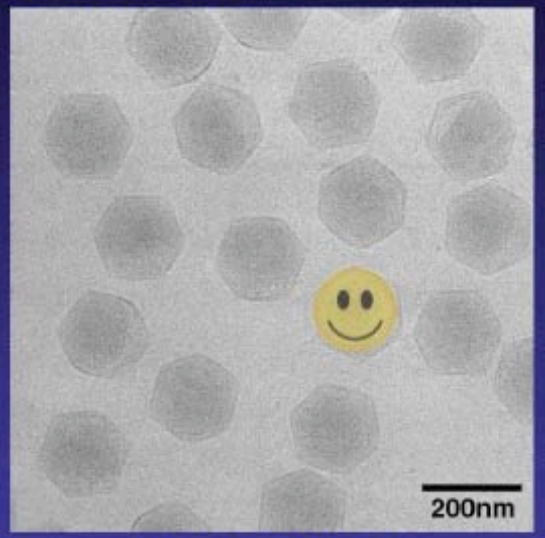

Unstained, vitrified

- Staining is often unpredictable and uneven
- Contrast is high but primarily highlights solvent-accessible surfaces
- Sample flattening occurs owing to dehydration
- Stain redistributes/crystallizes under influence of electron beam
- Different stains can give different appearances

Feb 2007

Electron Cryo-Microscopy

Blotting and Plunge Freezing

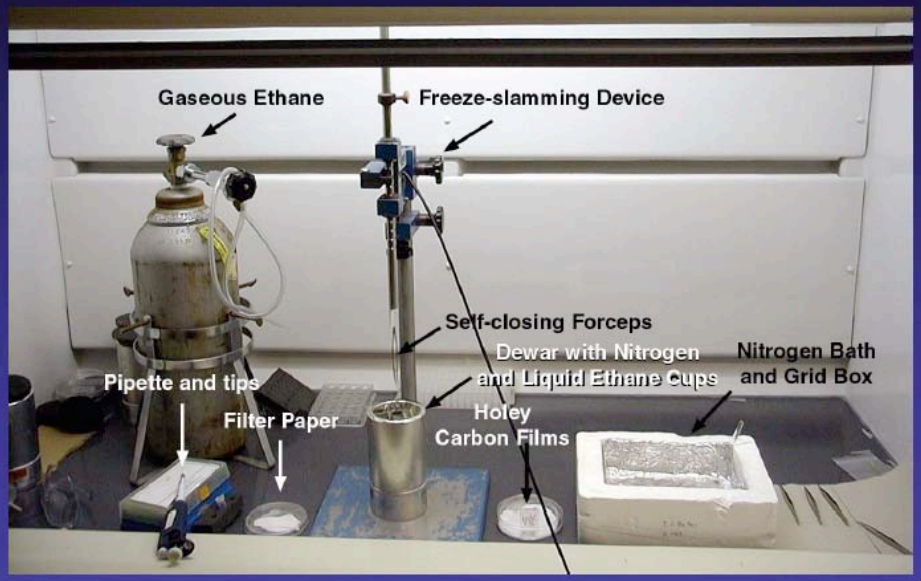

Blotting and Plunge Freezing

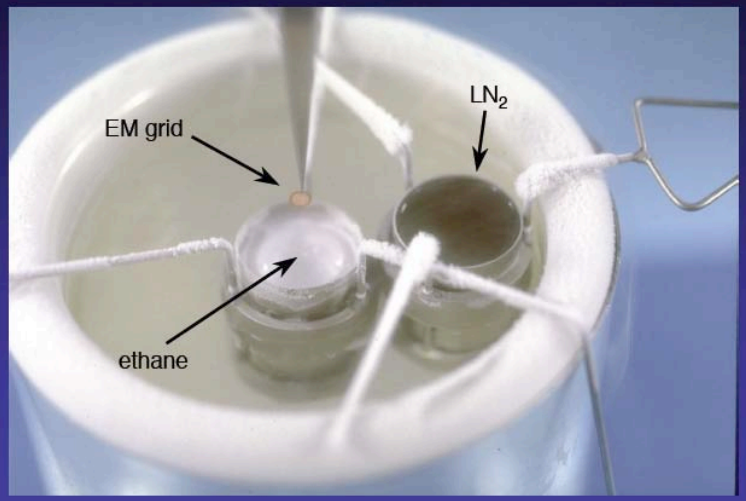

Electron Cryo-Microscopy

Contrast

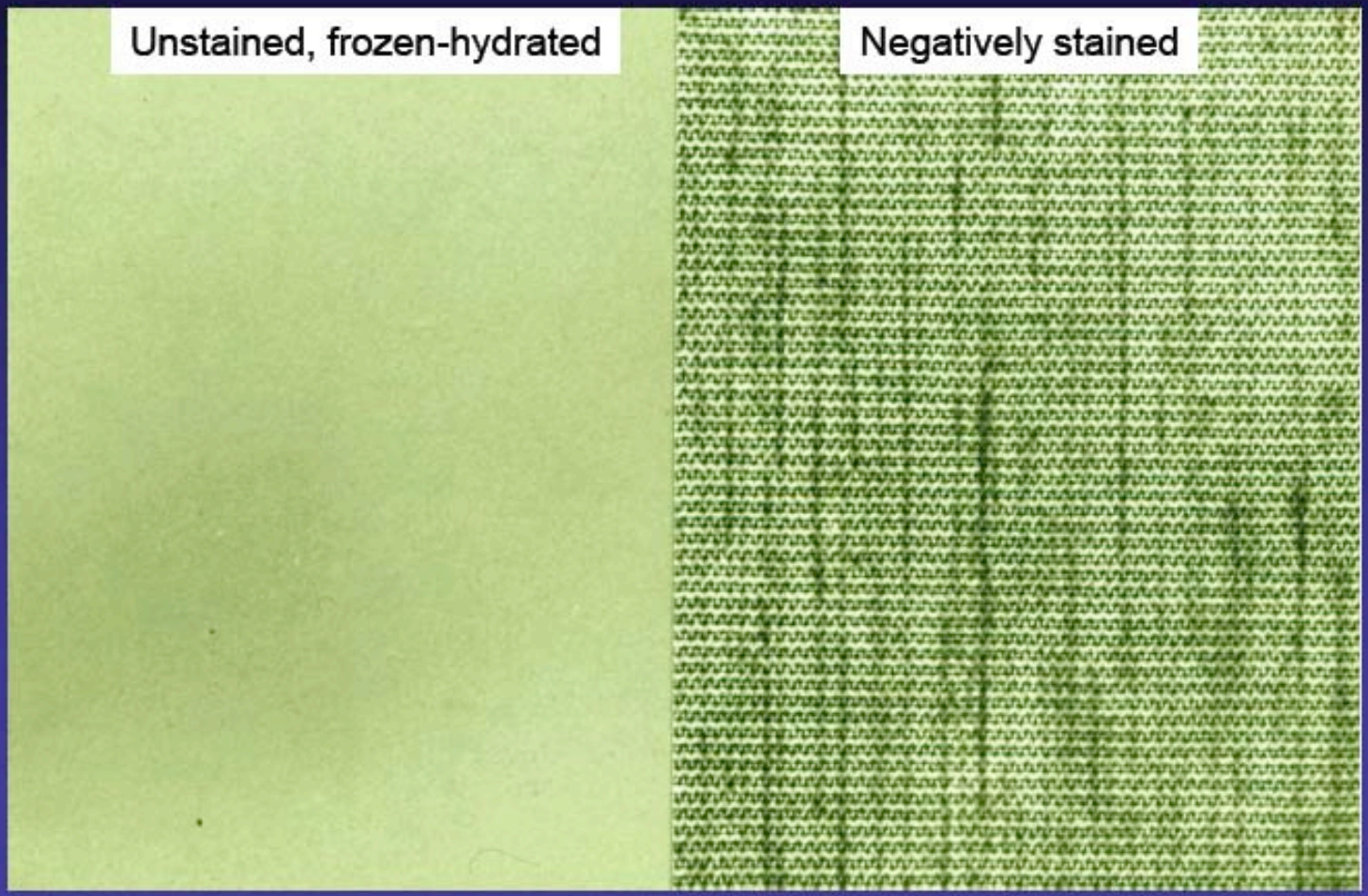

Images provided by R. Milligan

Feb 2007

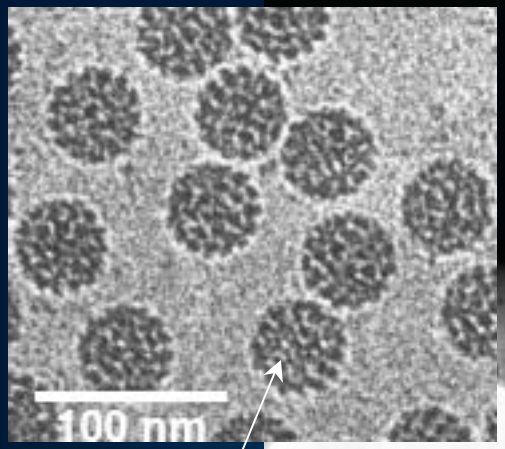

Thick
Ice

Vitreous
Ice

Specimen

Too Thin
(no sample)

Radiation Damage in Single Particles

SV40 Dose Series

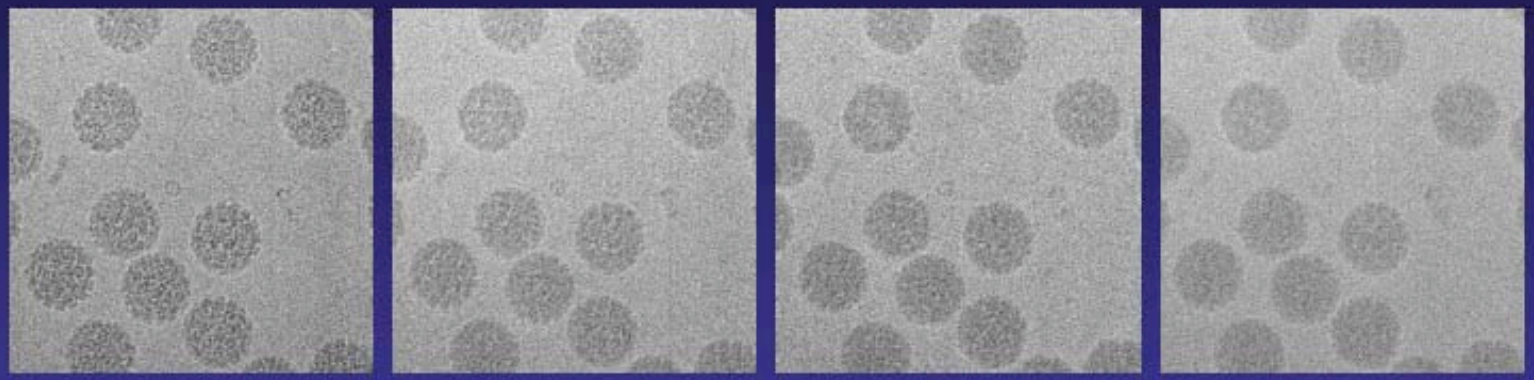

10 $e^-/Å^2$ 20 $e^-/Å^2$ 30 $e^-/Å^2$ 40 $e^-/Å^2$

Radiation Damage in 2D Crystals

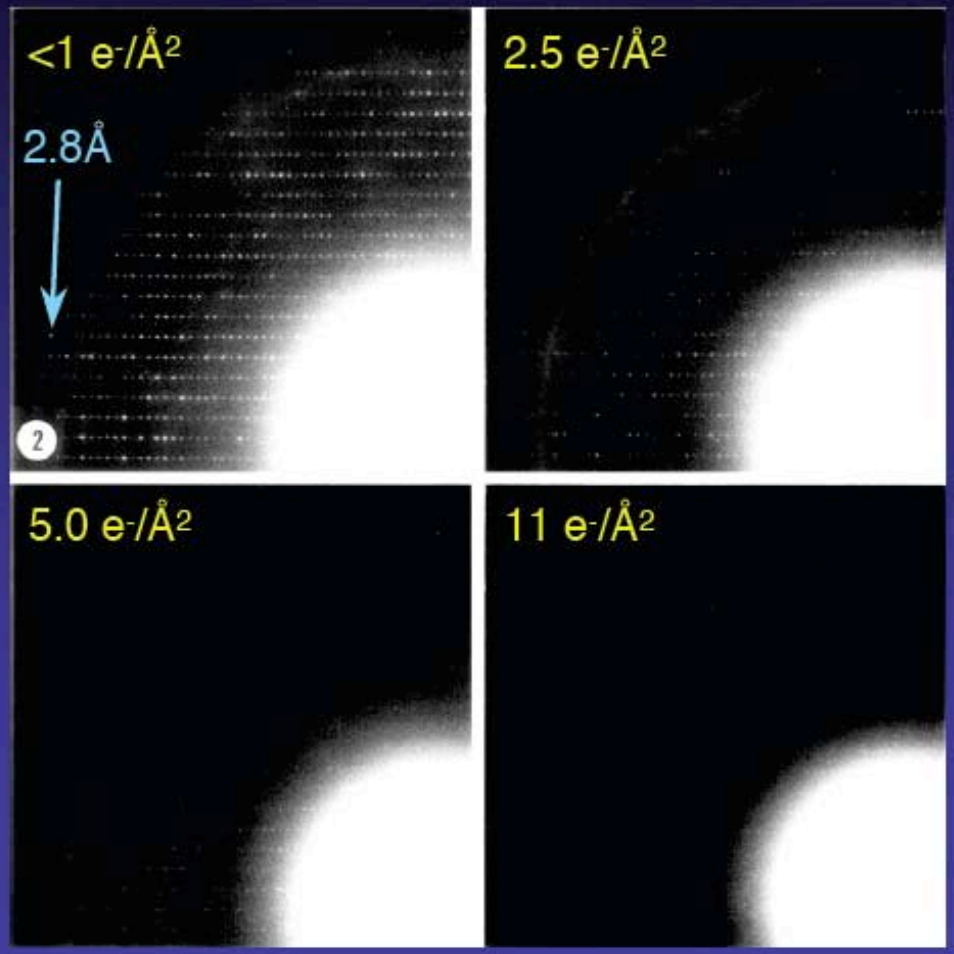

Changes in the electron diffraction pattern of frozen-hydrated catalase crystals resulting from radiation damage

From Taylor and Glaeser (1976)
J. Ultrastruc. Res. **55:448**

3D Image Reconstruction

2D Projections --> 3D Maps

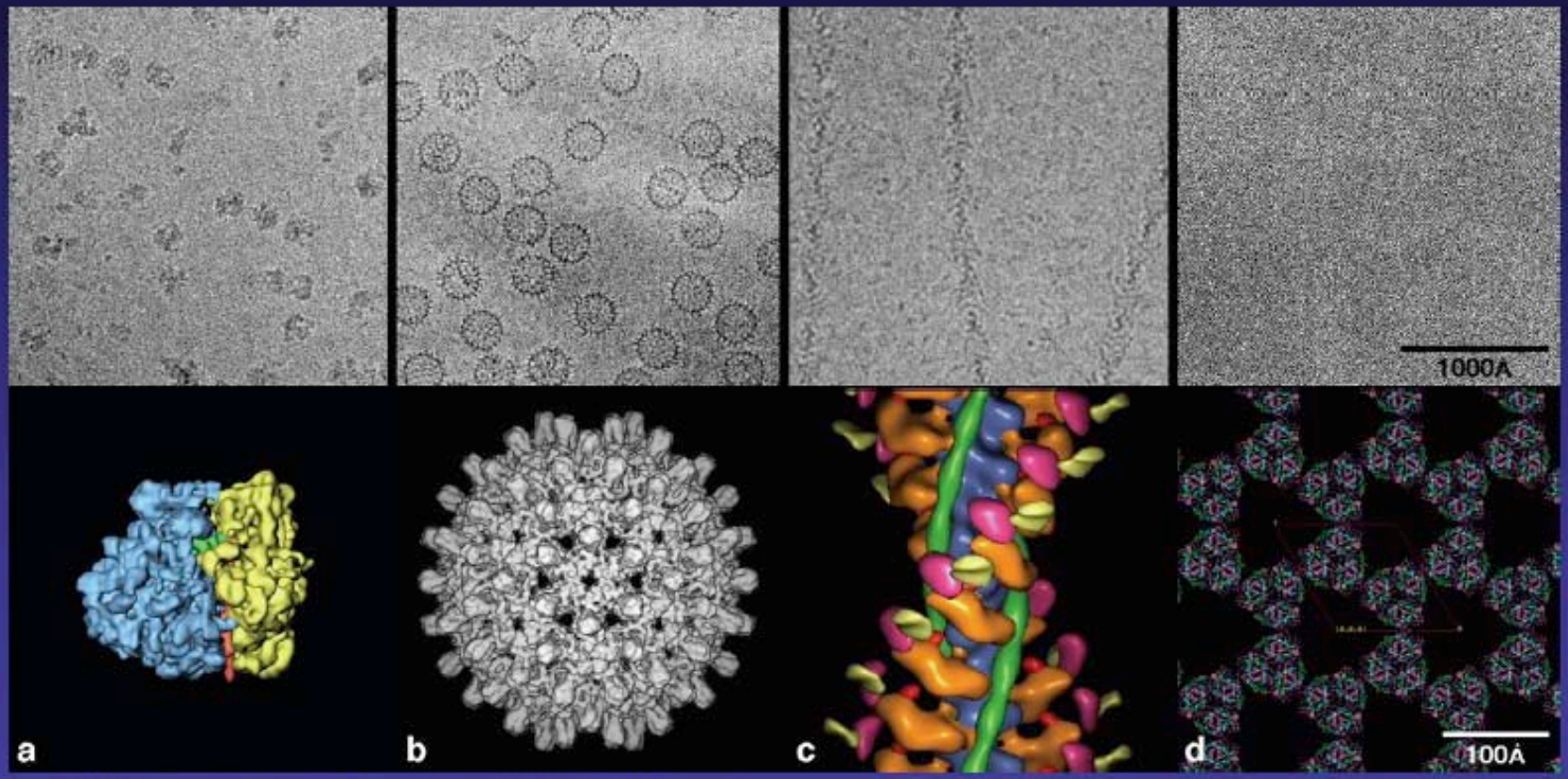

70S *E. coli* ribosome | Hepatitis B virus core | Actin-myosin filament | Light-harvesting 2D crystal

Electromigration Voids in"Real Devices"

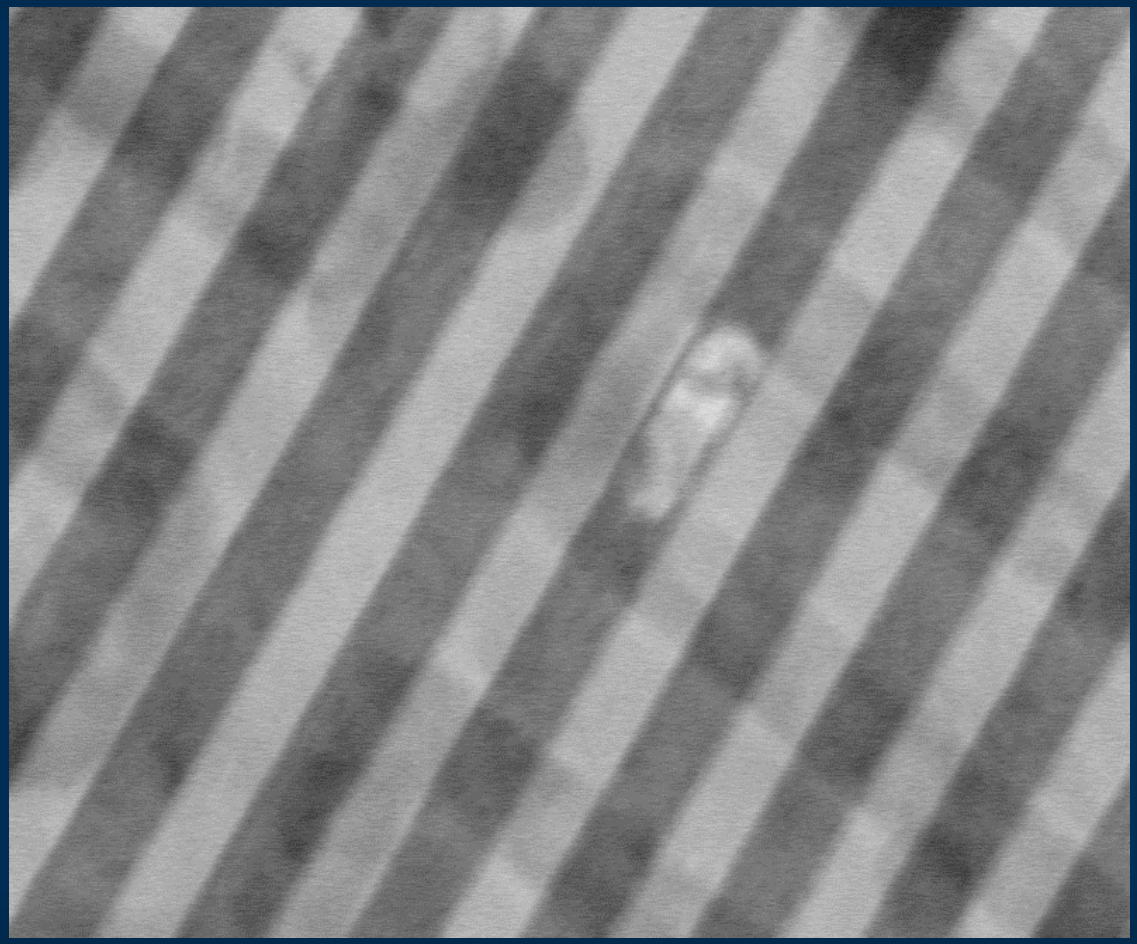

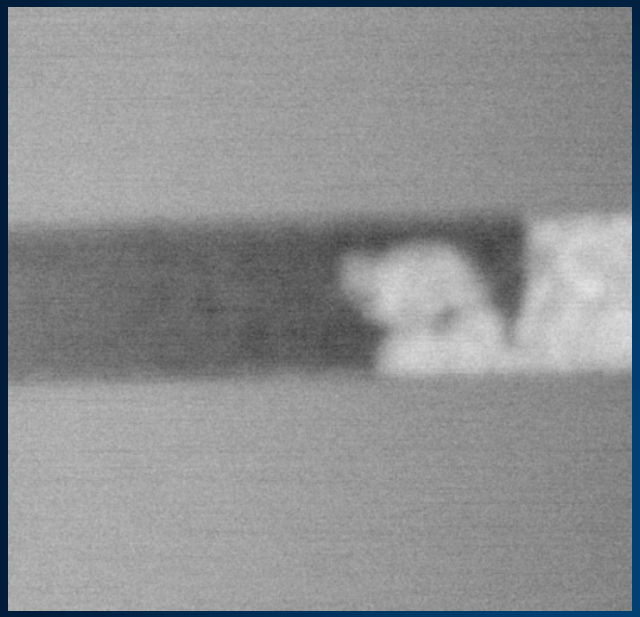

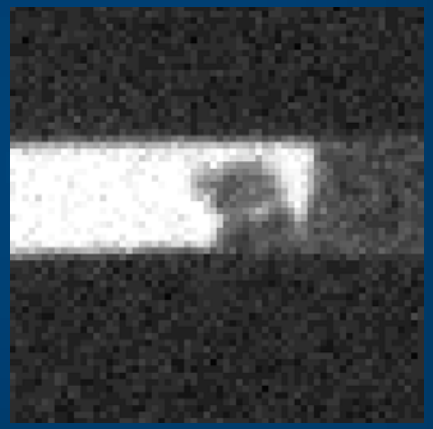

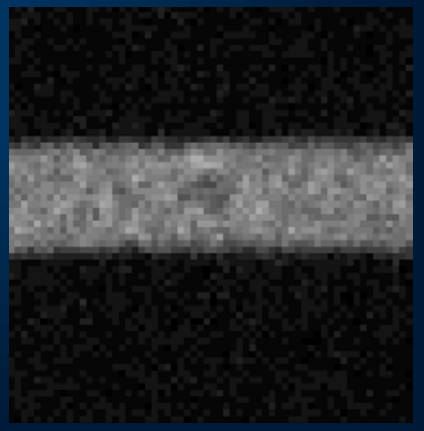

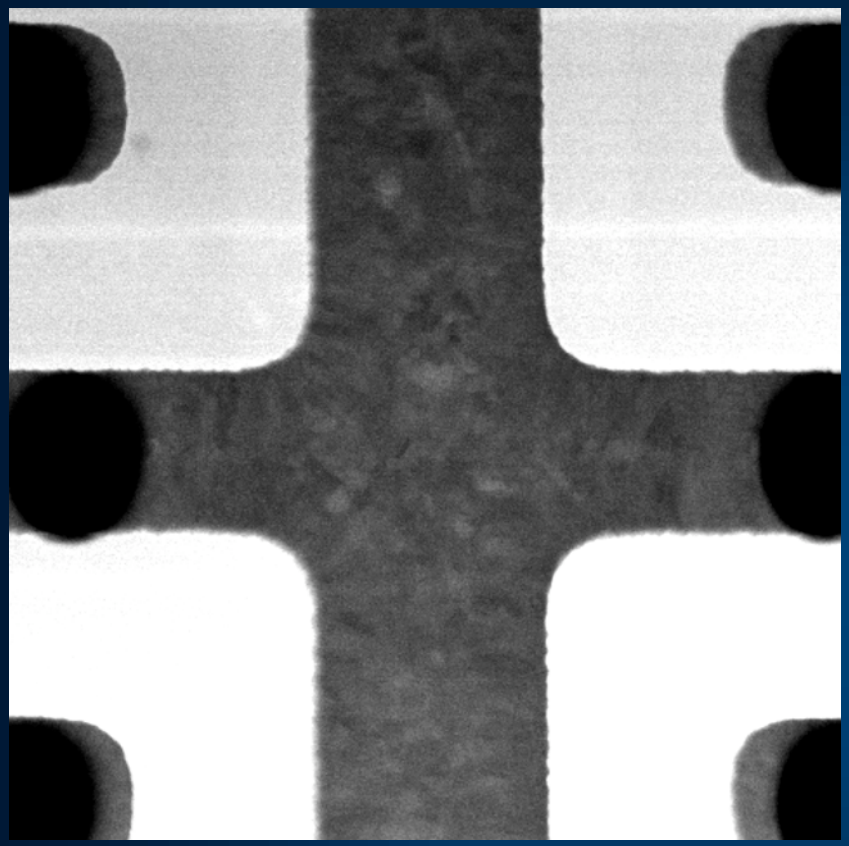

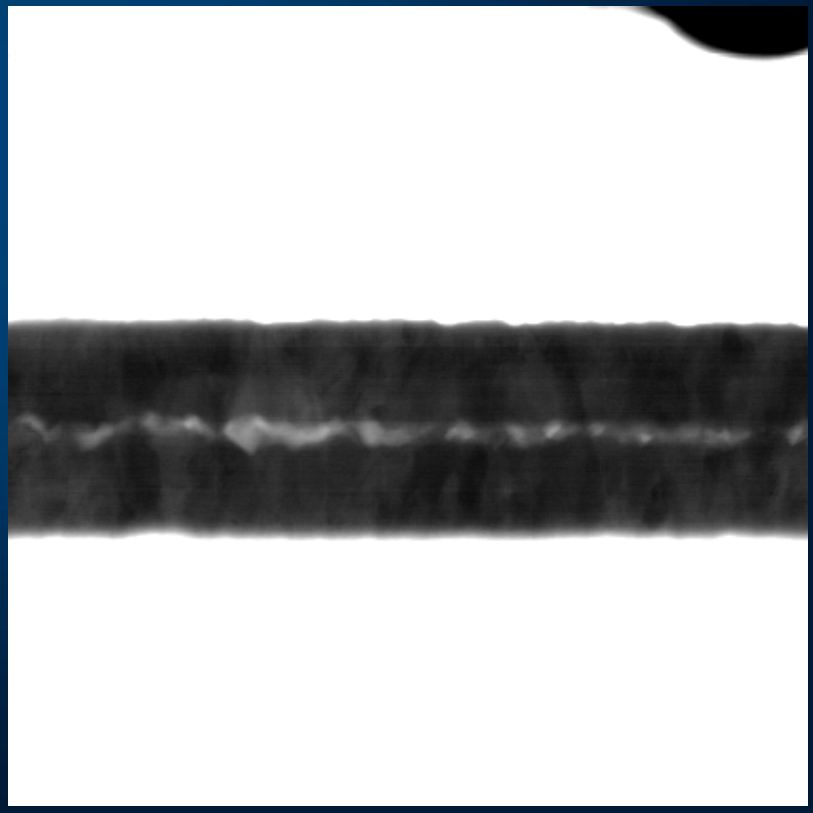

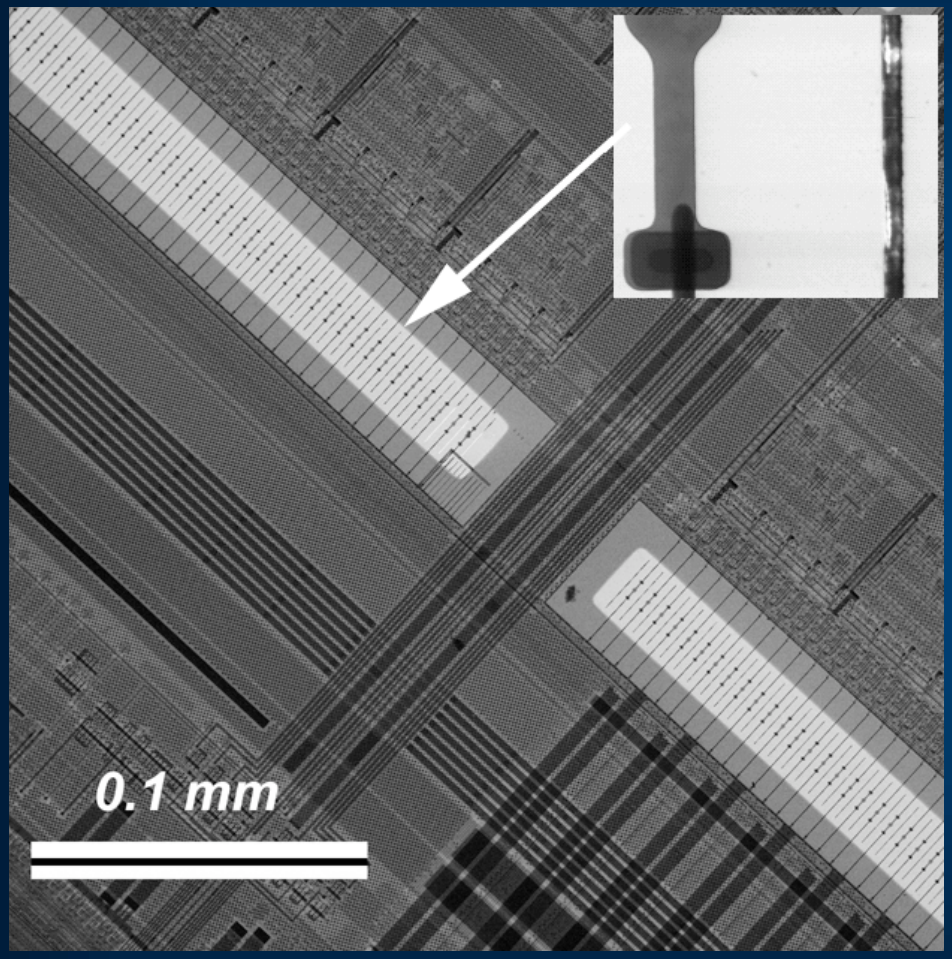
0.1 mm

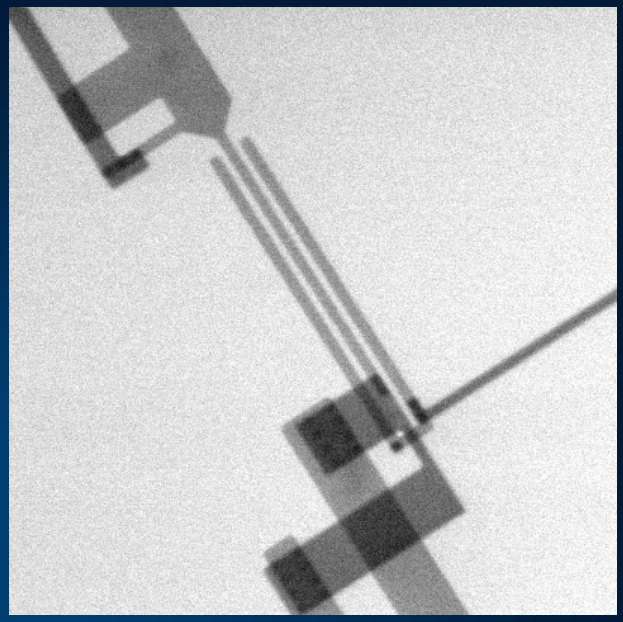

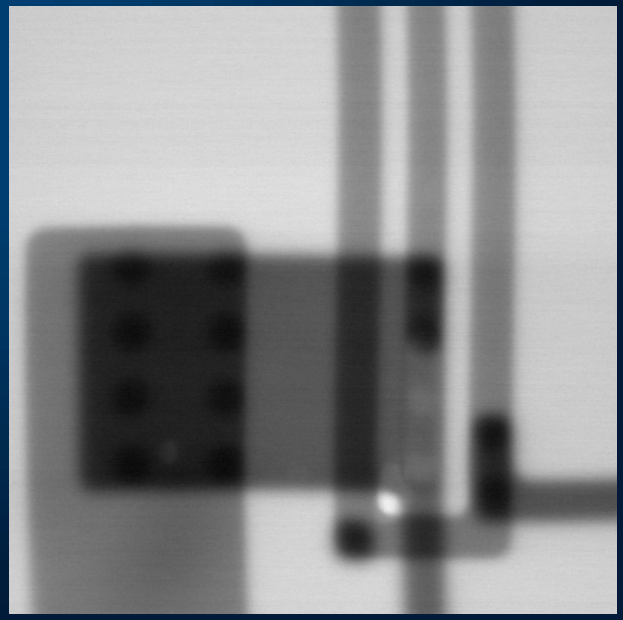

Elastic Scattering

Crystalline Solids:

$$I(\theta) \sim |F(hkl)|^2$$

$$F(hkl) = \sum_j f_j(\theta)\ e^{(-2\pi i \vec{k}\cdot\vec{r})}$$

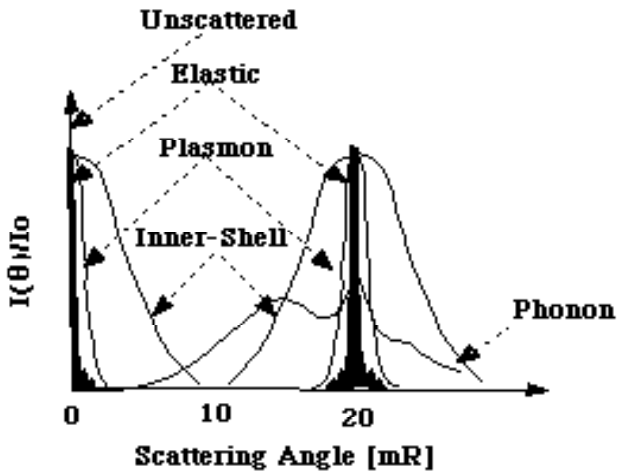

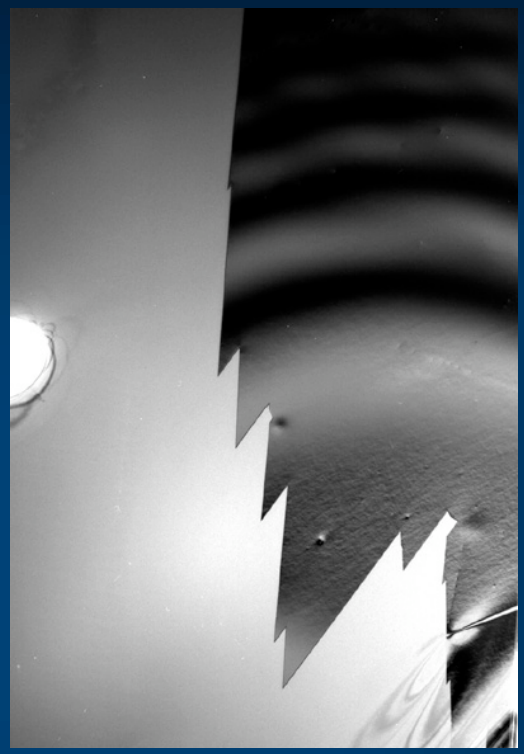

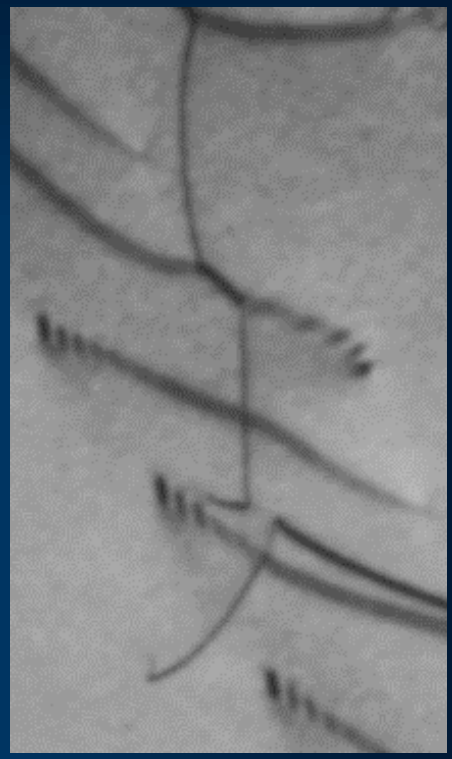

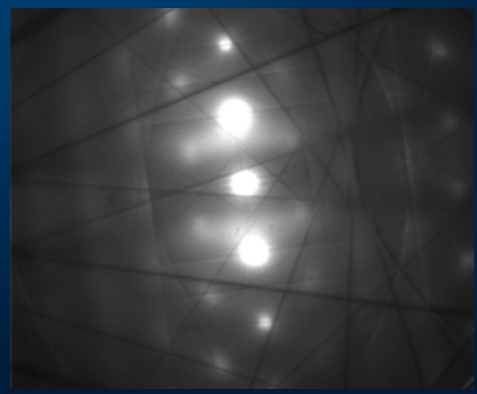

TEM/HREM Image Interpretation/Calculation (well beyond a 90 minute lecture)

$$\nabla^2\psi(\mathbf{r}) + (8\pi^2 me/h^2)[E + V(\mathbf{r})]\psi(\mathbf{r}) = 0$$

$$\psi(\mathbf{r}) = \exp(2\pi i \boldsymbol{\chi}.\mathbf{r})$$

$$V(\mathbf{r}) = \frac{h^2}{2me}\sum_g U_g \exp(2\pi i \mathbf{g}.\mathbf{r}) = \sum_g V_g \exp(2\pi i \mathbf{g}.\mathbf{r})$$

$$\psi(\mathbf{r}) = \phi_o(z)\exp(2\pi i \mathbf{K}.\mathbf{r}) + \phi_g(z)\exp(2\pi i(\mathbf{K}+\mathbf{g}).\mathbf{r})$$

$$K^2 = \frac{2meE}{h^2} + U_0 = \chi^2 + U_0$$

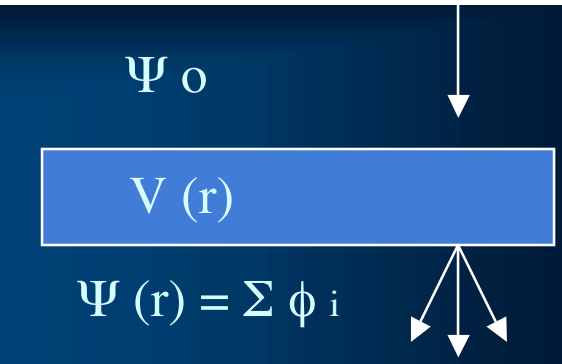

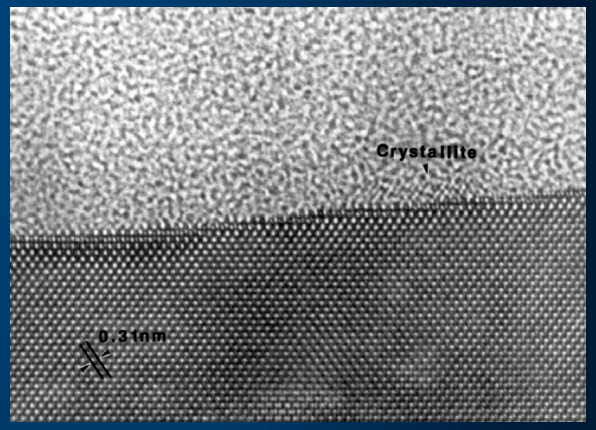

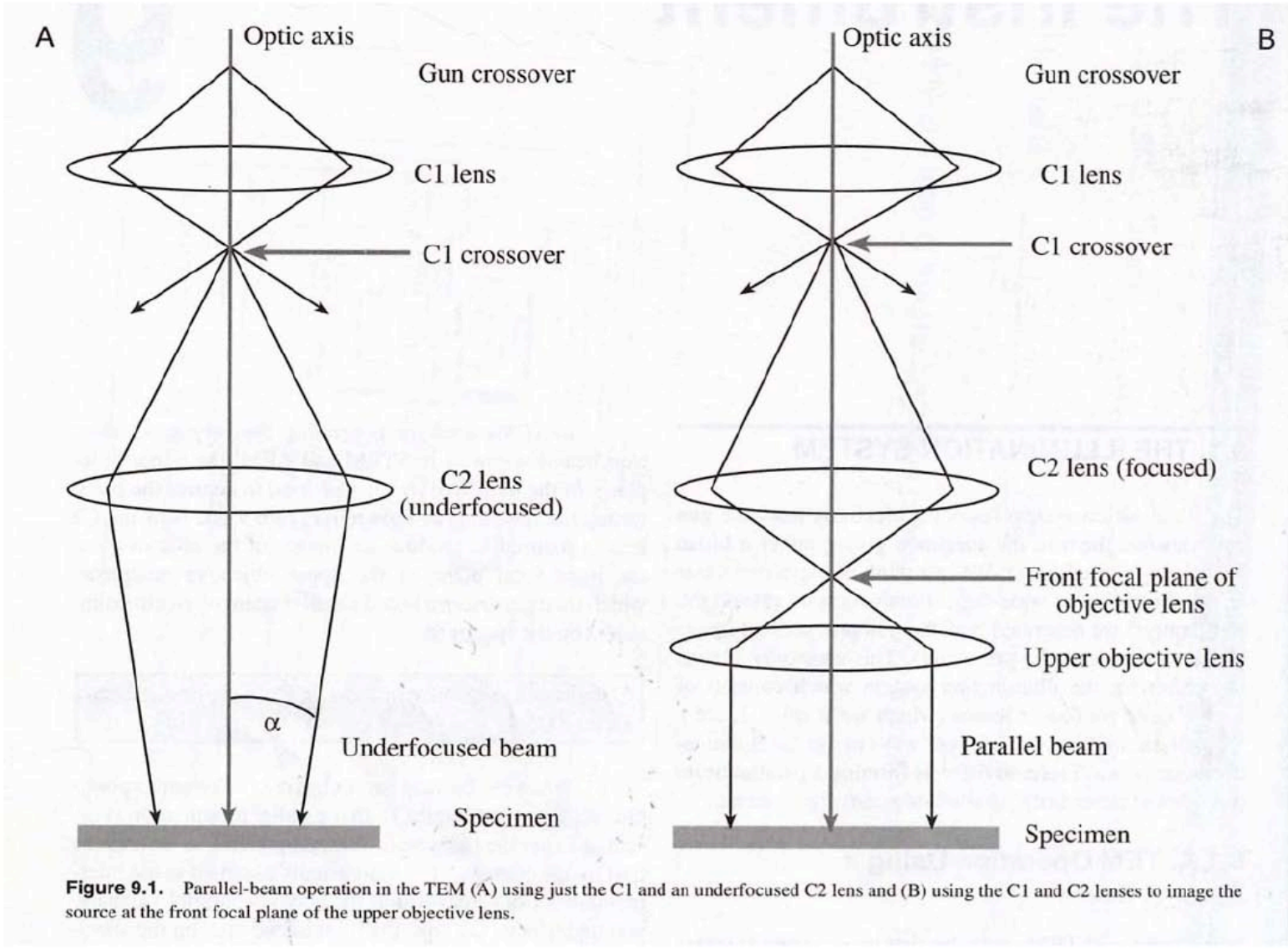

Figure 9.1. Parallel-beam operation in the TEM (A) using just the C1 and an underfocused C2 lens and (B) using the C1 and C2 lenses to image the source at the front focal plane of the upper objective lens.

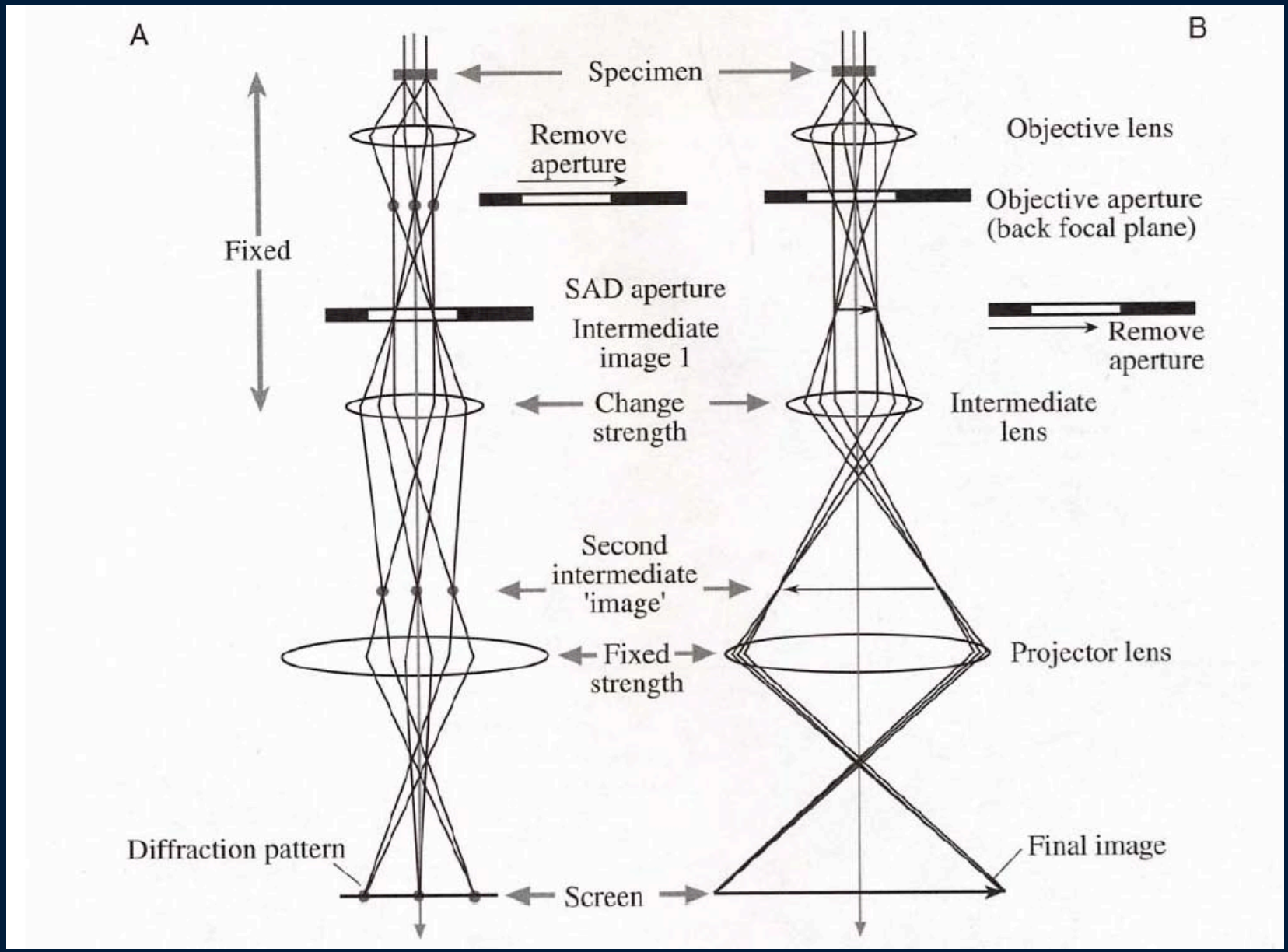
A
B
Specimen
Remove aperture
Objective lens
Objective aperture (back focal plane)
Fixed
SAD aperture
Intermediate image 1
Remove aperture
Change strength
Intermediate lens
Second intermediate 'image'
Fixed strength
Projector lens
Diffraction pattern
Screen
Final image

Bright-Field and Dark-Field Imaging

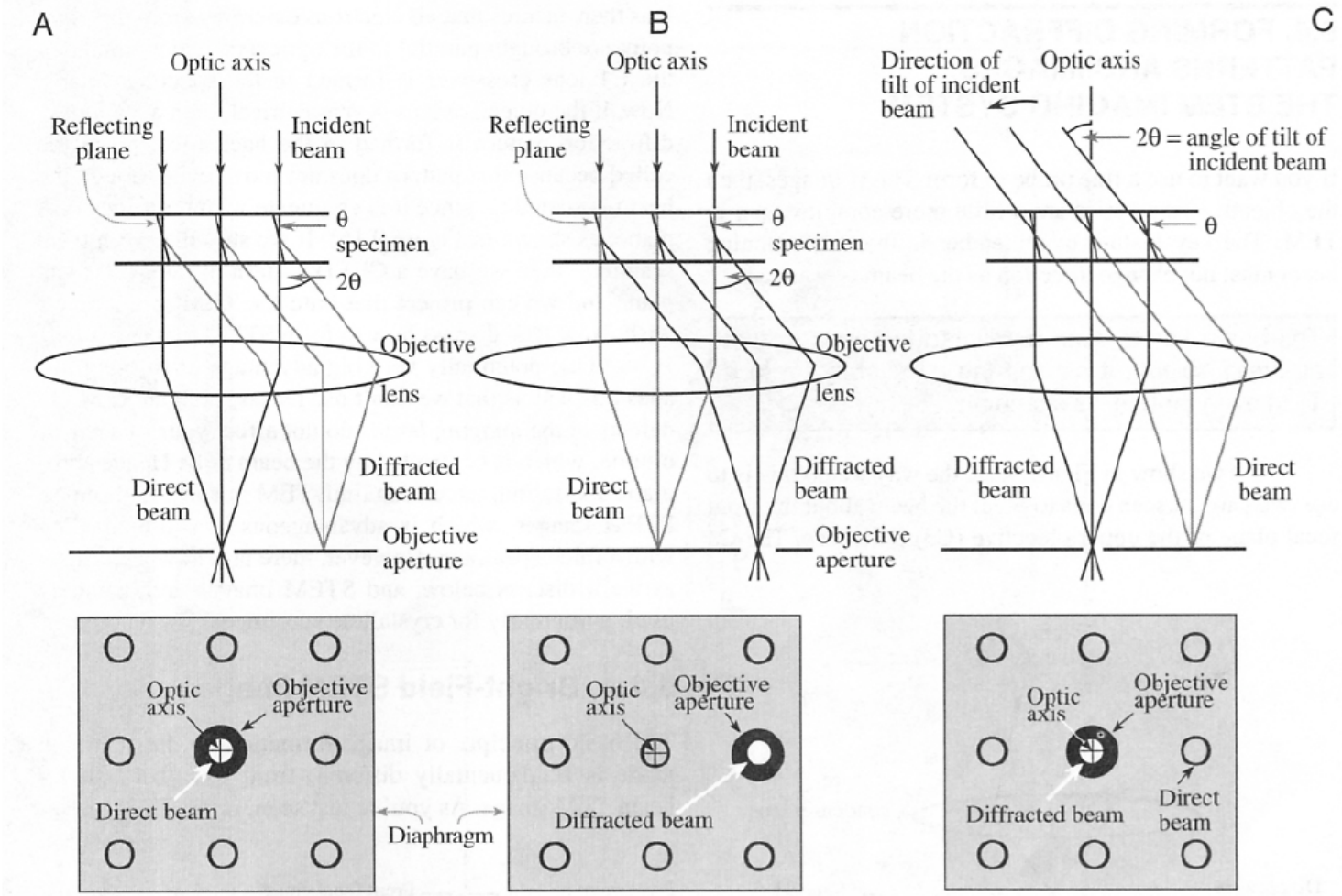

Figure 9.14. Ray diagrams showing how the objective lens/aperture are used in combination to produce (A) a BF image formed from the direct beam, (B) a displaced-aperture DF image formed with a specific off-axis scattered beam, and (C) a CDF image where the incident beam is tilted so that the scattered beam remains on axis. The area selected by the objective aperture, as seen on the viewing screen, is shown below each ray diagram.

Deflection Coils

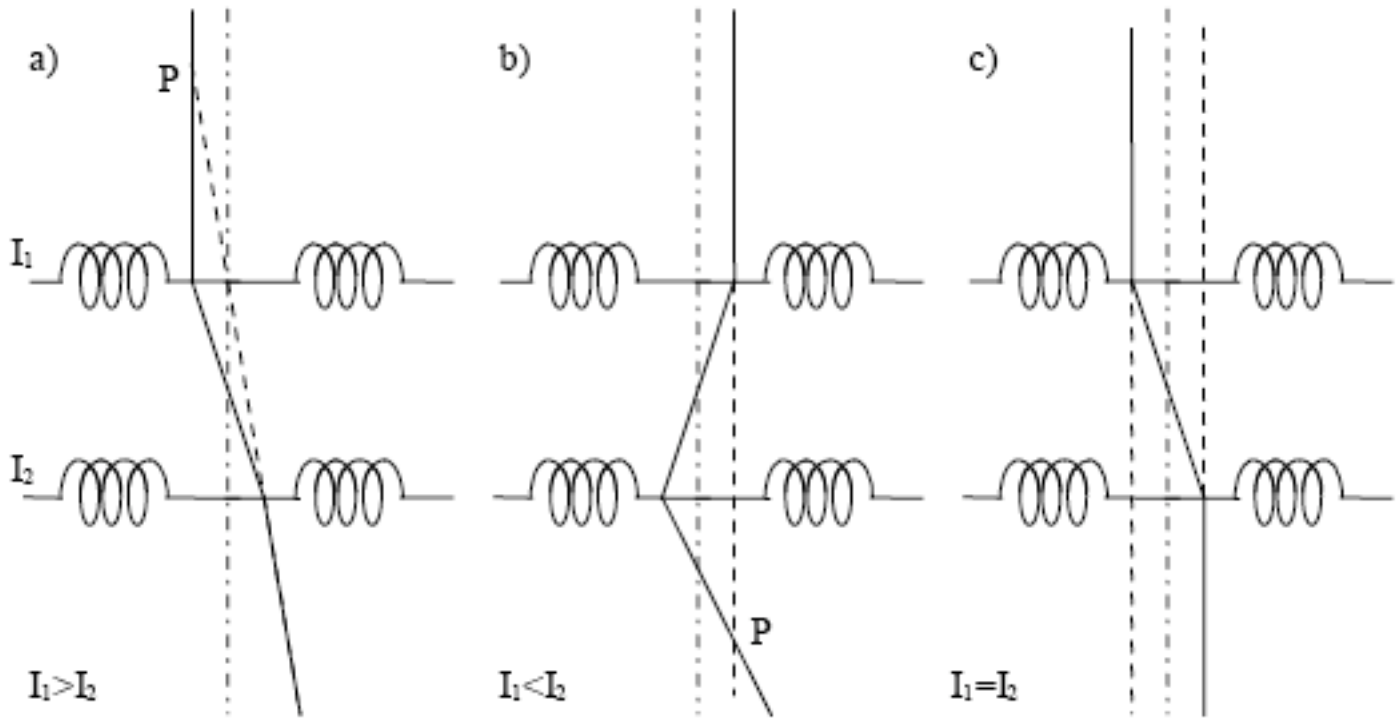

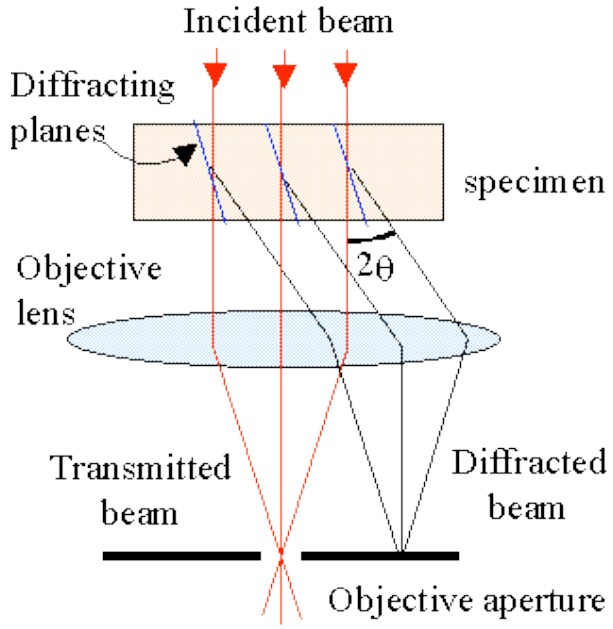

Bright Field Imaging

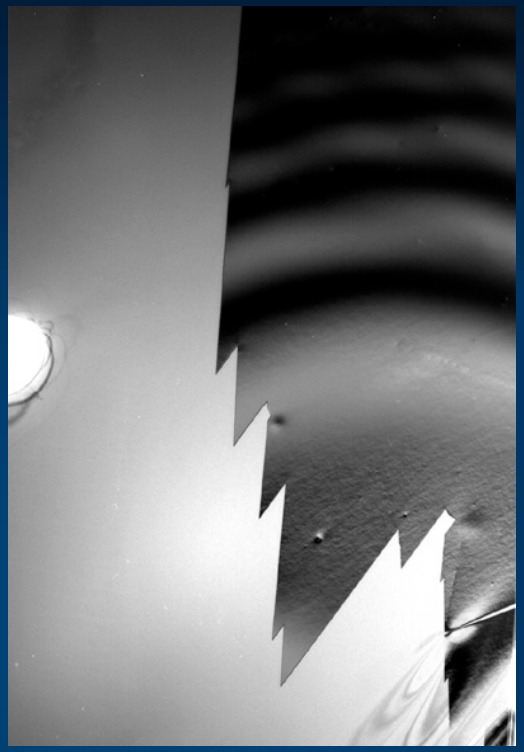

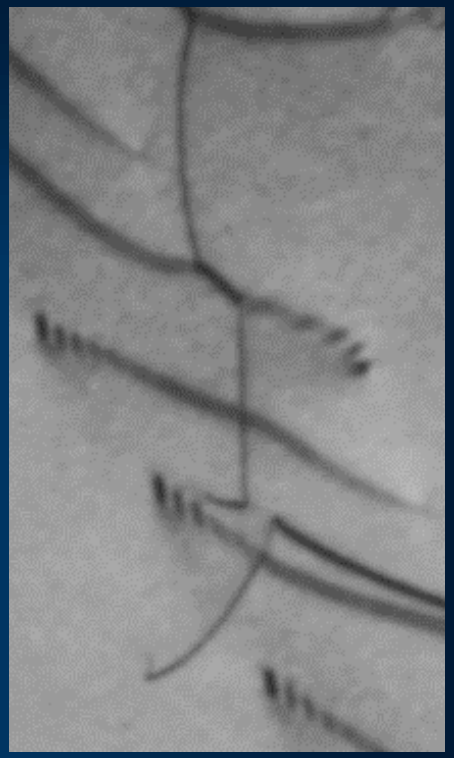

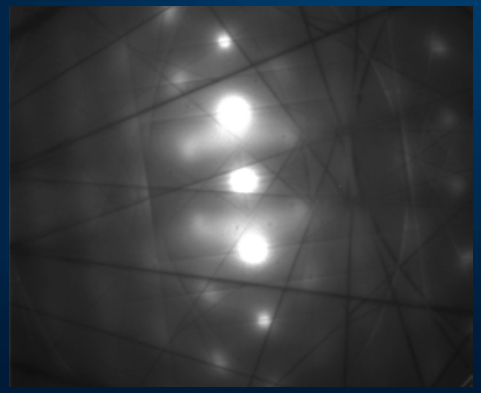

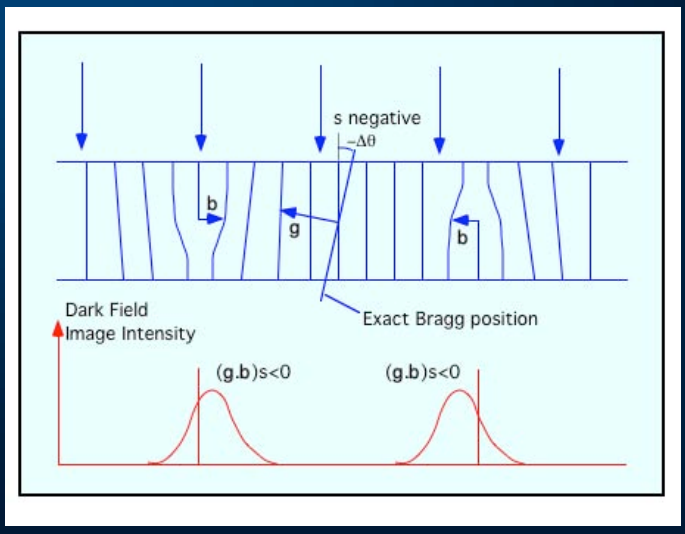

Bright Field/Dark Field Imaging

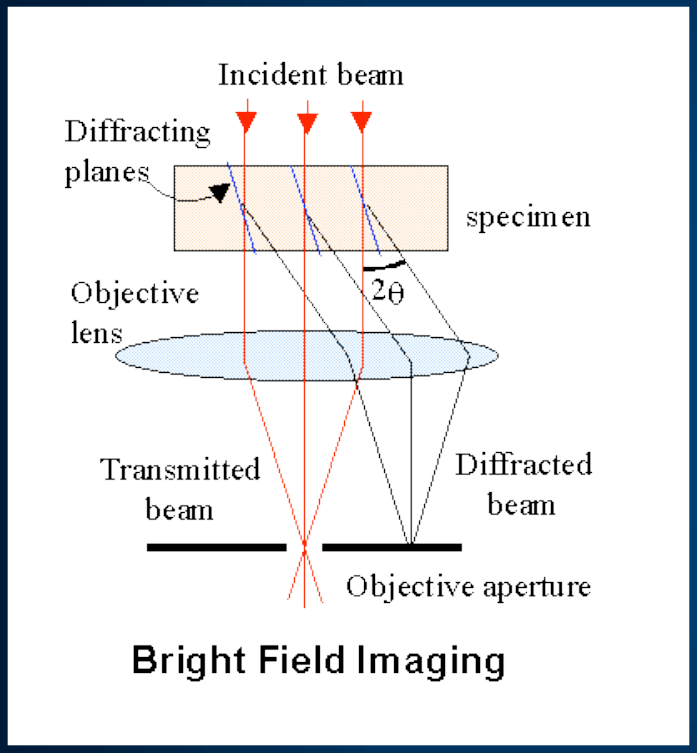

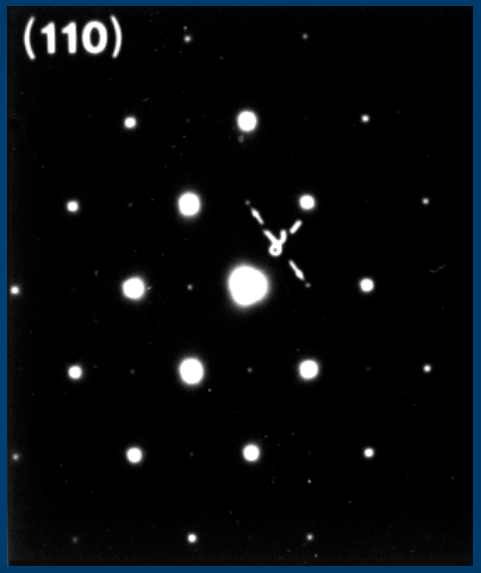

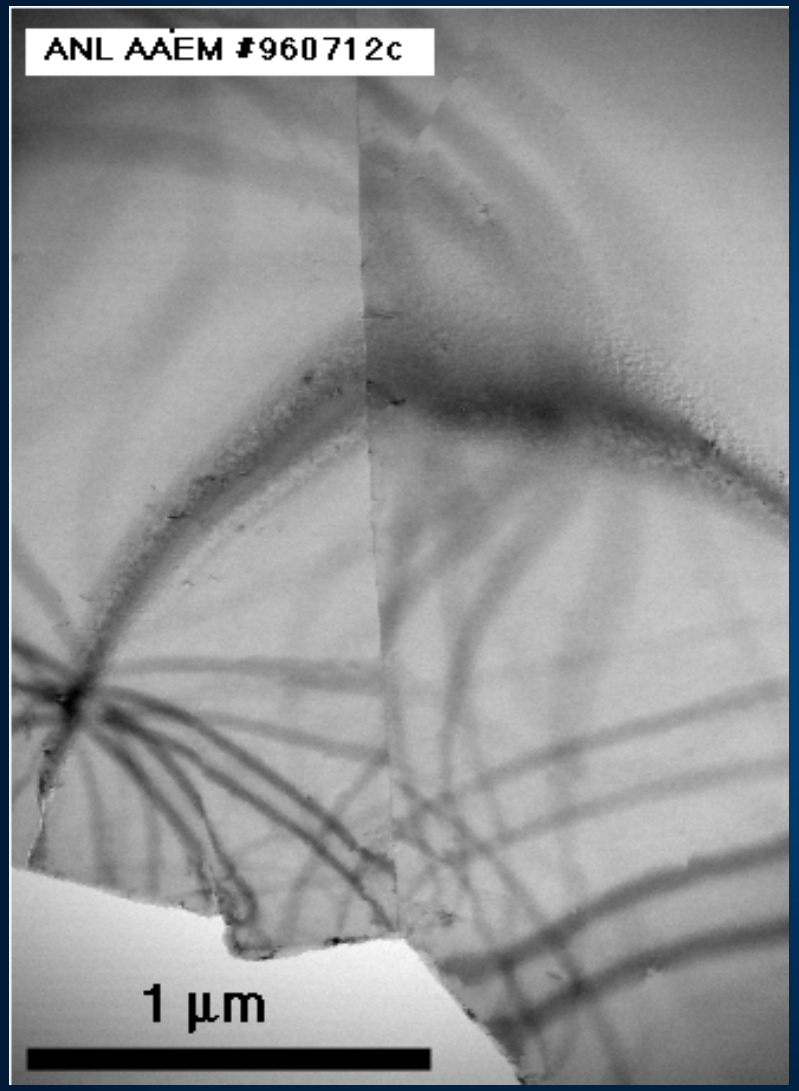
ANL AAEM #960712c
1 µm

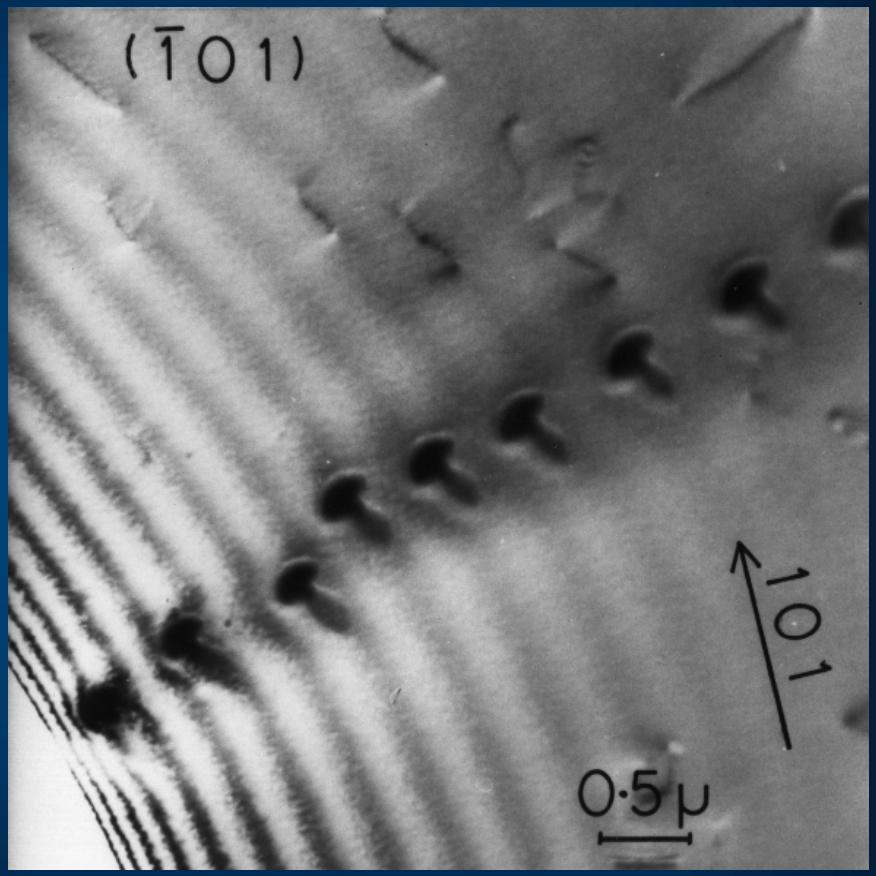
(1̄01)
101
0·5 µ

Kinematical Theory of Image Contrast

1.) Amplitude Contrast
2.) Diffraction into a Beam is small
3.) Multiple Diffraction Events do not occur
4.) Each point of the specimen can be considered independent of its neigbors (column approximation)
5.) Each slab in the column can be assumed to act as a Fresnel Zone

$\phi_0 \sim 1 - \phi_g$

$$\phi_g = (\pi i/\xi_g) \int_0^t \exp[-2\pi i s_g z]\, dz$$

$$\xi_g = \pi V_c \cos\theta / \lambda F(\theta)$$

$$\phi_g = (\pi i/\xi_g)\,(\sin \pi t s_g/\pi s_g)\,\{\exp(-i\pi t s_g)\}$$

$$\phi_g{}^2 = I_g = (\pi^2/\xi_g{}^2)\,(\sin{}^2 \pi t s_g/\pi^2 s_g{}^2)$$

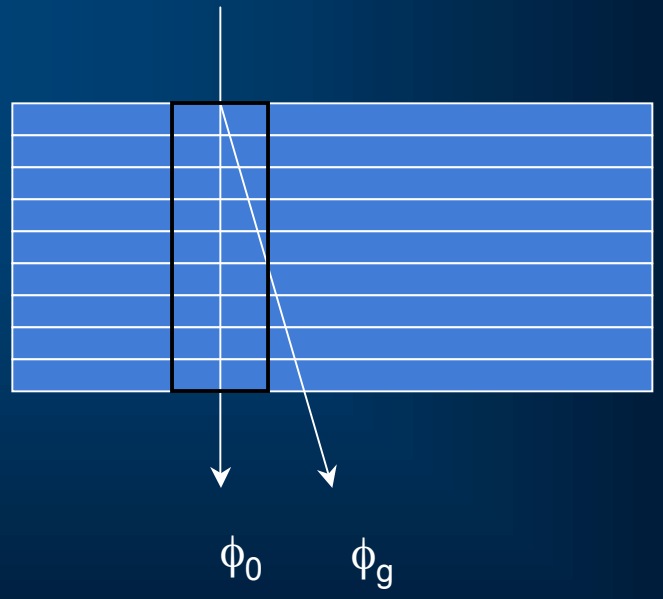

Contrast Variation with Thickness

$$\phi_g^2 = I = \left(\frac{\pi}{\xi_g}\right)^2 \frac{\sin^2(\pi t s)}{(\pi s)^2}$$

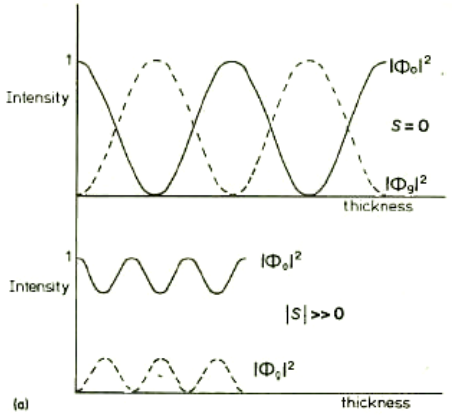

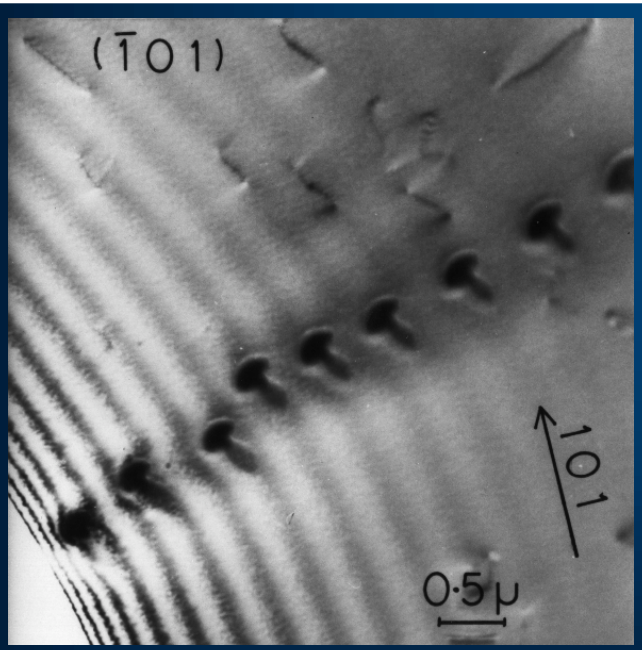

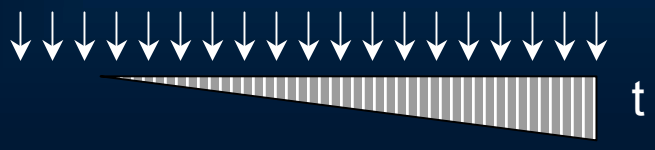

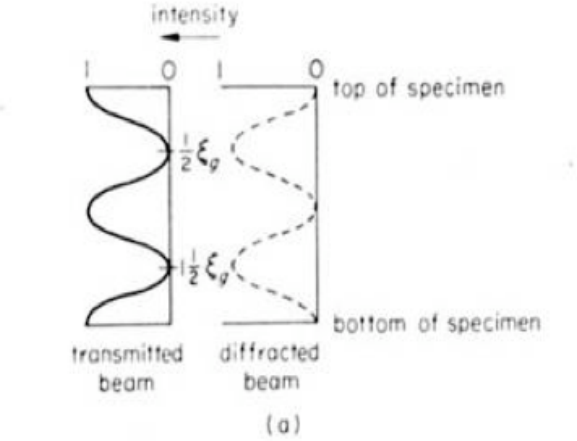

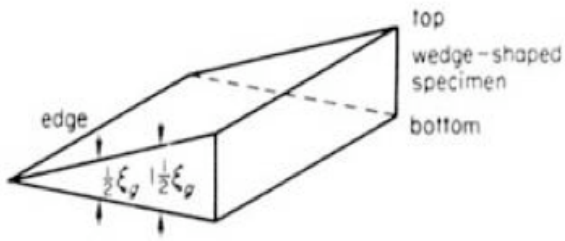

Contrast Variation with Orientation

$$\phi_g^2 = I = \left(\frac{\pi}{\xi_g}\right)^2 \frac{\sin^2(\pi t s)}{(\pi s)^2}$$

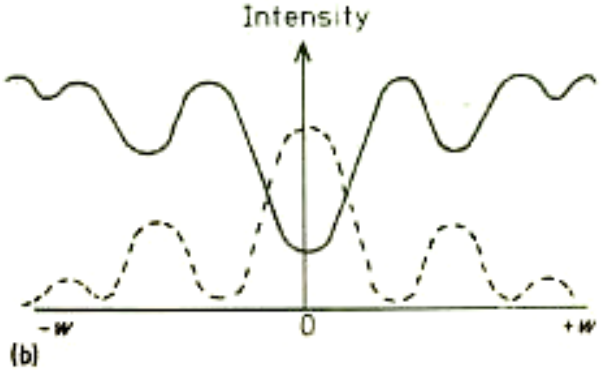

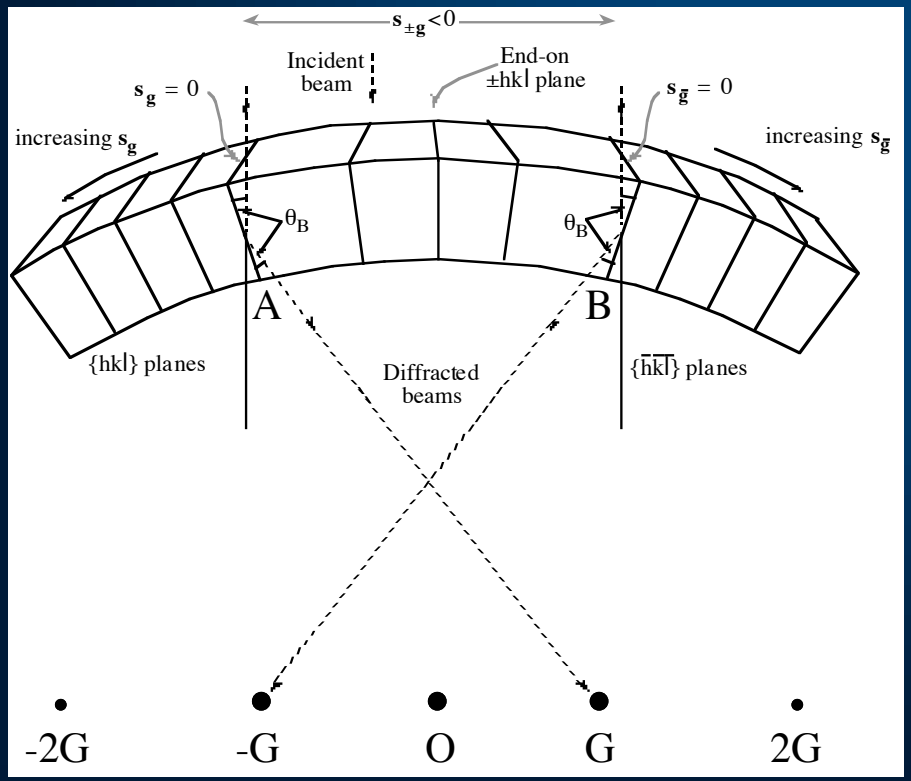

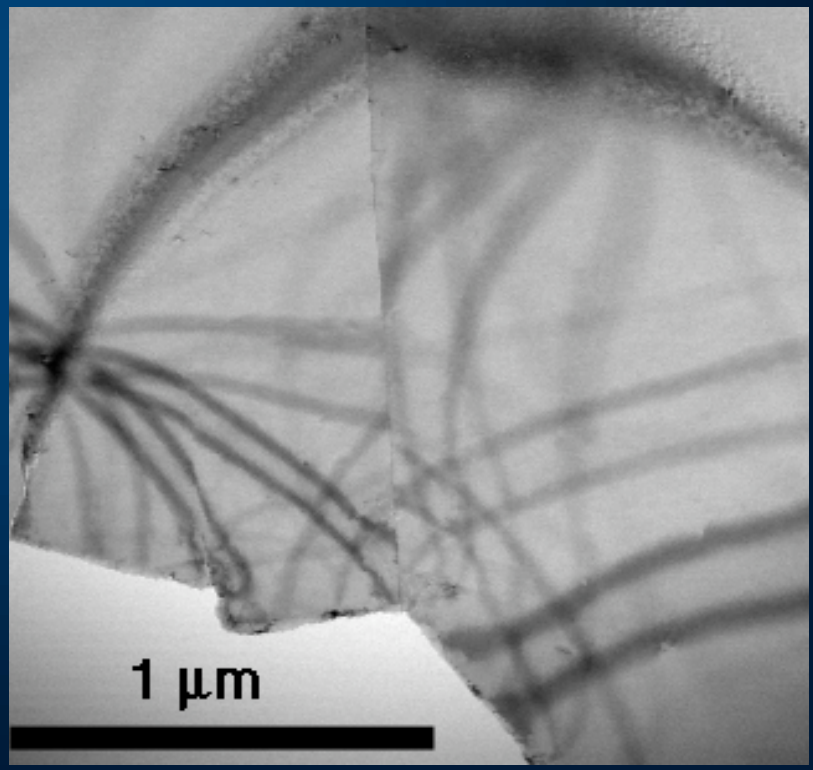

Bend Contours

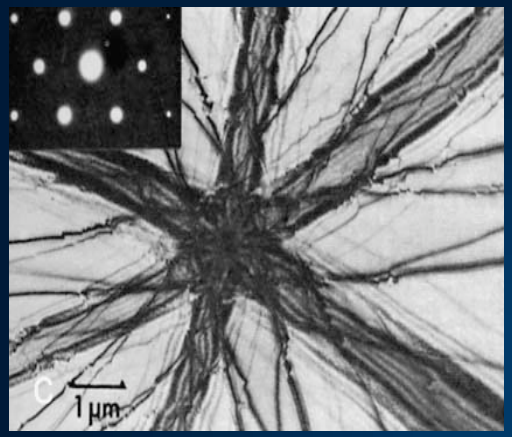

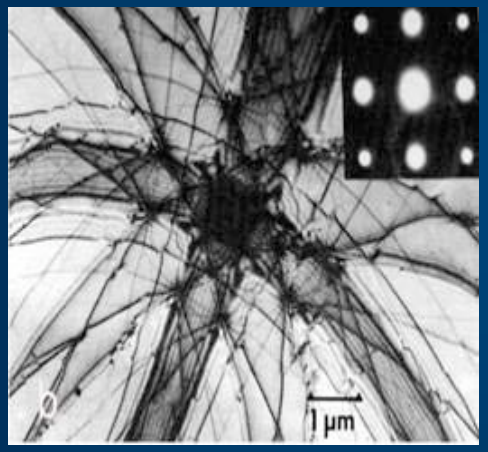

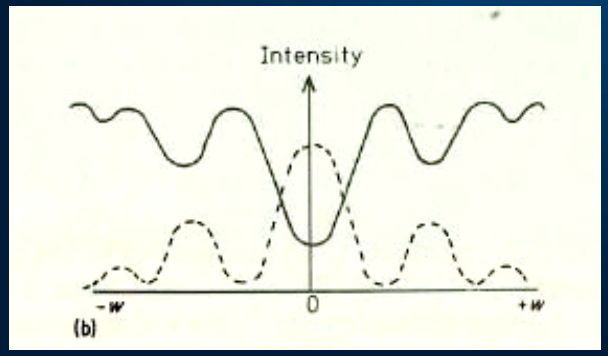

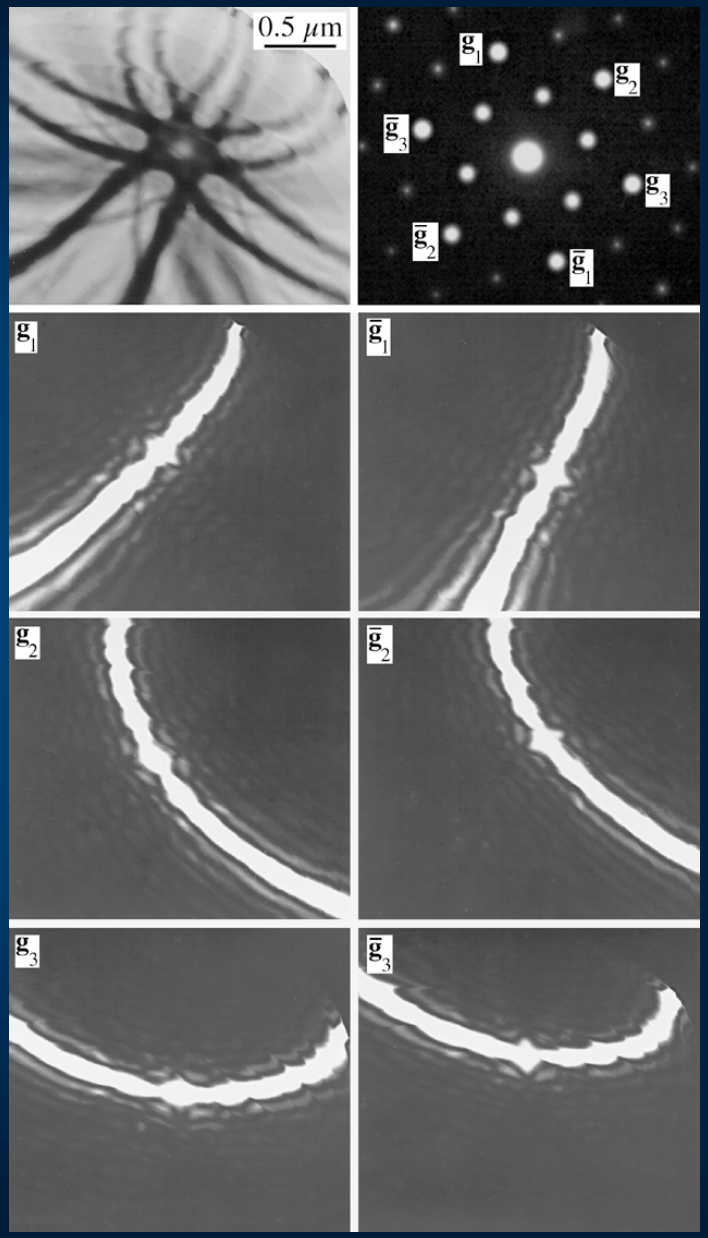

Table C.1 Typical extinction distances for 100 kV electrons (in nm).

Reflection	Al	Cu	Ni	Au	Si	Ge
111	56	24	24	16	60	43
200	67	28	28	18	–	–
220	106	42	41	25	76	45
311	130	51	50	29	135	76
222	138	54	53	31	–	–
400	167	65	65	36	127	66

Reflection	Fe	Nb	Mo
110	27	26	23
200	39	37	32
211	50	46	41
310	71	62	58

Reflection	Mg	Co	Zn	Zr	Cd
0002	81	25	26	32	24
$1\bar{1}01$	100	31	35	38	32
$11\bar{2}0$	141	43	50	49	44
$1\bar{1}00$	151	47	55	59	52
$11\bar{2}2$	171	52	58	59	68
$2\bar{2}01$	202	62	70	69	61
$1\bar{1}02$	231	70	76	84	68

$$\xi_g = \pi V_c \cos\theta / \lambda F(\theta)$$

Dislocation Images

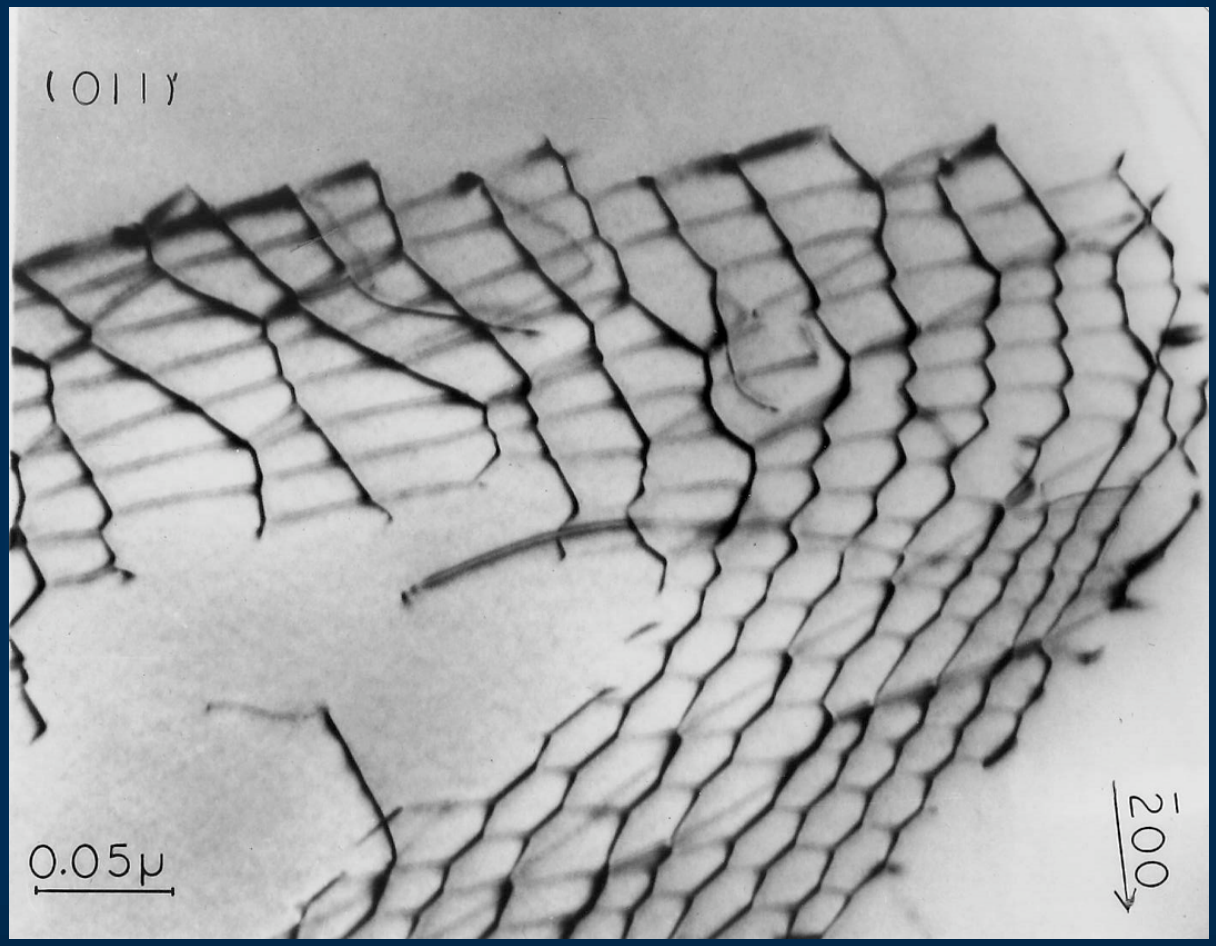

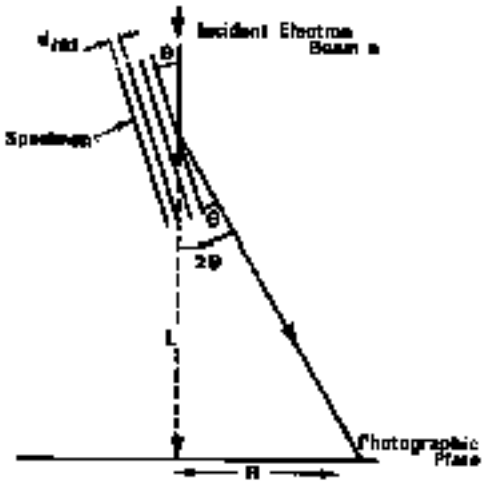

Fig. I.154. The electron microscope considered as a simple electron diffraction camera. (From Beeston, p.224)

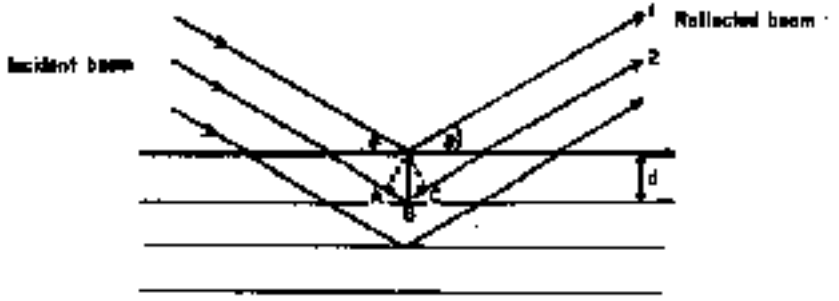

Fig. I.153. Bragg's Law. (From Blundell and Johnson, p.109)

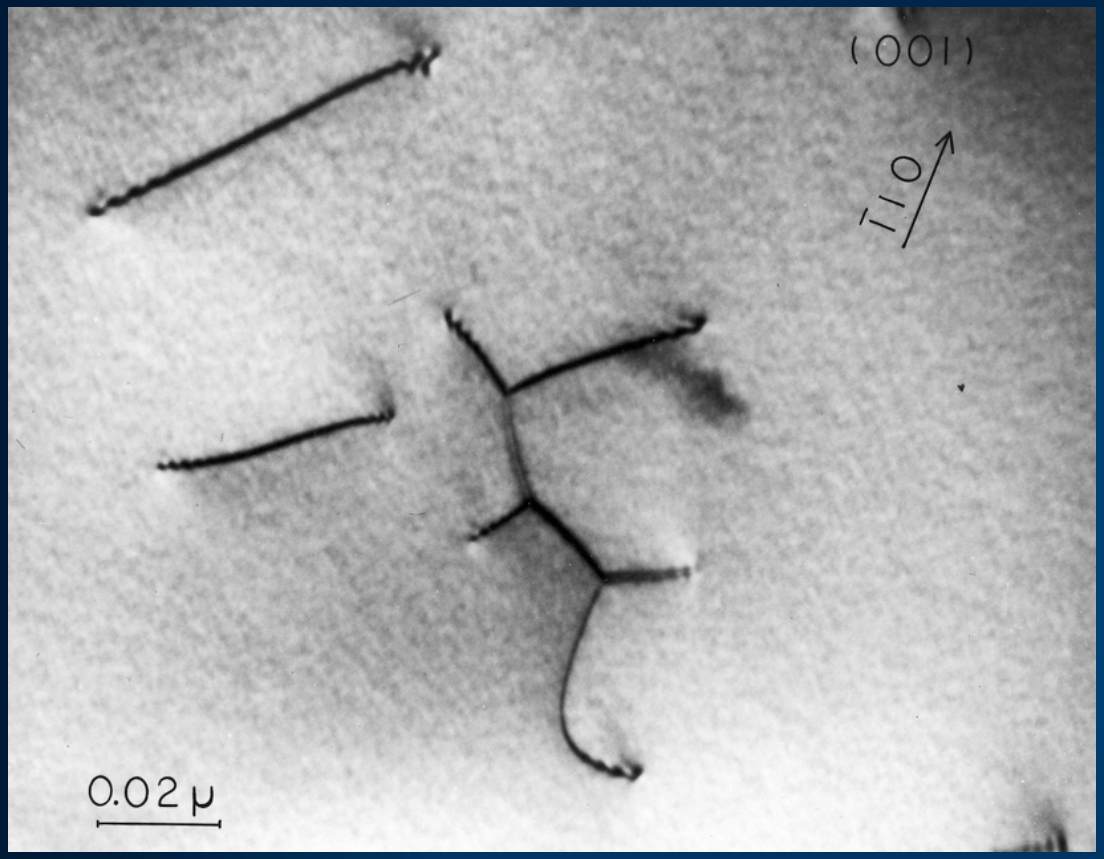

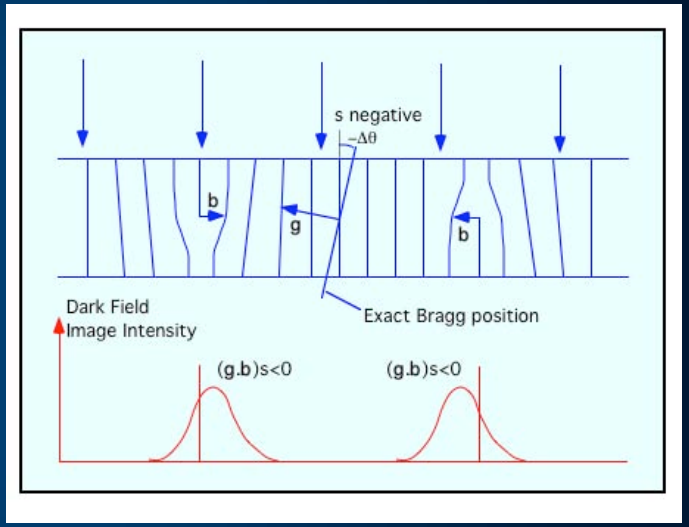

$$\phi_g = \frac{\pi i}{\xi_g} \int_0^t \exp\left[-2\pi i\,(sz + \mathbf{g}.\mathbf{R})\right] dz$$

R = displacement of the unit cell in the area of the defect due to its strain field.

Contrast of Dislocations due to local changes in orientation of planes - recall Bend Contours

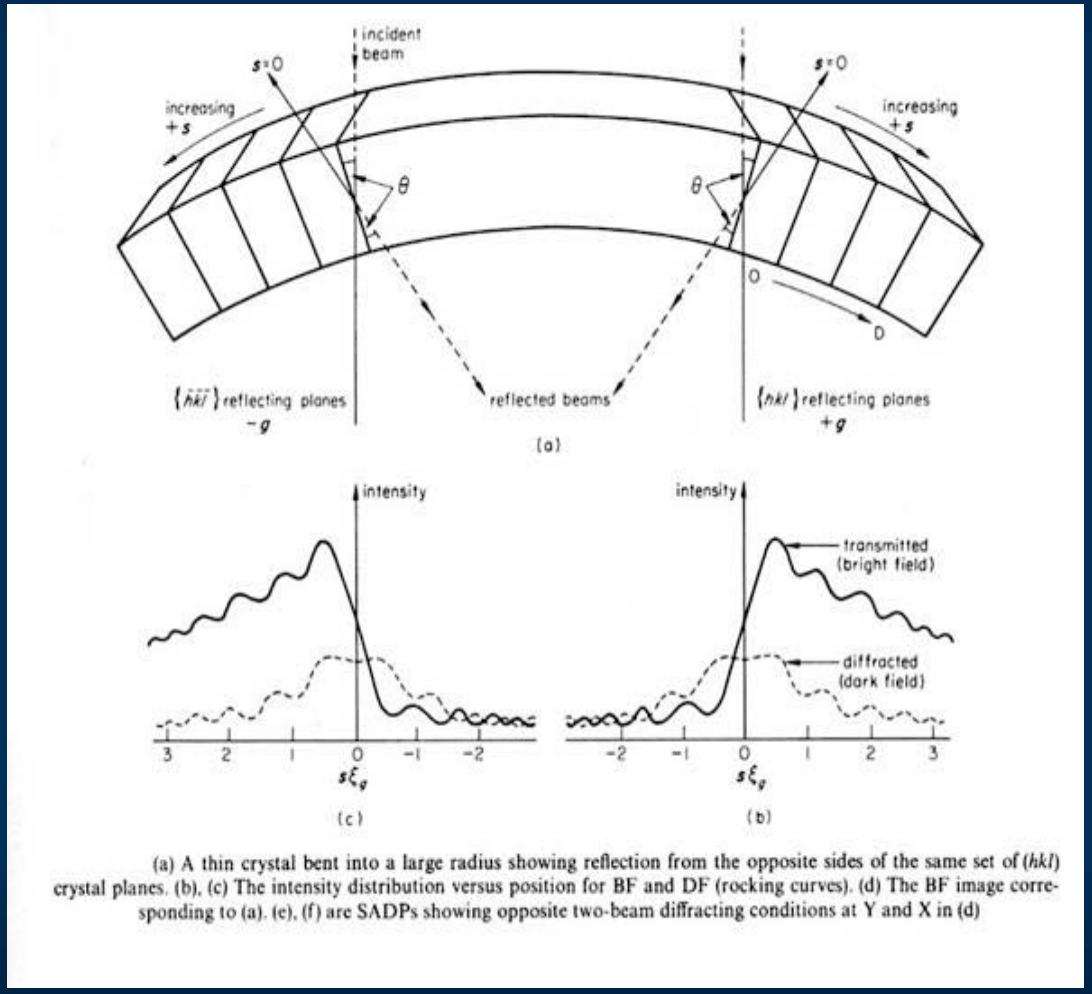

(a) A thin crystal bent into a large radius showing reflection from the opposite sides of the same set of (*hkl*) crystal planes. (b), (c) The intensity distribution versus position for BF and DF (rocking curves). (d) The BF image corresponding to (a). (e), (f) are SADPs showing opposite two-beam diffracting conditions at Y and X in (d)

Dynamical Theory of Image Contrast

$$\frac{d\phi_o}{dz} = \frac{\pi i \phi_o}{\xi_o} + \frac{\pi i \phi_g}{\xi_g} \exp(2\pi i s z)$$

$$\frac{d\phi_g}{dz} = \frac{\pi i \phi_g}{\xi_o} + \frac{\pi i \phi_o}{\xi_g} \exp(-2\pi i s z)$$

$$|\phi_g|^2 = I = \left(\frac{\pi}{\xi_g}\right)^2 \frac{\sin^2(\pi t \bar{s})}{(\pi \bar{s})^2}$$

$$\bar{s} = [s^2 + (1/\xi_g^2)]^{1/2}$$

$$\xi_g^{eff} = \frac{\xi_g}{(1 + s^2 \xi_g^2)^{1/2}}$$

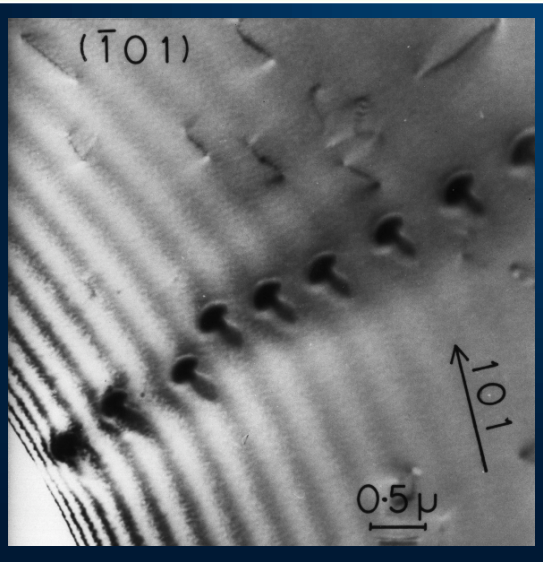

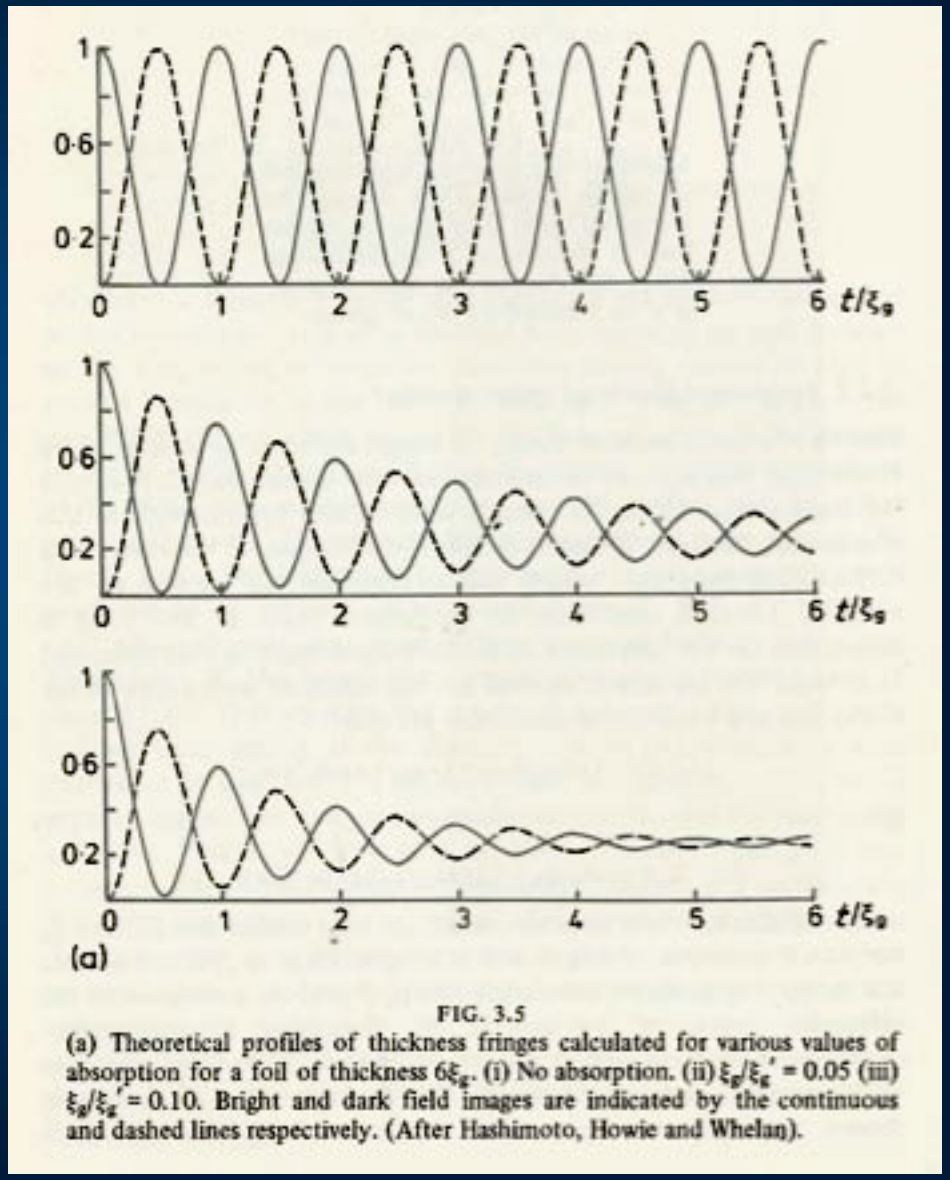

FIG. 3.5

(a) Theoretical profiles of thickness fringes calculated for various values of absorption for a foil of thickness $6\xi_g$. (i) No absorption. (ii) $\xi_g/\xi_g' = 0.05$ (iii) $\xi_g/\xi_g' = 0.10$. Bright and dark field images are indicated by the continuous and dashed lines respectively. (After Hashimoto, Howie and Whelan).

The Howie-Whelan equations

$$\frac{d\phi_0}{dz} = -\frac{\pi}{\xi'_0}\phi_0 + \pi i\left(\frac{1}{\xi_g} + i\frac{1}{\xi'_g}\right) e^{2\pi i \mathbf{g}.\mathbf{R}(z)}\,\phi_g$$

$$\frac{d\phi_g}{dz} = \pi i\left(\frac{1}{\xi_g} + i\frac{1}{\xi'_g}\right) e^{-2\pi i \mathbf{g}.\mathbf{R}(z)}\,\phi_0 + \left(2\pi i S_g - \frac{\pi}{\xi'_0}\right)\phi_g$$

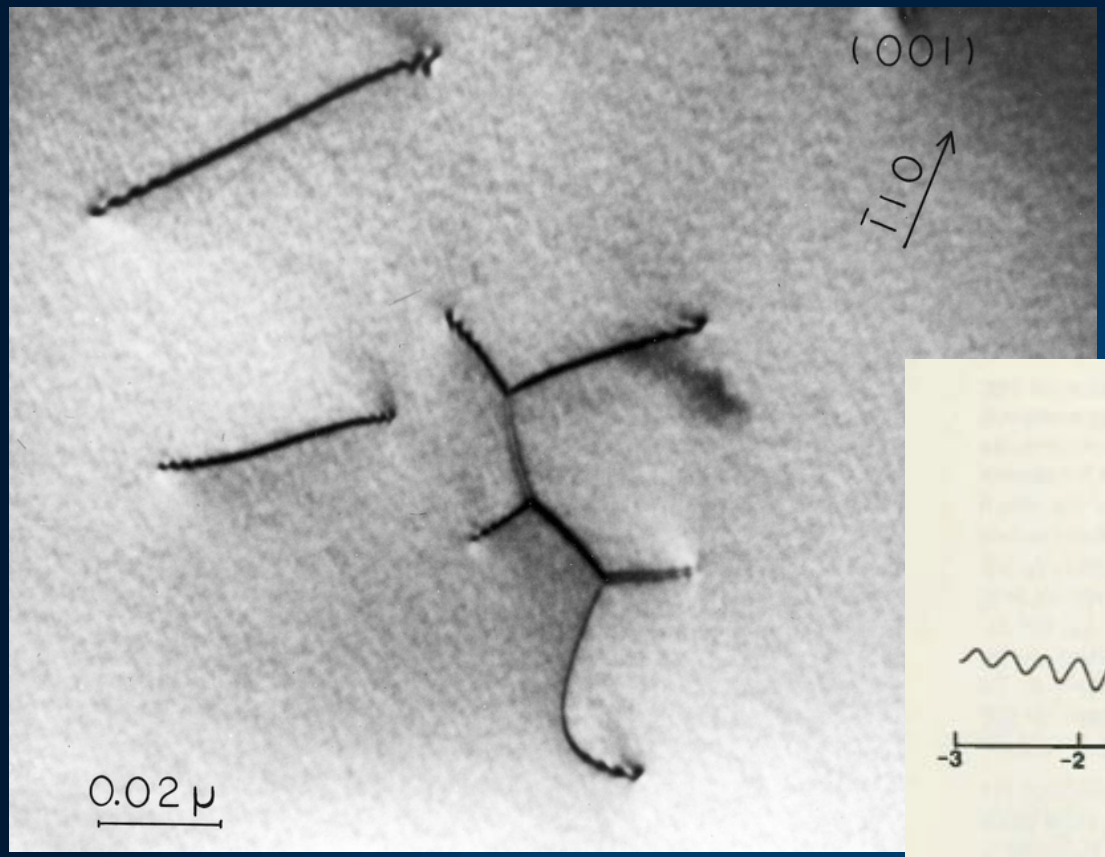

Maximize Contrast with s > 0.
Dark Field Images are Symmetric

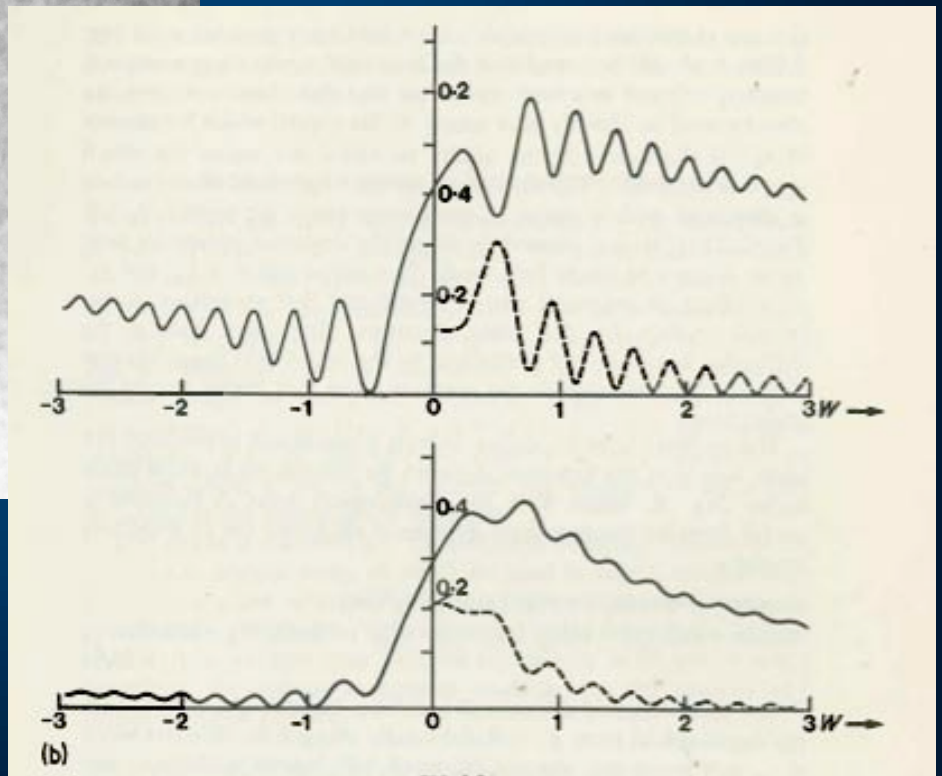

FIG. 3.5

(b) Rocking curves calculated for (i) $\xi_g/\xi_g' = 0.05$ and (ii) $\xi_g/\xi_g' = 0.1$ showing the bright-field curves (full line) are asymmetric about w = 0, whereas the dark-field (broken lines) are symmetrical.

e 000480
00 £34£

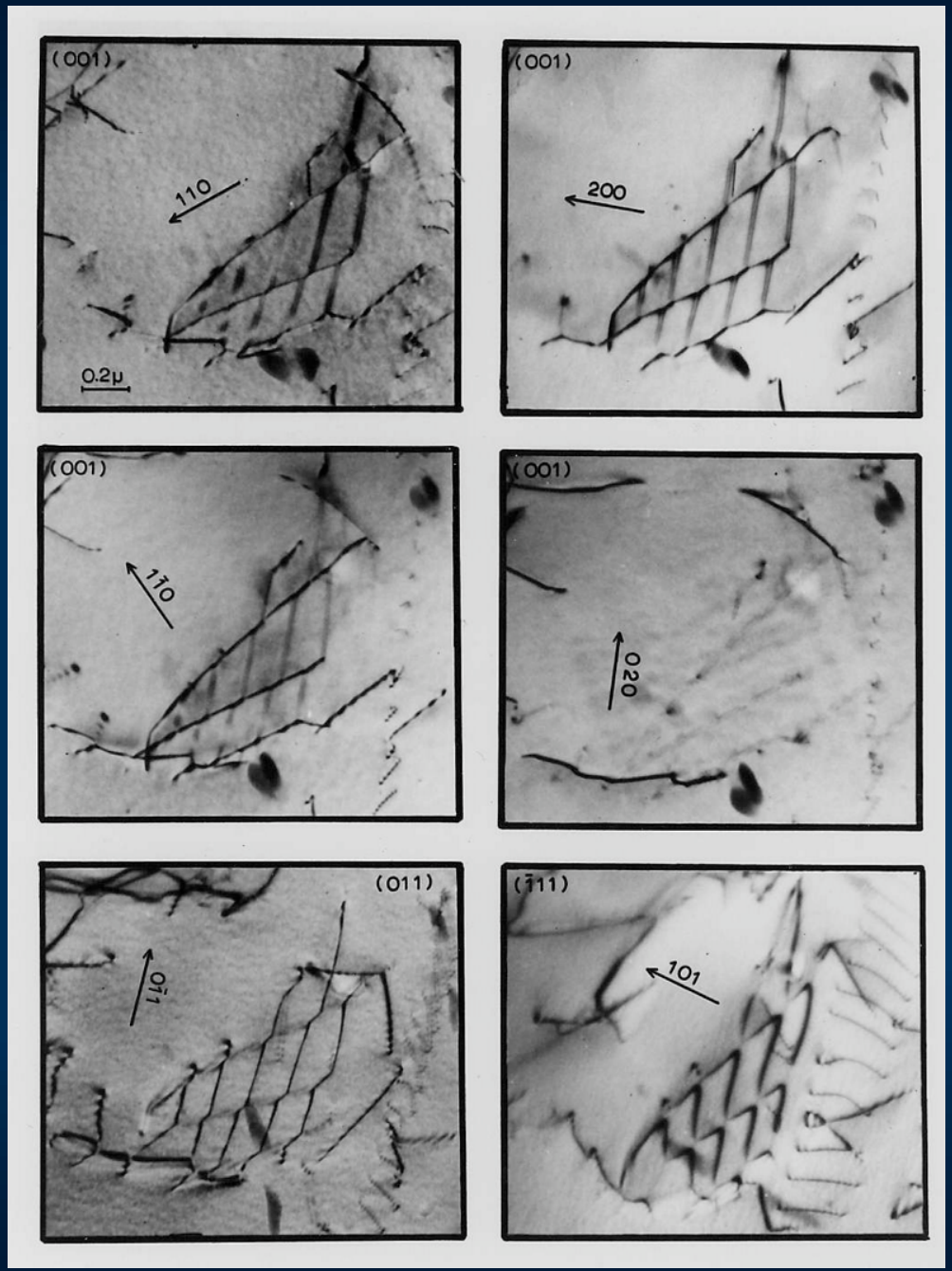
(001)
110
0.2μ
(001)
200
(001)
110
(001)
020
(011)
011
(111)
101

(1) Dislocations are most easily visible and the images broadest when $\mathbf{s} = 0$. Images for which $\mathbf{g}\cdot\mathbf{b} \geqslant 2$ show much stronger contrast for the same value of $\mathbf{s}$ than those for which $\mathbf{g}\cdot\mathbf{b} = 1$ or 0. At $\mathbf{s} = 0$, images for which $\mathbf{g}\cdot\mathbf{b} = 2$ show double images, and as $\mathbf{s}$ is increased one of the images fades away. Images for which $\mathbf{g}\cdot\mathbf{b} = 0$ also show double images at $\mathbf{s} = 0$ but the two peaks fade away together as $\mathbf{s}$ is increased. The images for which $\mathbf{g}\cdot\mathbf{b} = 1$ also fade away as $\mathbf{s}$ is increased and become so much weaker than images for which $\mathbf{g}\cdot\mathbf{b} = 2$ that they can be confused with images for which $\mathbf{g}\cdot\mathbf{b} = 0$. Because the background intensity in dark field becomes very small at large values of $\mathbf{s}$ (cf. Fig. 5.3(b)) weak images can be observed as bright lines on a dark background. At small values of $\mathbf{s}$ the bright and dark field images appear qualitatively similar.

(2) Dislocations running from top to bottom of a foil show oscillatory contrast when imaged at $\mathbf{s} \sim 0$. This contrast is damped out as $\mathbf{s}$ is increased. Images taken in bright field with a given diffracting vector give similar oscillatory contrast to that observed in dark field for the same sense of $\mathbf{g}$ for the part of the dislocation at the top of the foil.

(3) The image of a dislocation lies to one side of a dislocation provided $\mathbf{g}\cdot\mathbf{b} \neq 0$ and $\mathbf{s} \neq 0$. The origin of this can be seen from simple diagrams representing the strain fields around dislocations. The displacements on one side of an edge dislocation can be seen to rotate the crystal towards the Bragg condition (thus giving strong contrast) and on the other side away from this condition. The side to which the image lies is given by the sign of $(\mathbf{g}\cdot\mathbf{b})\,\mathbf{s}$ and the magnitude of the shift by the magnitude of $(\mathbf{g}\cdot\mathbf{b})\,\mathbf{s}$. Thus when $\mathbf{g}\cdot\mathbf{b} = 0$ the image is centred on the dislocation. An indication that $\mathbf{g}\cdot\mathbf{b} = 0$, even when this condition gives strong residual contrast can therefore be obtained by reversing $\mathbf{g}$; the absence of an image shift for $|s\xi| > 1$ implies that $\mathbf{g}\cdot\mathbf{b} = 0$.

(4) The image of a dislocation reverses top to bottom and side to side if $\mathbf{g}$ is reversed. A closely spaced dislocation dipole can give apparently more complex behaviour on reversing $\mathbf{g}$ since the images of the dislocations may overlap.

g[hkl]	b[hkl]	g.b
[100]	[100], [010], [001]	1 , 0 , 0
[110]	[100], [010], [001]	1, 1, 0
[111]	[100], [010], [001]	1, 1, 1
[110]	[110], [101], [011]	2, 1, 1
[1-10]	[110], [101], [011]	0, 1, -1

0 = Out of Contrast 1 = In-Contrast 2 = Double Contrast

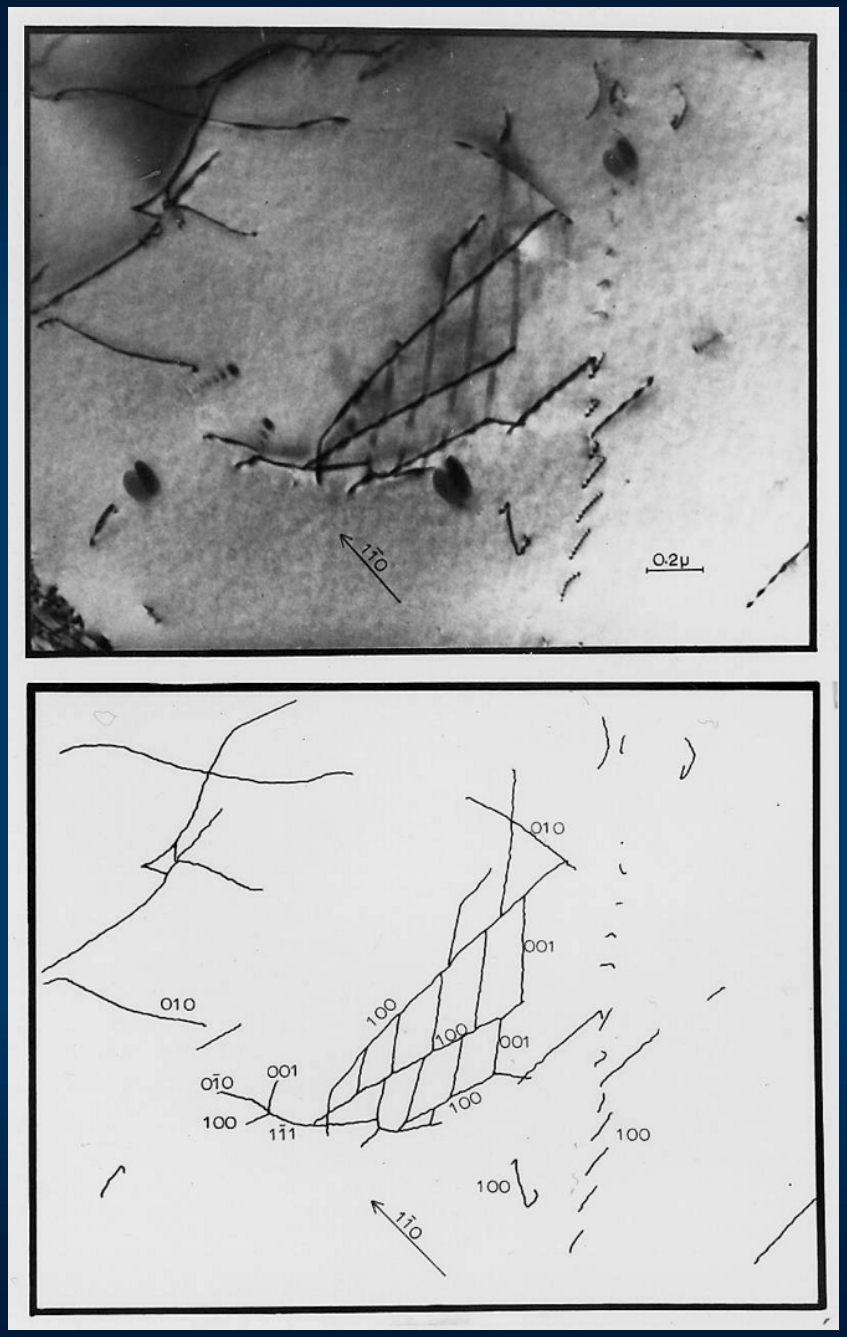
1$\bar{1}$0
0.2μ
010
001
100
100
001
010
001
0$\bar{1}$0
100
1$\bar{1}$1
100
100
100
1$\bar{1}$0

Specimen Holders

Single-titl holder
Double-tilt holder
Low-background holder
Heating holder
Cooling holder
Cryo-transfer holder

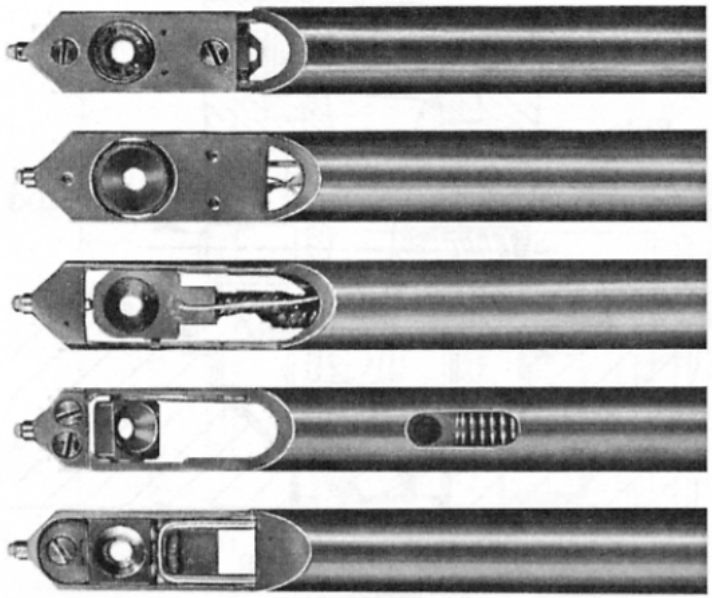

Figure 8.8. Examples of different designs for the side-entry holder. From the top, they are: a rotation holder, a heating holder, a cooling holder, a double-tilt holder, and a single-tilt holder.

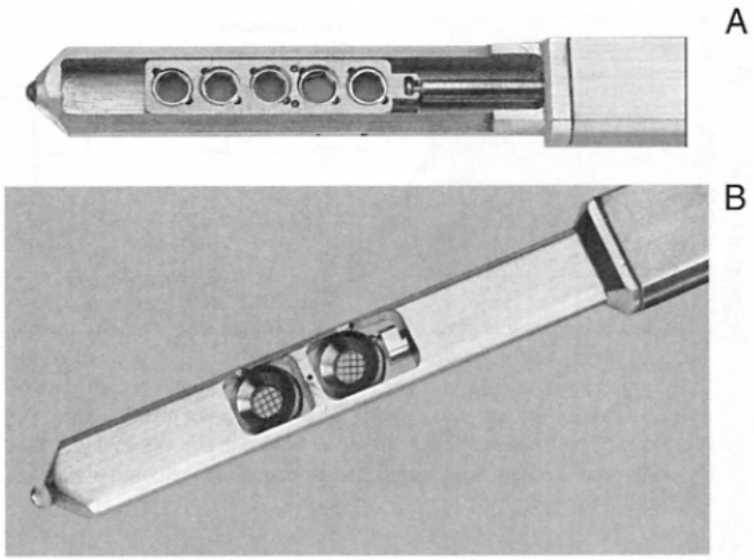

Figure 8.9. Multiple-specimen holders. (A) Five-specimen single-tilt and (B) two-specimen double-tilt.

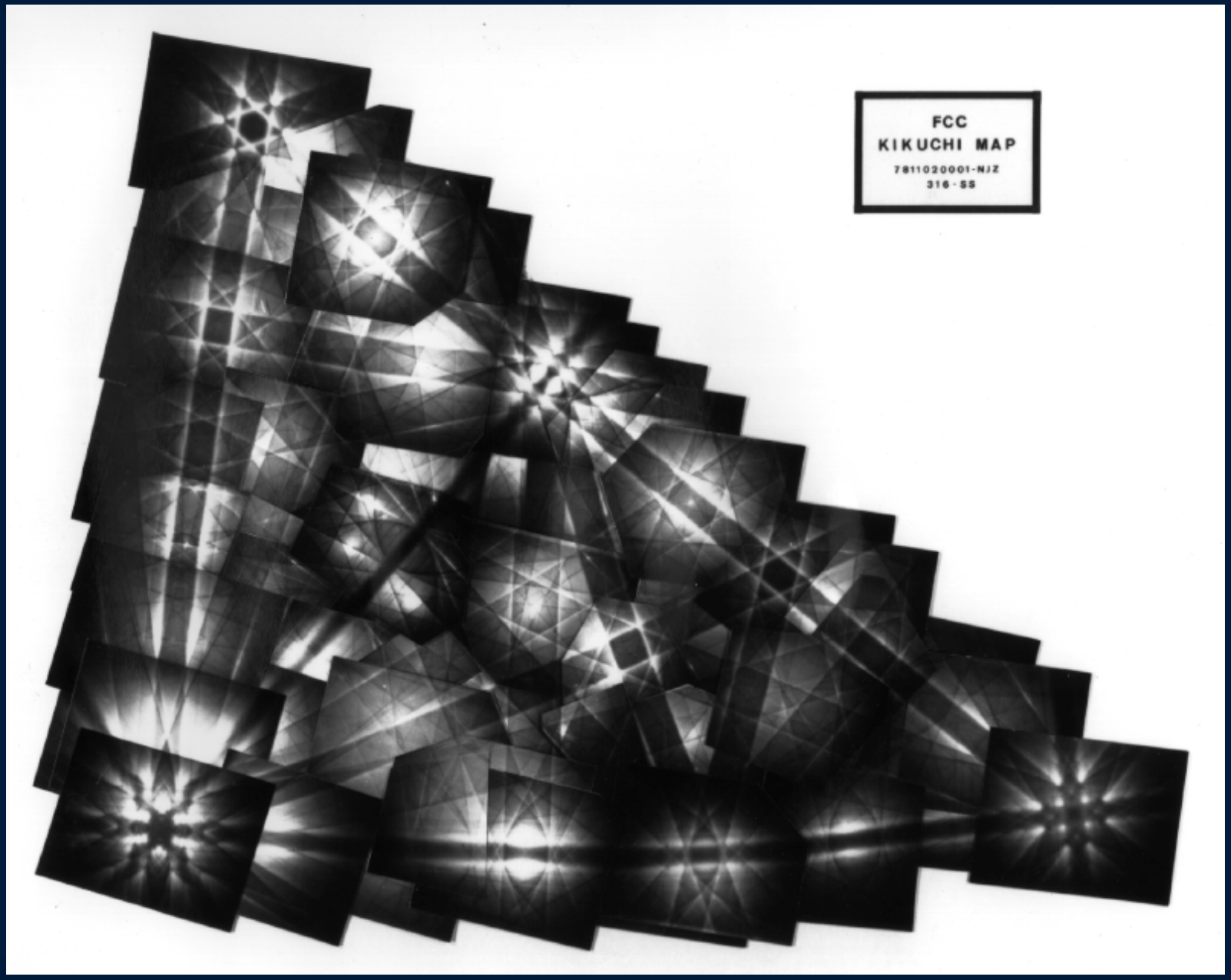
FCC
KIKUCHI MAP
7811020001-NJZ
316-SS

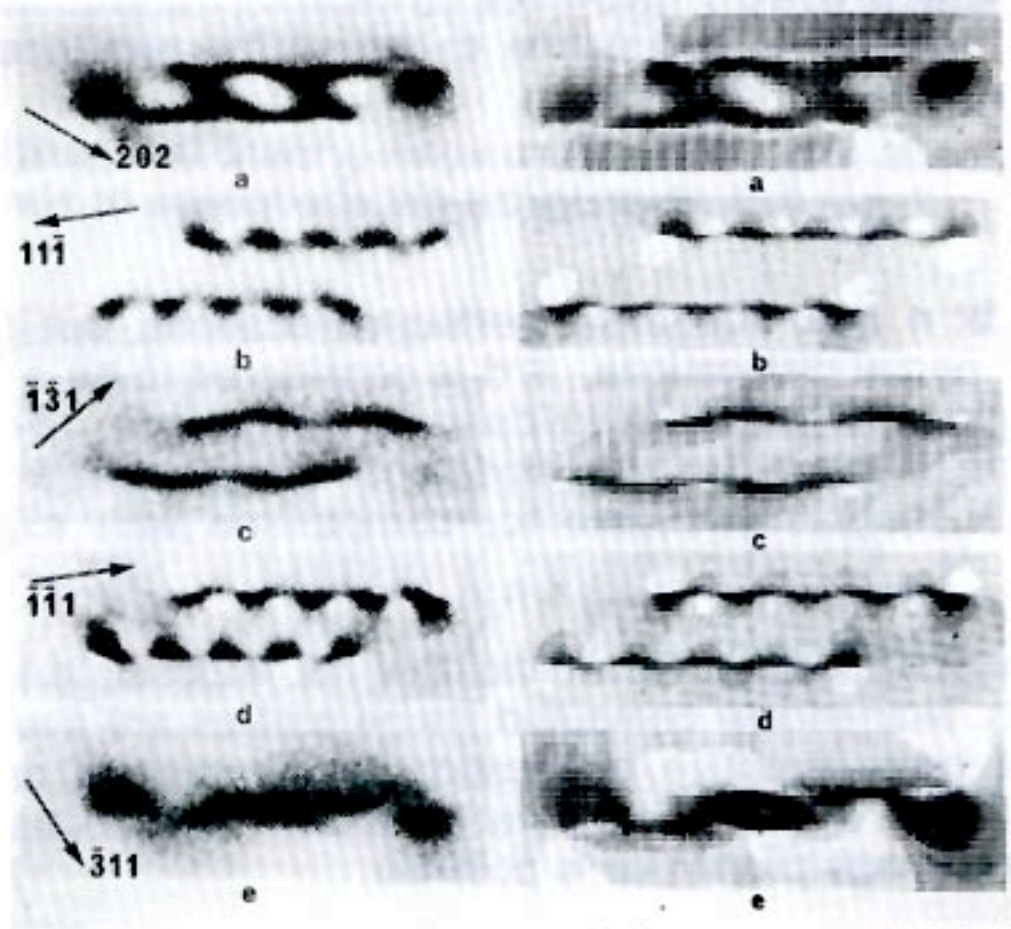

Figure 1.49 Examples of the quantitative agreement that can be achieved between observed and computed dislocation images. Left: observed images for different diffraction vectors Right: corresponding computer generated images.

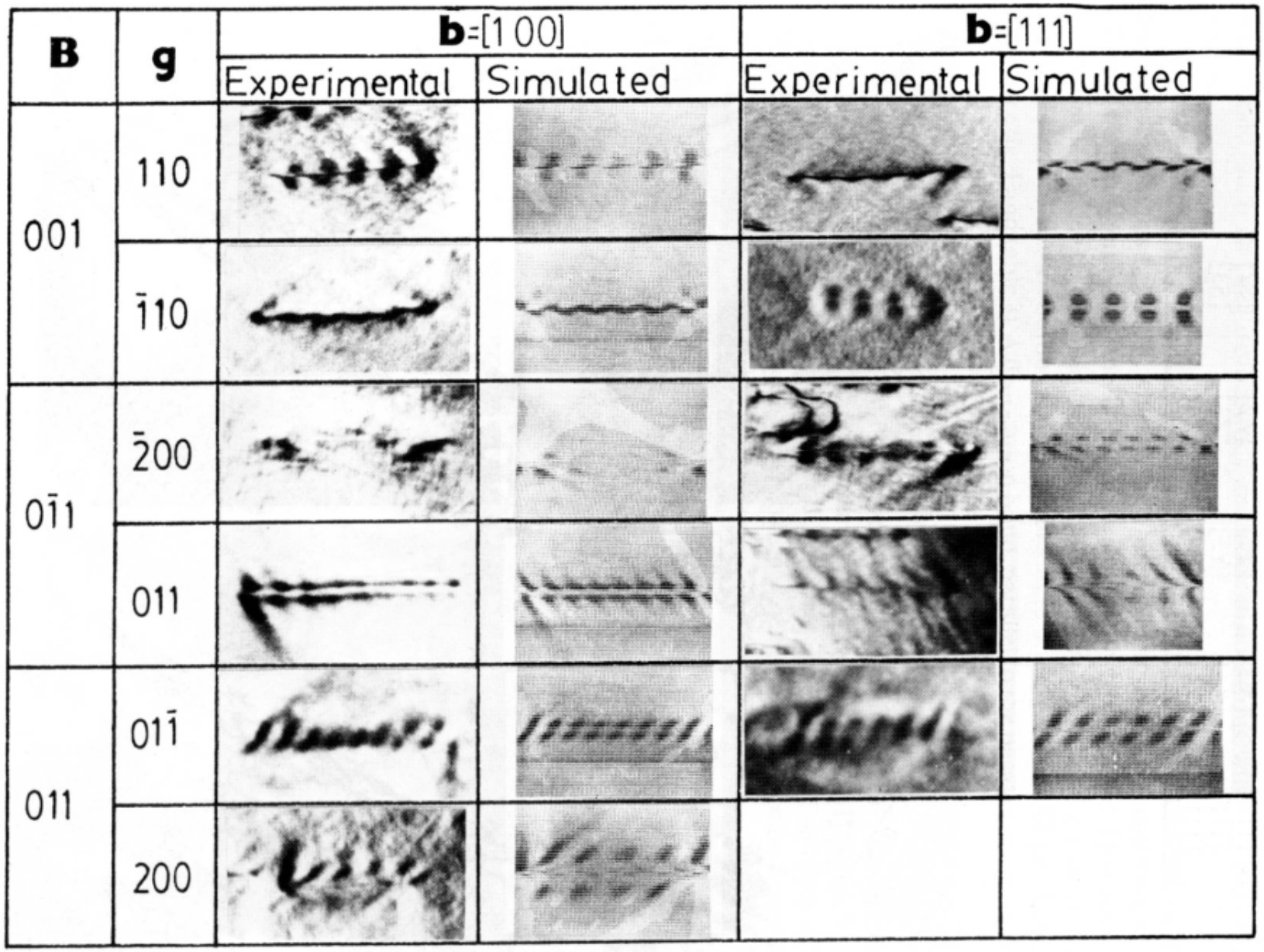
B
g
b=[100]
b=[111]
Experimental
Simulated
Experimental
Simulated
001
110
$\bar{1}10$
$0\bar{1}1$
$\bar{2}00$
011
011
$01\bar{1}$
200

Planar Defects

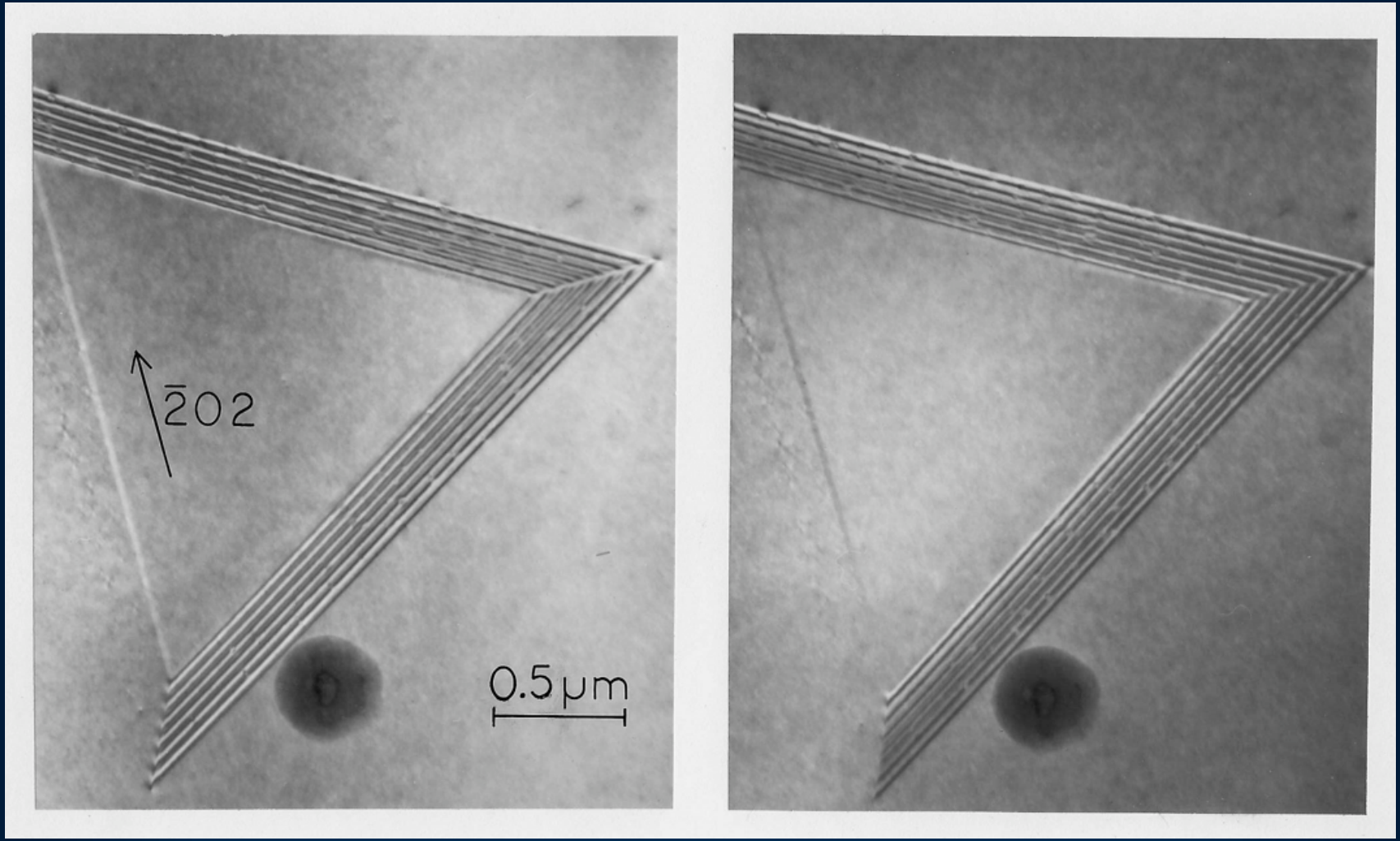

g.R = 0, 1, 2 … No Contrast

g.R < $\pm 2\pi/3$ Oscillitory Contrast

Symmetric BF, Asymmetric DF

Symmetry of the stacking faults images

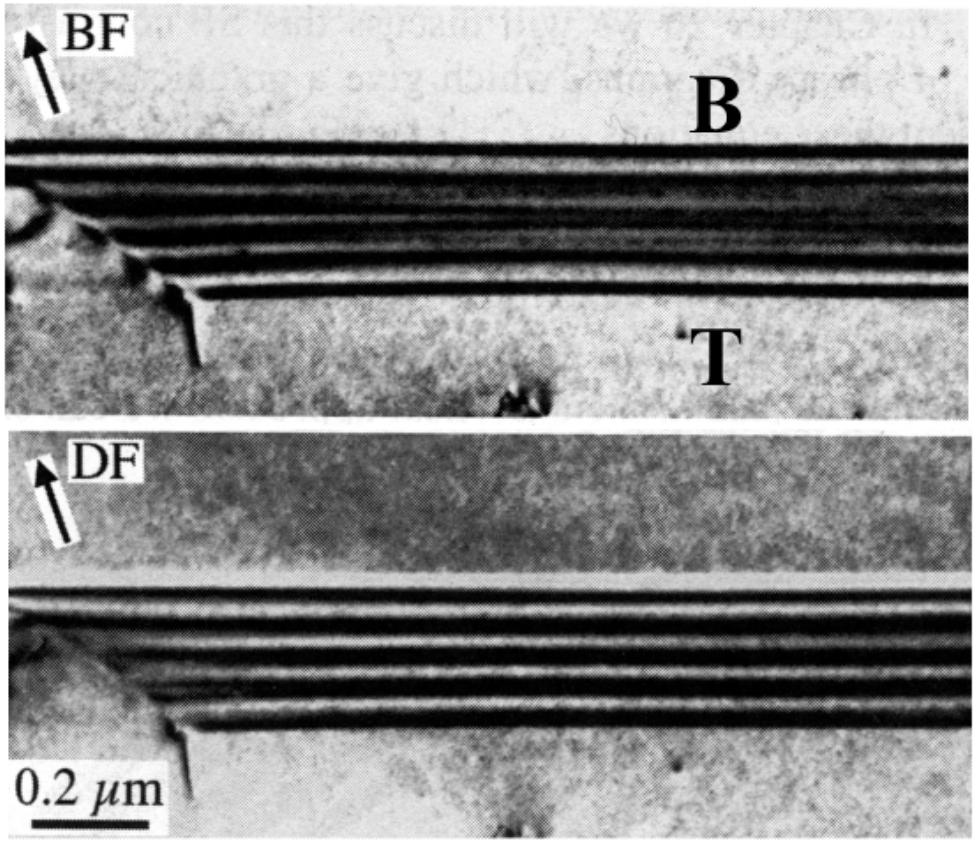

-The fringes at the top are the same in BF and DF images

-The fringes at the bottom are complementary

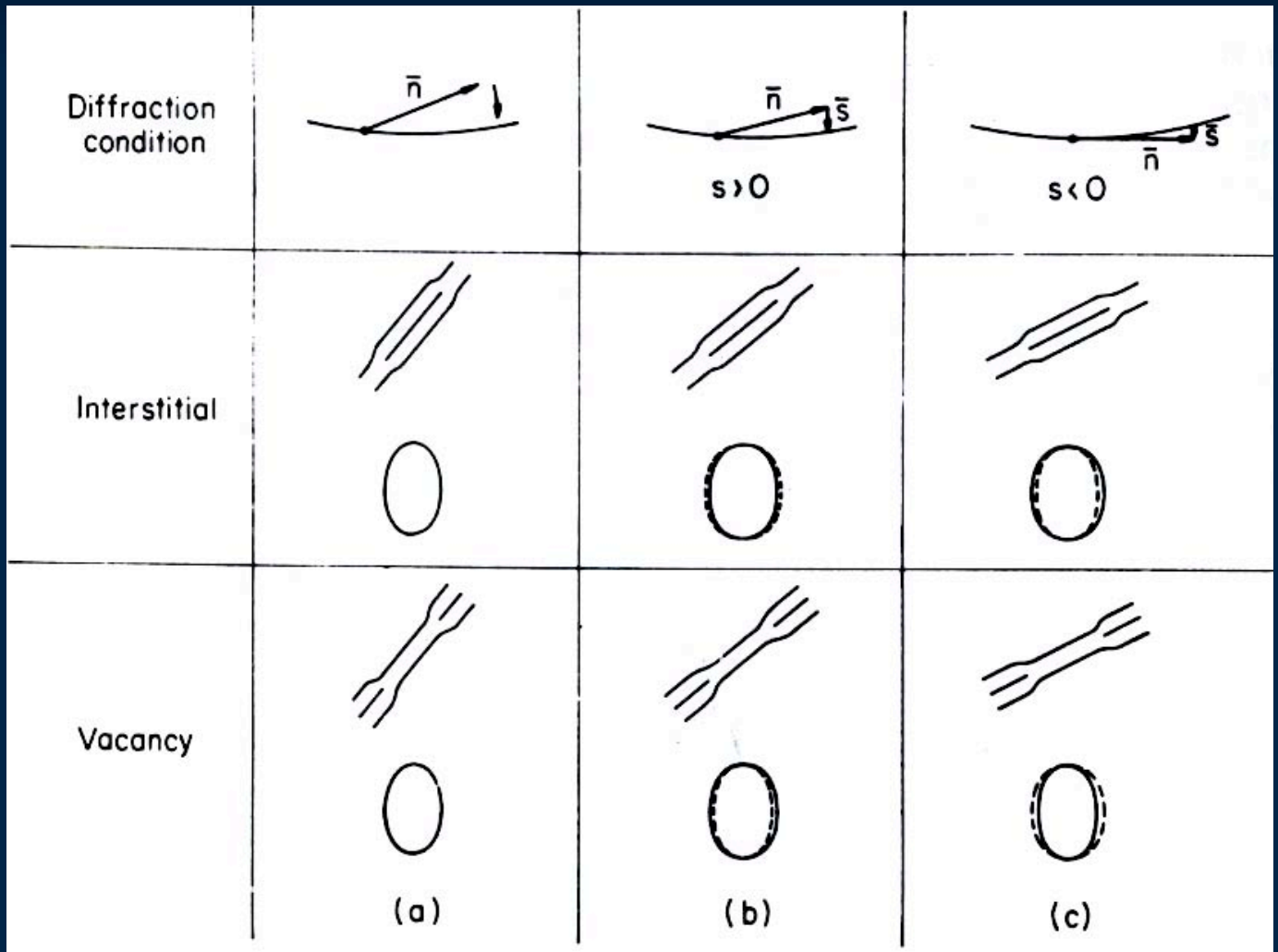

Figure 1.68 Contrast experiment allowing to determine the nature of dislocation loops. Diffraction vector n. The foil is tilted in the indicated sense.

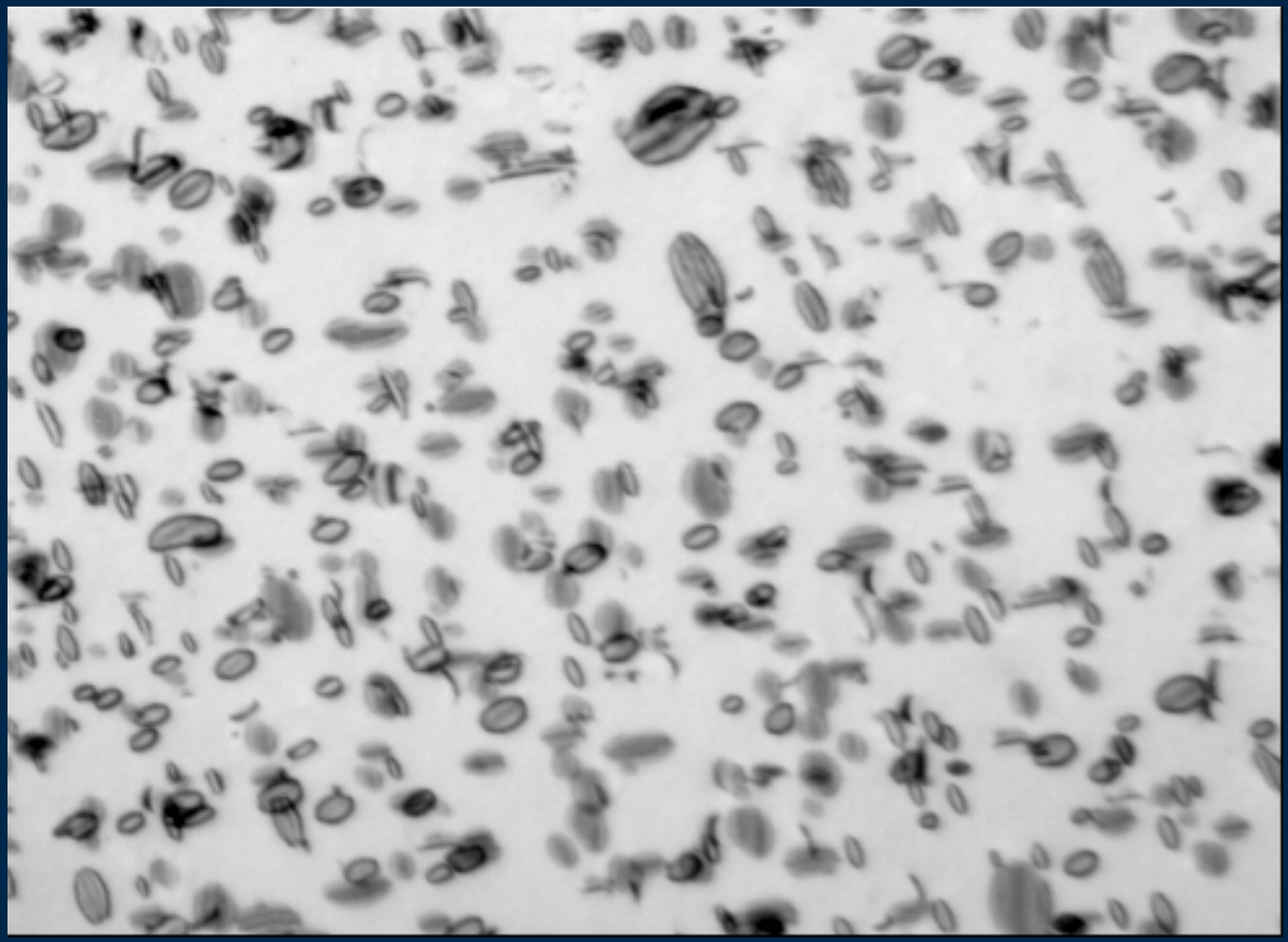

Radiation Damage in Materials

Damage Creation Event/Process

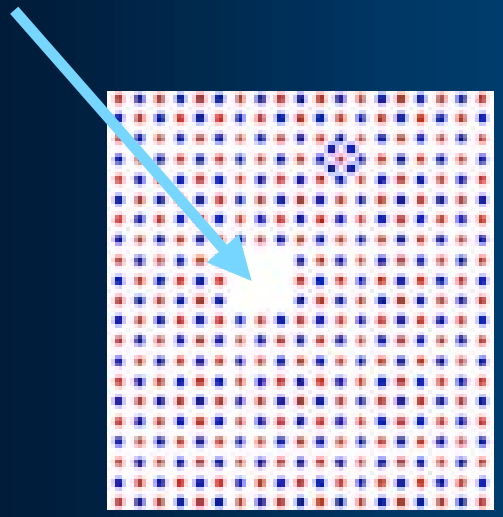

Mobile
Vacancy & Interstitials
Created

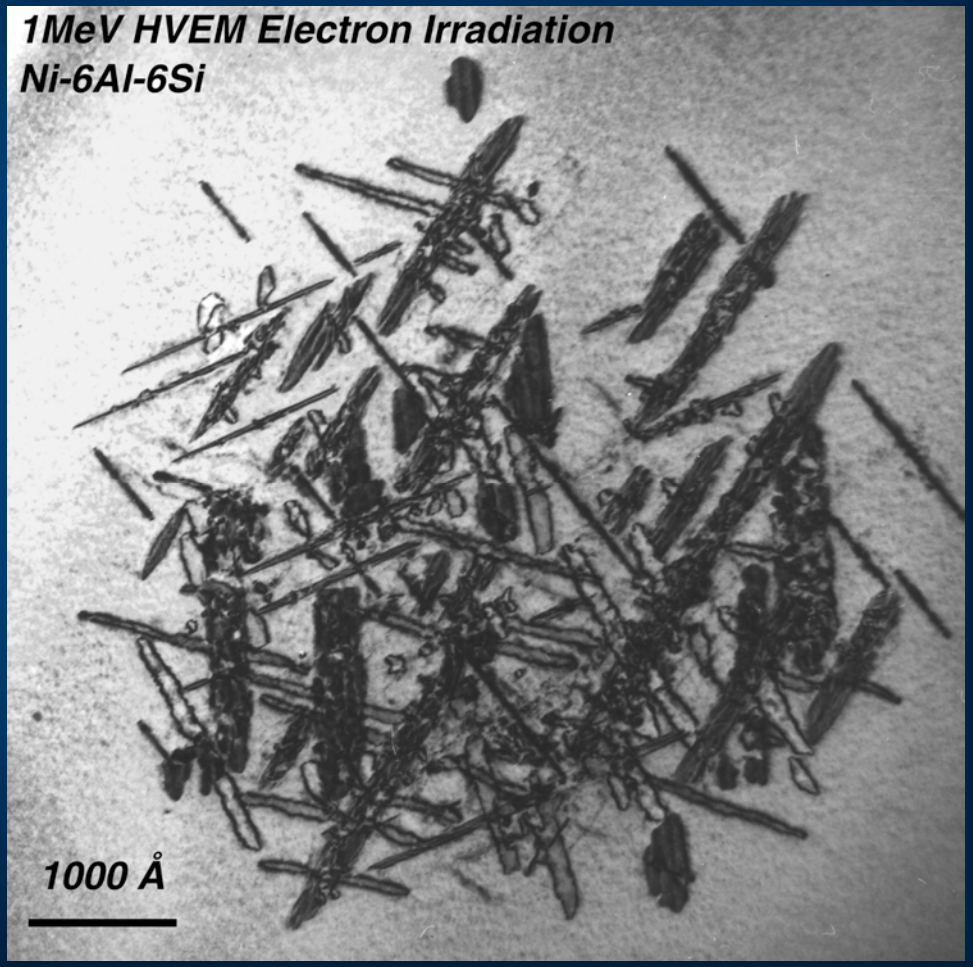

HREM - Phase Contrast Imaging

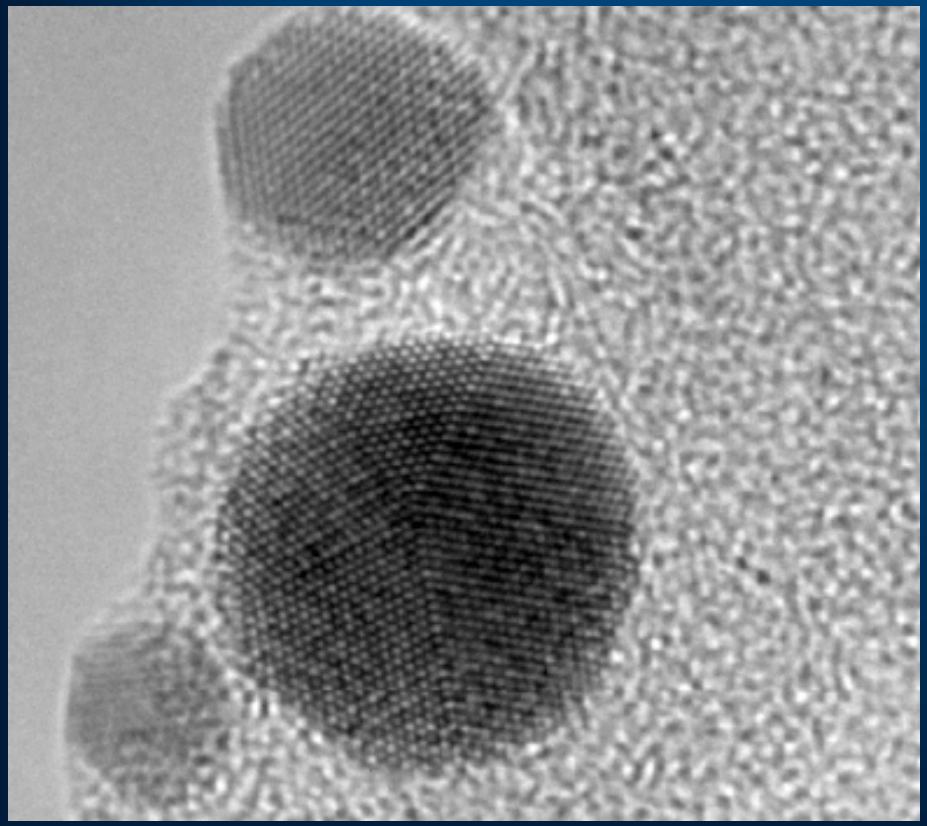

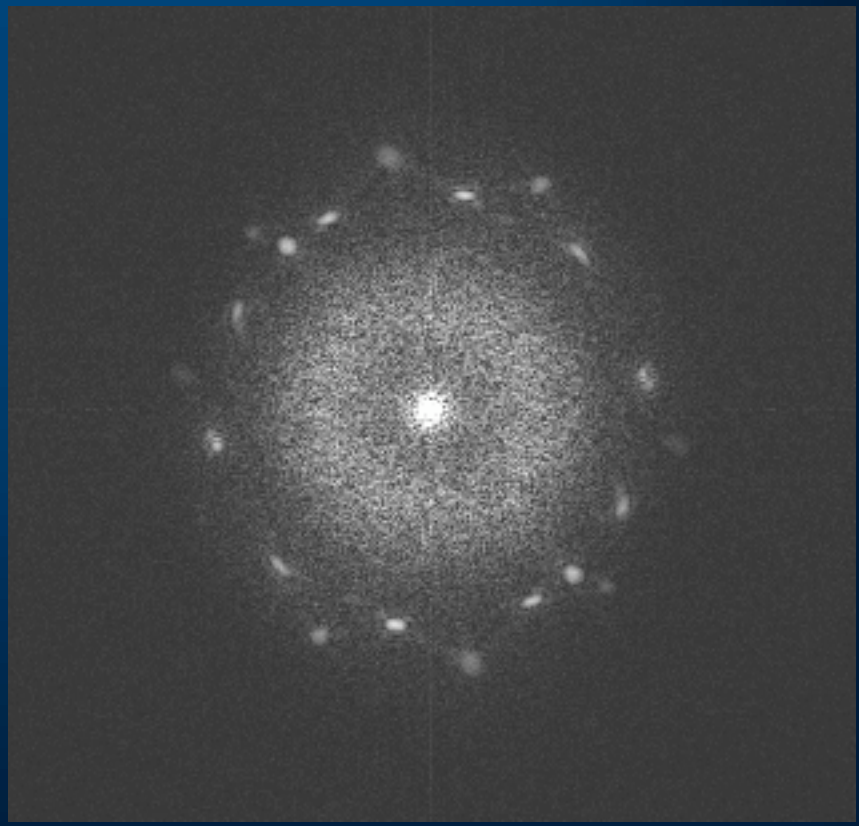

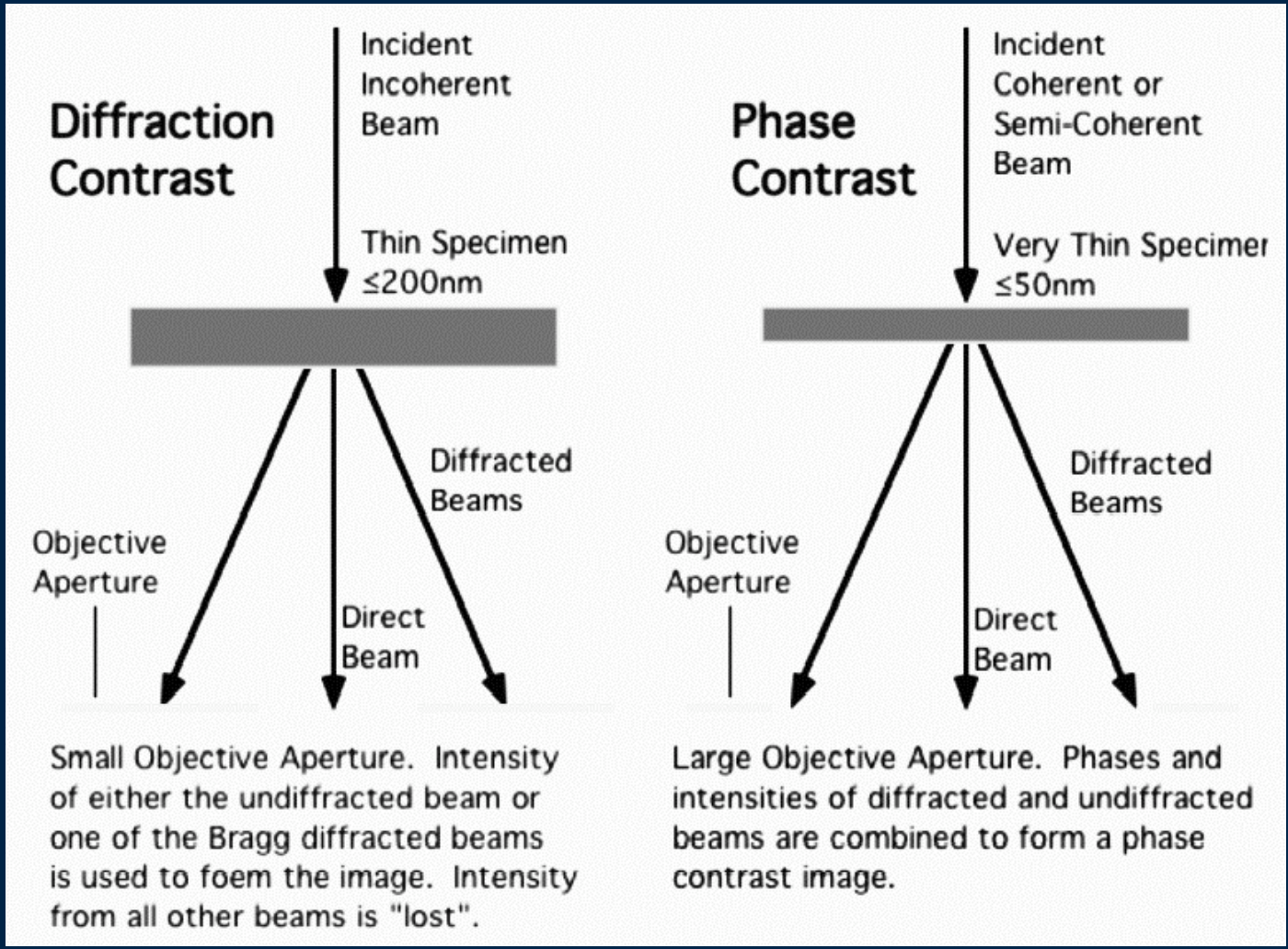
Diffraction Contrast
Incident Incoherent Beam
Thin Specimen ≤200nm
Diffracted Beams
Objective Aperture
Direct Beam
Small Objective Aperture. Intensity of either the undiffracted beam or one of the Bragg diffracted beams is used to foem the image. Intensity from all other beams is "lost".
Phase Contrast
Incident Coherent or Semi-Coherent Beam
Very Thin Specimer ≤50nm
Diffracted Beams
Objective Aperture
Direct Beam
Large Objective Aperture. Phases and intensities of diffracted and undiffracted beams are combined to form a phase contrast image.

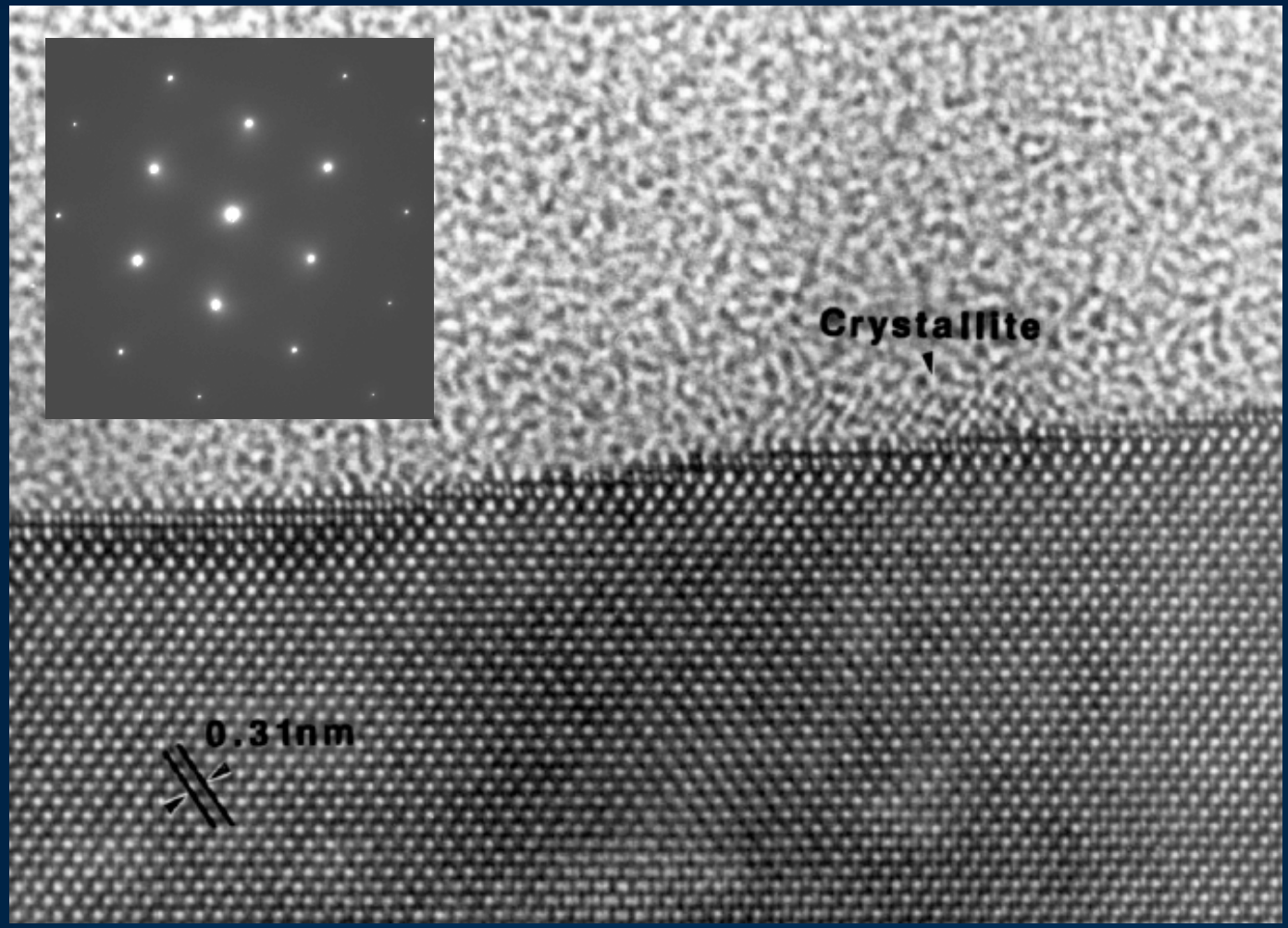

"Routine HREM"

Simplest HREM Imaging
2 Beam Lattice

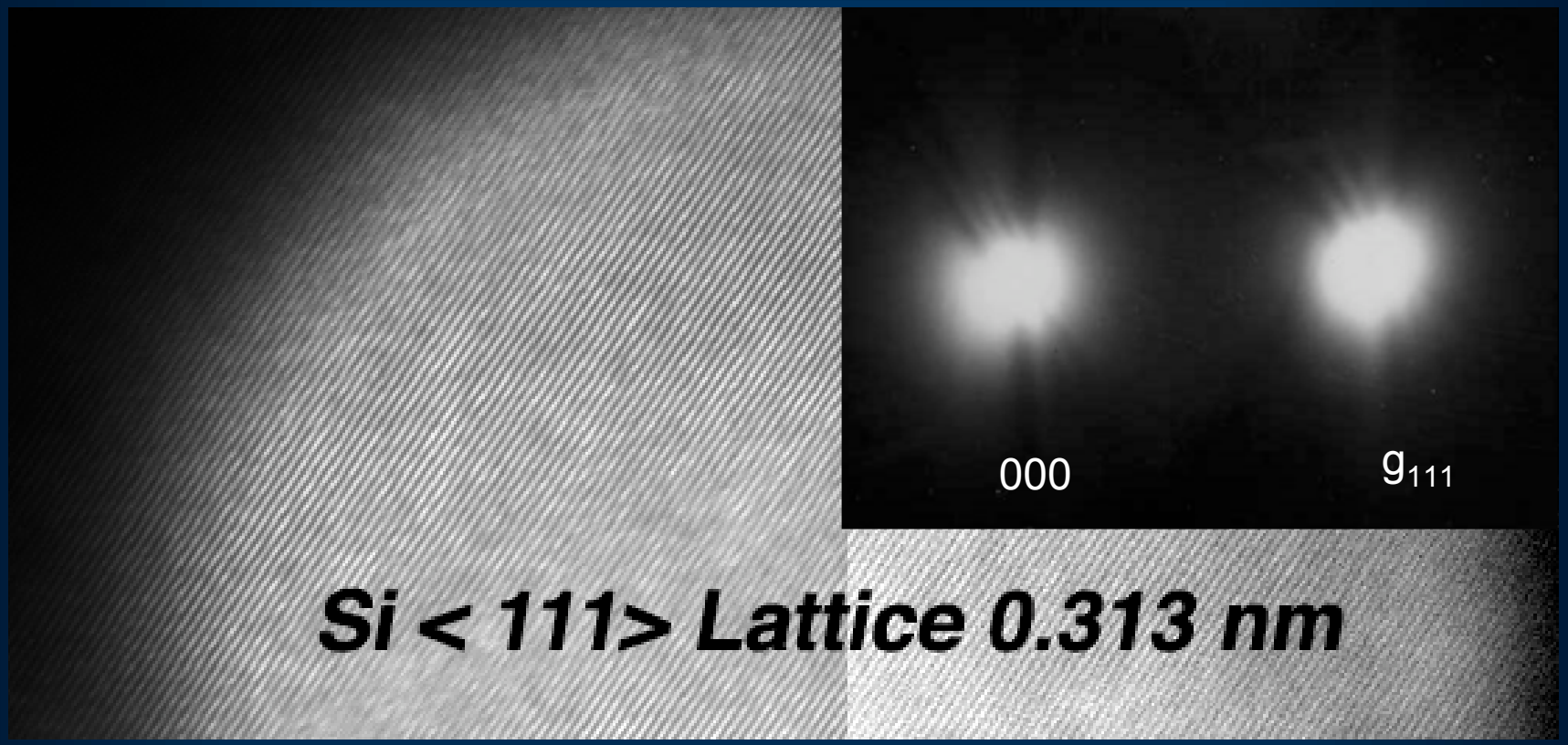

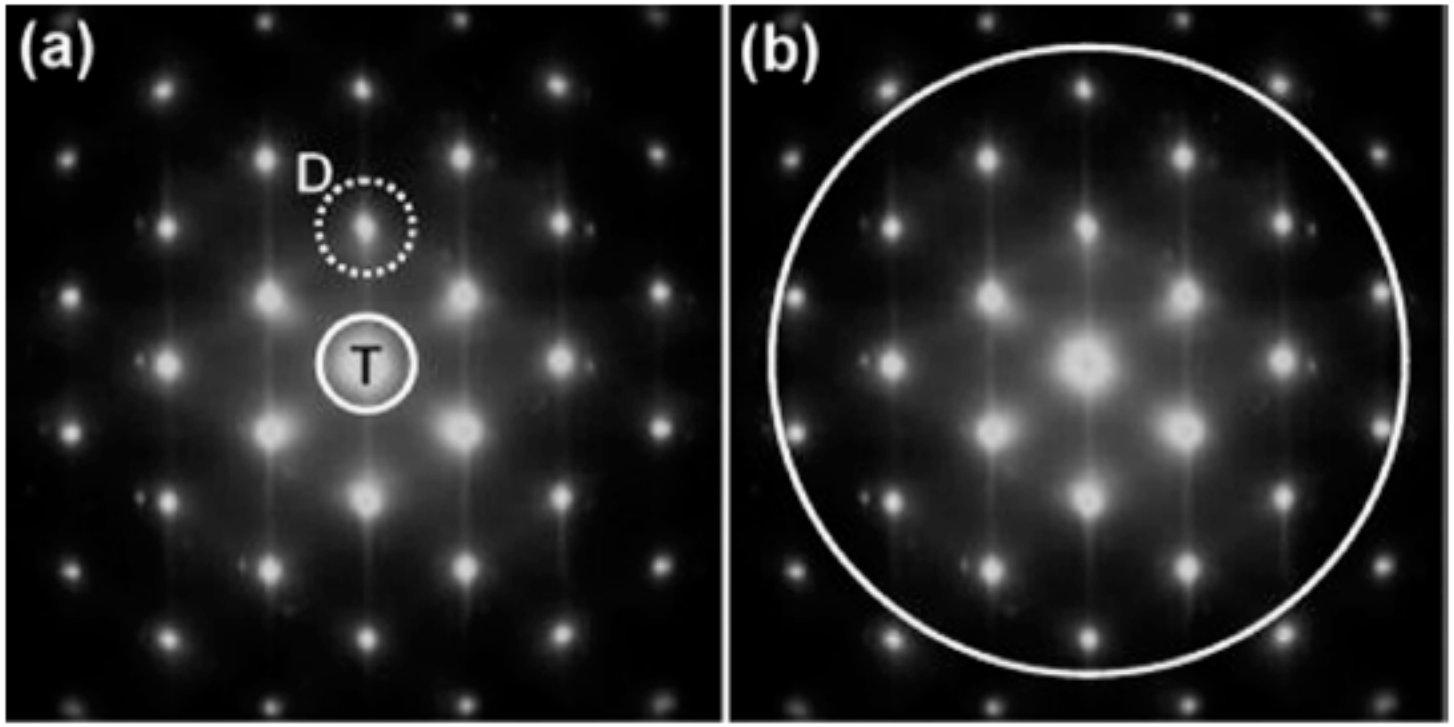

Fig. 6. The size and the position of the objective aperture for diffraction contrast (a) and phase interference contrast (b)

Image Formation in the High-Resolution TEM

- In the high-resolution TEM, the incident electron beam interacts strongly with the crystal, forming multiple diffracted beams that are brought together by the objective lens so they can interfere to create an image.
- ***TEM images are able to depict the projected atom columns because they are interference patterns of the directly transmitted beam with beams diffracted from the specimen.***
- Structural information from the specimen is encoded in the phase of the scattered electron waves [5]. Although the electron phase is not an observable (it is not gauge invariant [6]), phase differences can be measured by interference experiments such as imaging.
- At the "optimum" or "extended Scherzer" defocus [7], objective lens phase shifts allow interference of the scattered electron waves exiting the specimen to turn the relative phases of the waves into image peaks mapping the atom positions (at the resolution of the microscope).

[5] J.M. Cowley, Diffraction Physics (1975) North Holland / American Elsevier.
[6] H. Rose, Lectures on Charged Particle Optics, LBNL (2004)
[7] O. Scherzer, J. Appl. Phys. 20 (1949) 20-29.

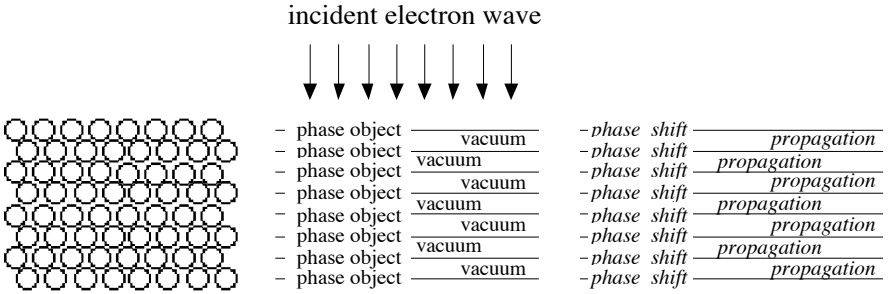

$$\psi(x,y)_V = \psi_{in}(x,y)_0 \exp\left(\sigma \int_0^{\varepsilon} V(xy,z)dz\right) = \psi_{in}(x,y)_0 \exp\left(i\sigma V_p(xy)_1\right)$$

$$\psi(x,y)_n \approx \frac{\exp ik'\varepsilon}{\varepsilon}\left[\psi_{in}(X,Y)_{n-1} \exp\left(i\sigma V_p(X,Y)_n\right)\right] \otimes \exp\left[\frac{ik'\varepsilon}{2\varepsilon}(X^2+Y^2)\right]$$

Phase of the exit wave depends upon the thickness & interference of the diffracted and transmitted beams in the specimen.

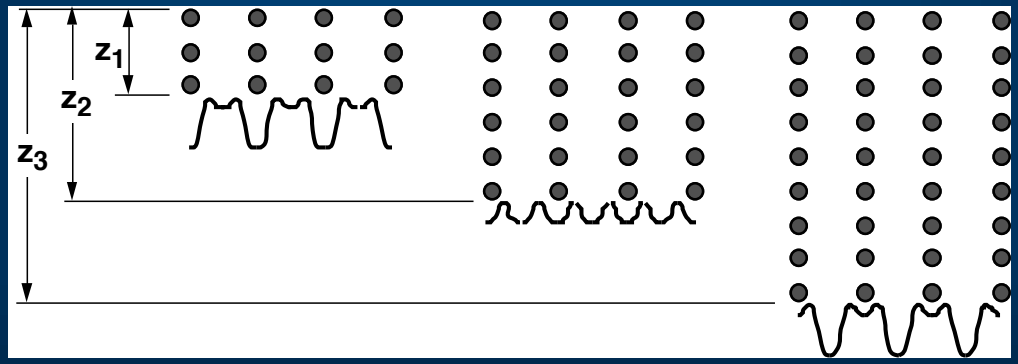

Dark Atoms

White Atoms

Dark
Atoms

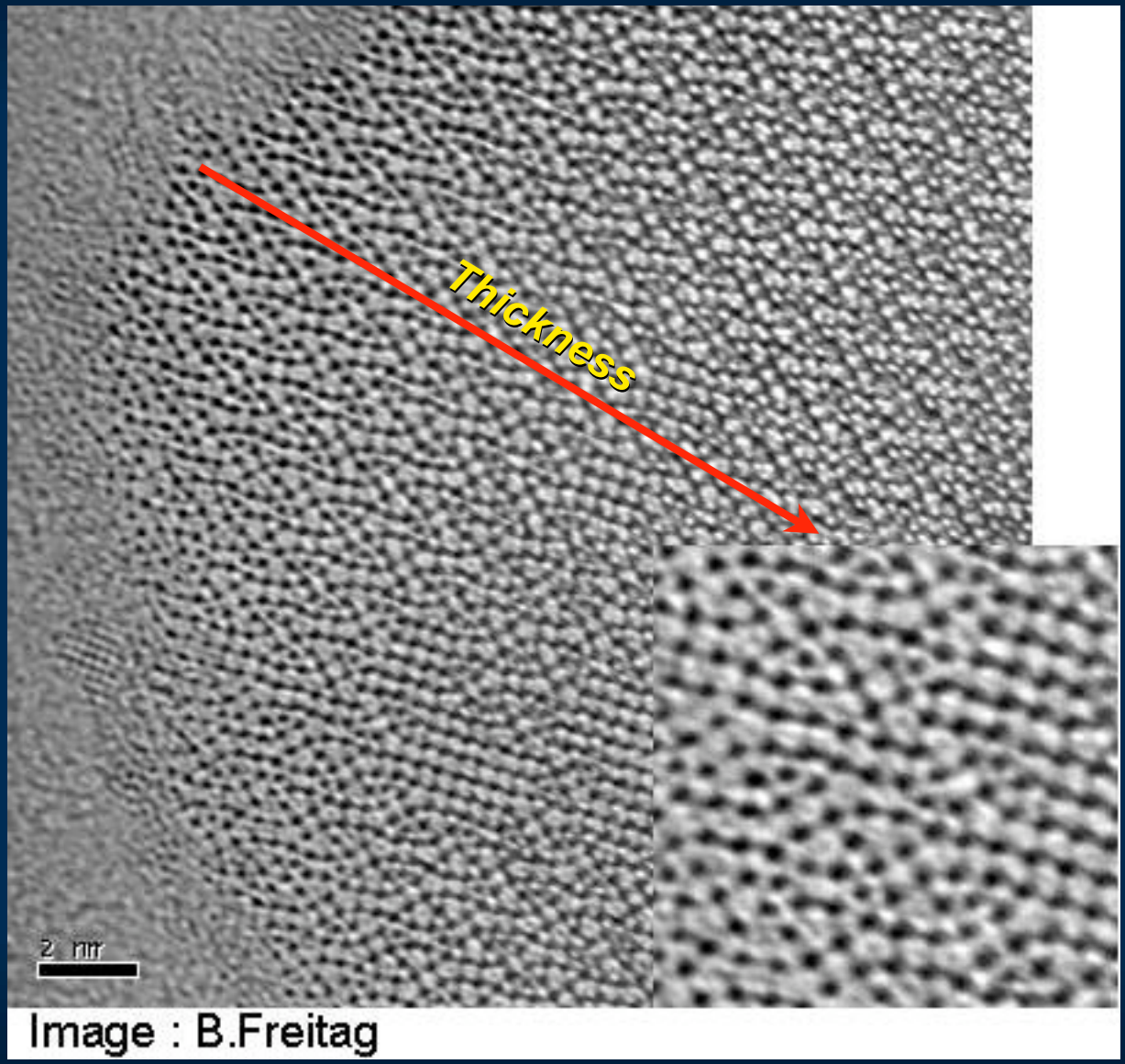

Image : B.Freitag

White
Atoms

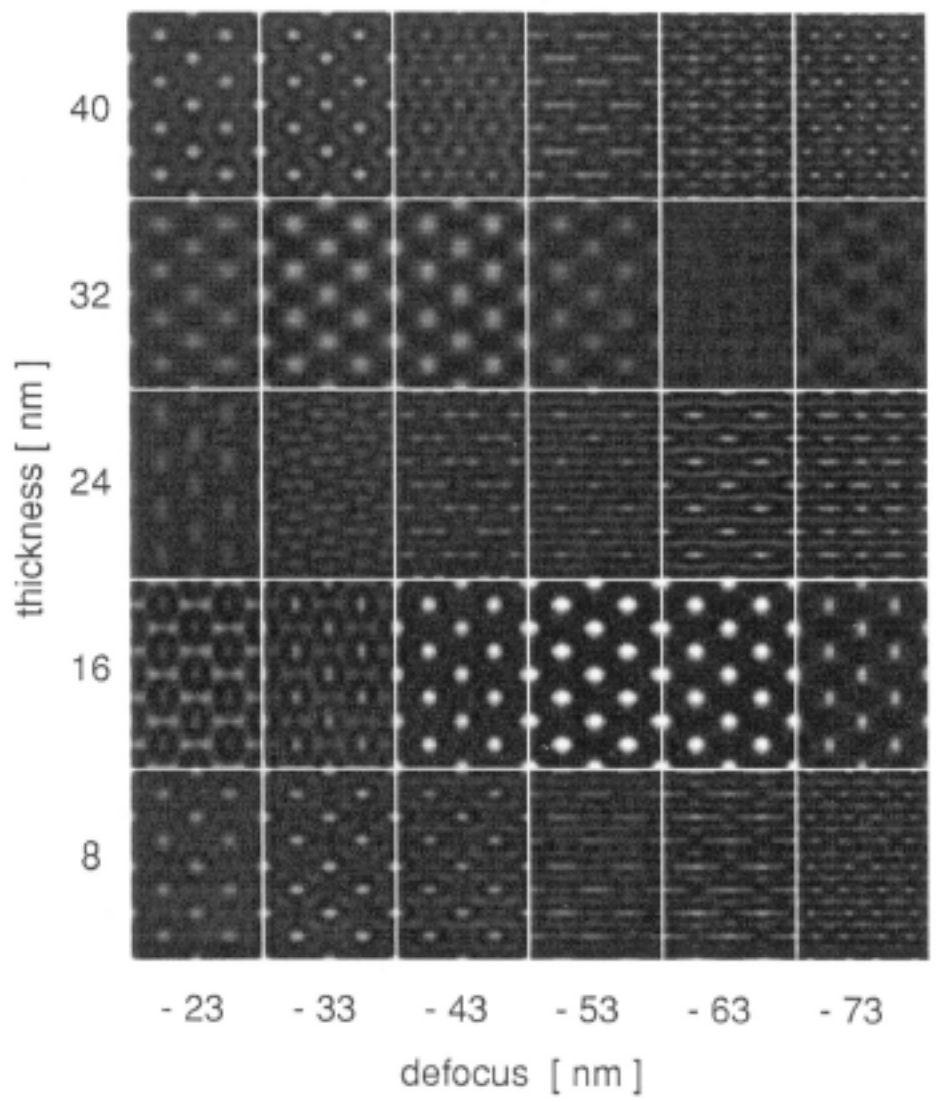

Fig. 15. A defocus - thickness map of the Fe_3Al intermetallics

Image Phase Shifts due to:

Defocus

$$\chi_2(\theta,\Delta z) = -\frac{2\pi}{\lambda}\Delta z\frac{\theta^2}{2} \qquad \Delta z = -1{,}2\sqrt{C_s\lambda}$$

Scherzer Defocus

Spherical Aberration

$$\chi_1(\theta) = -\frac{2\pi}{\lambda}C_s\frac{\theta^4}{4}$$

Contrast Transfer Function

$$T_C(\theta,\Delta z) = \exp i\left(\chi_1+\chi_2\right) = \exp i\left\{-\frac{2\pi}{\lambda}\left(C_s\frac{\theta^4}{4}+\Delta z\frac{\theta^2}{2}\right)\right\}$$

Temporal Coherence
(Chromatic Aberration)

$$E_T = \exp\left\{-\frac{\pi^2}{\lambda^2}(\Delta f)^2\theta^4\right\} \qquad \Delta f = C_c\left[\left(\frac{\Delta V}{V}\right)^2+\left(\frac{2\Delta I}{I}\right)^2+\left(\frac{\Delta E}{E}\right)^2\right]^{1/2}$$

Spatial Coherence
(Beam Convergence)

$$E_S = \frac{2J_1(x)}{x} \qquad x = 2\pi\alpha\left\{\Delta z\frac{\theta}{\lambda}+\left[\lambda C_s - i\pi(\Delta f)^2\right]\frac{\theta^3}{\lambda^2}\right\}$$

Total / System Transfer Function

$$T_R = T_C \,.\, E_T \,.\, E_S$$

Wave Function at the Detector

$$\tilde{\psi}_E(\vec{q})\,T(\vec{q},\Delta z)$$

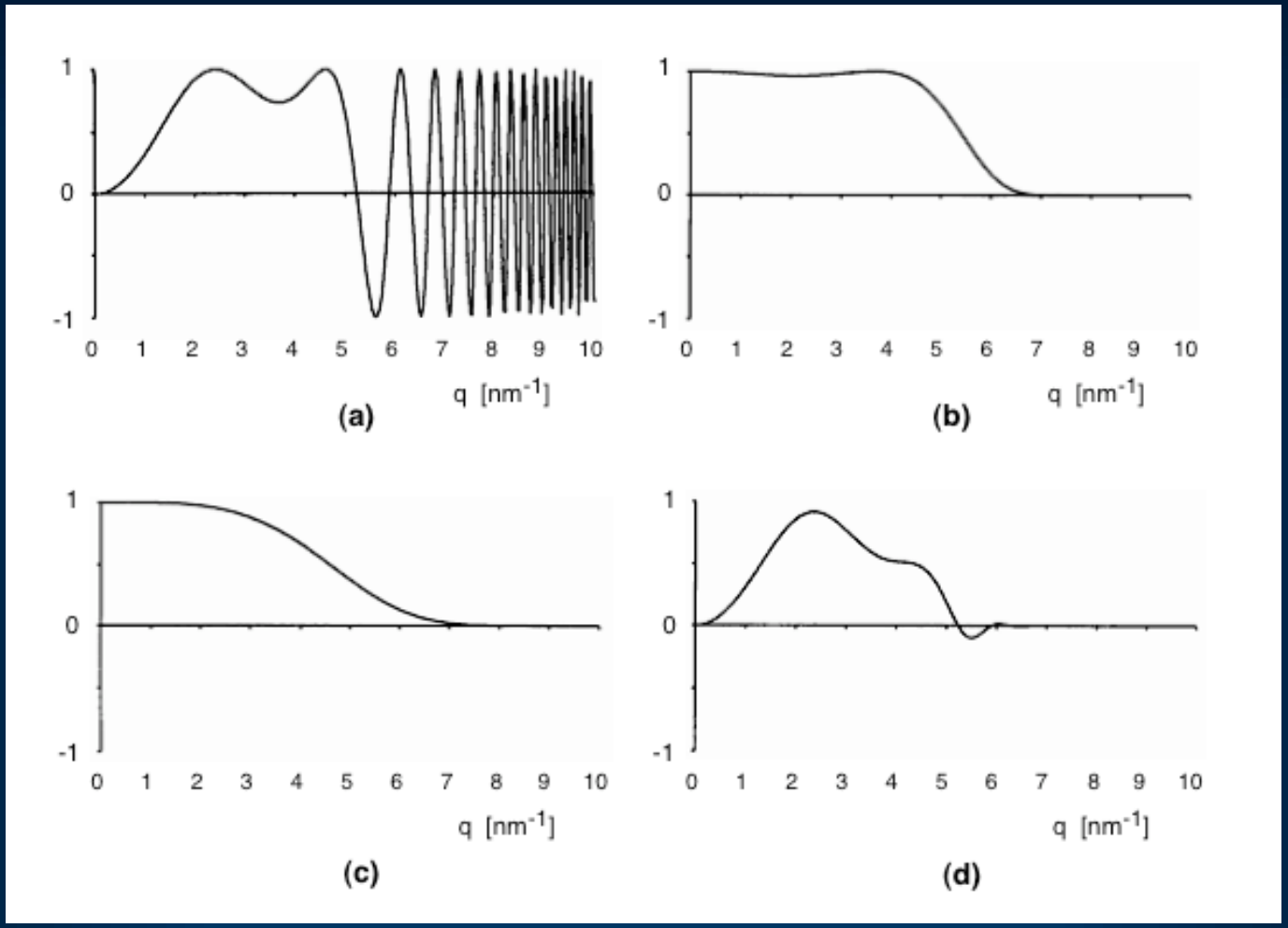

Fig. 8 : *Transfer function and its envelopes (Scherzer defocus)*

a) contrast transfer function
b) spatial coherence envelope
c) temporal coherence envelope
d) product (a)(b)*(c) – tranfer function in amplitude*

Phase Transfer in the High-Resolution TEM

Phase Contrast Transfer Function shows strength of transfer into image

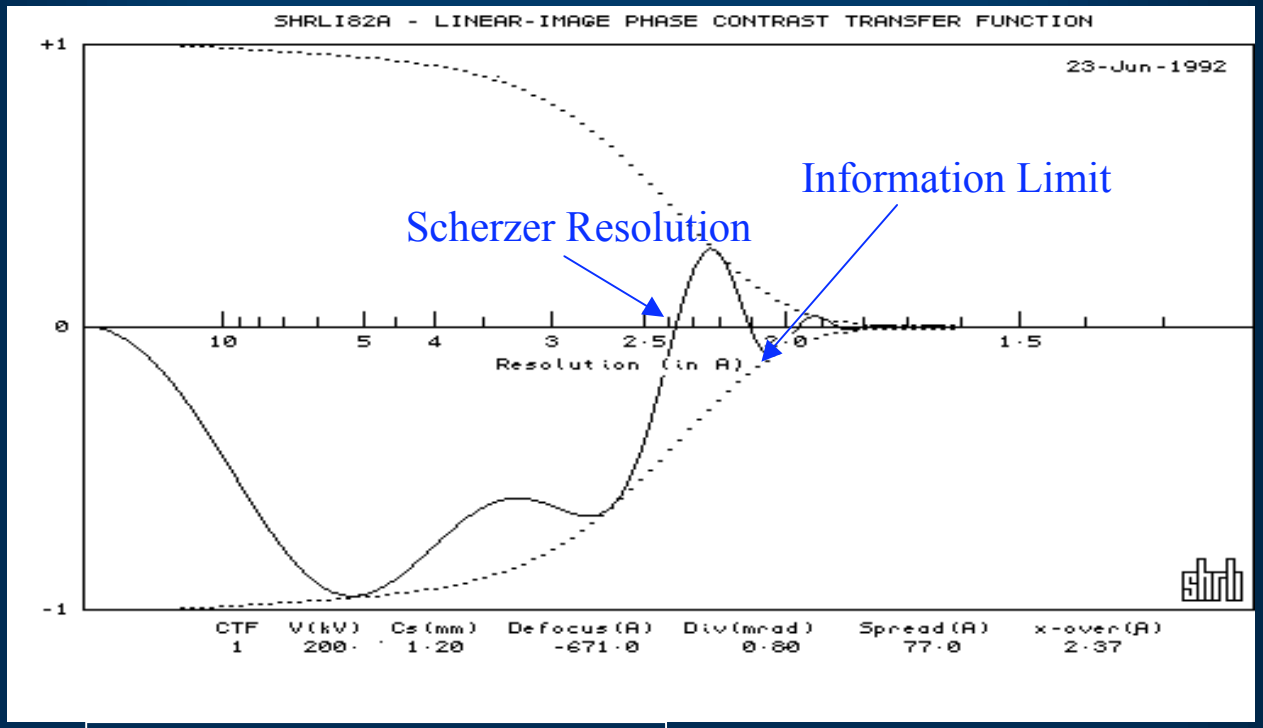

Same-sign transfer defines microscope resolution

End of transfer is the microscope's "information limit"

GaN and Sapphire

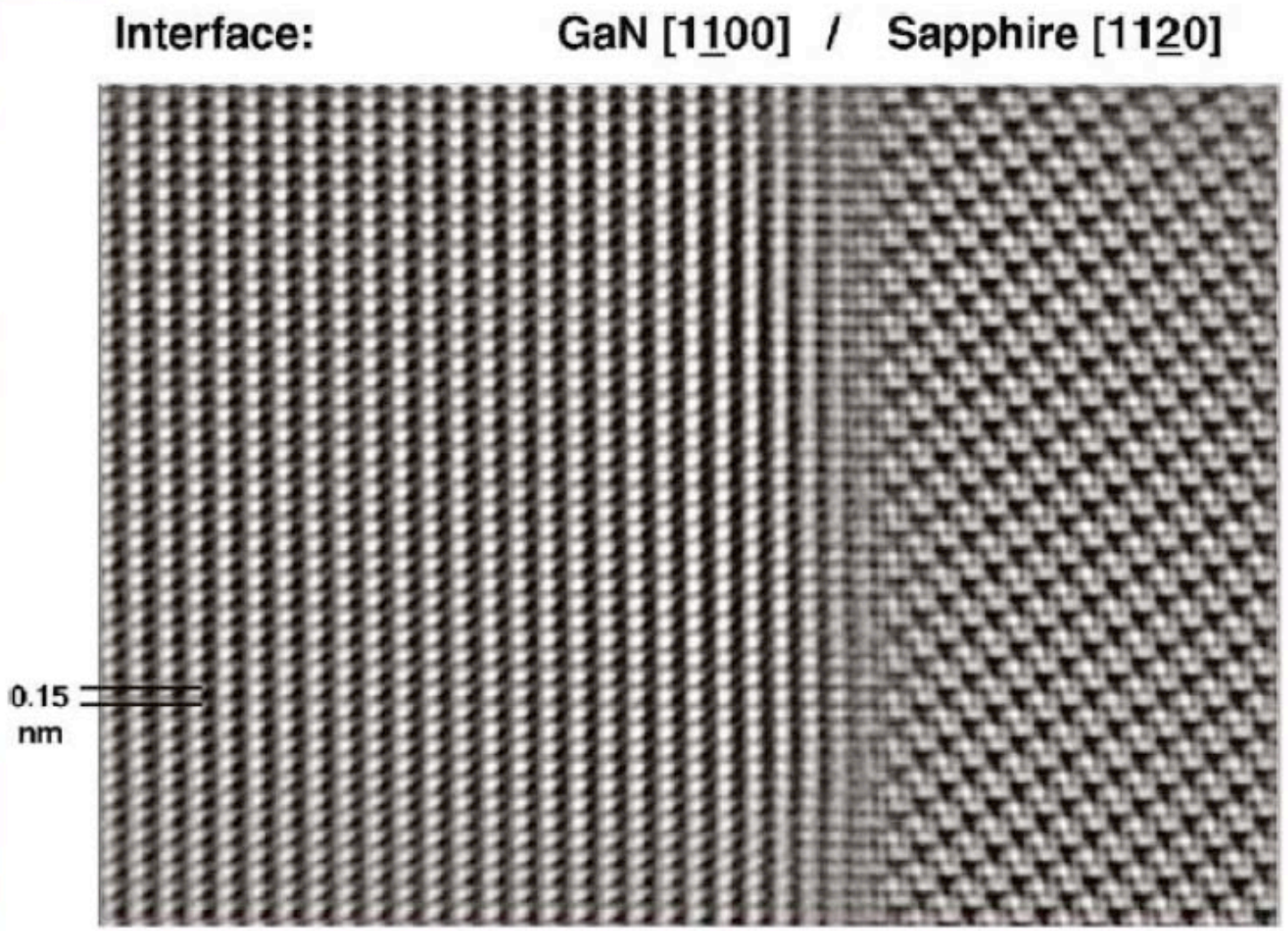

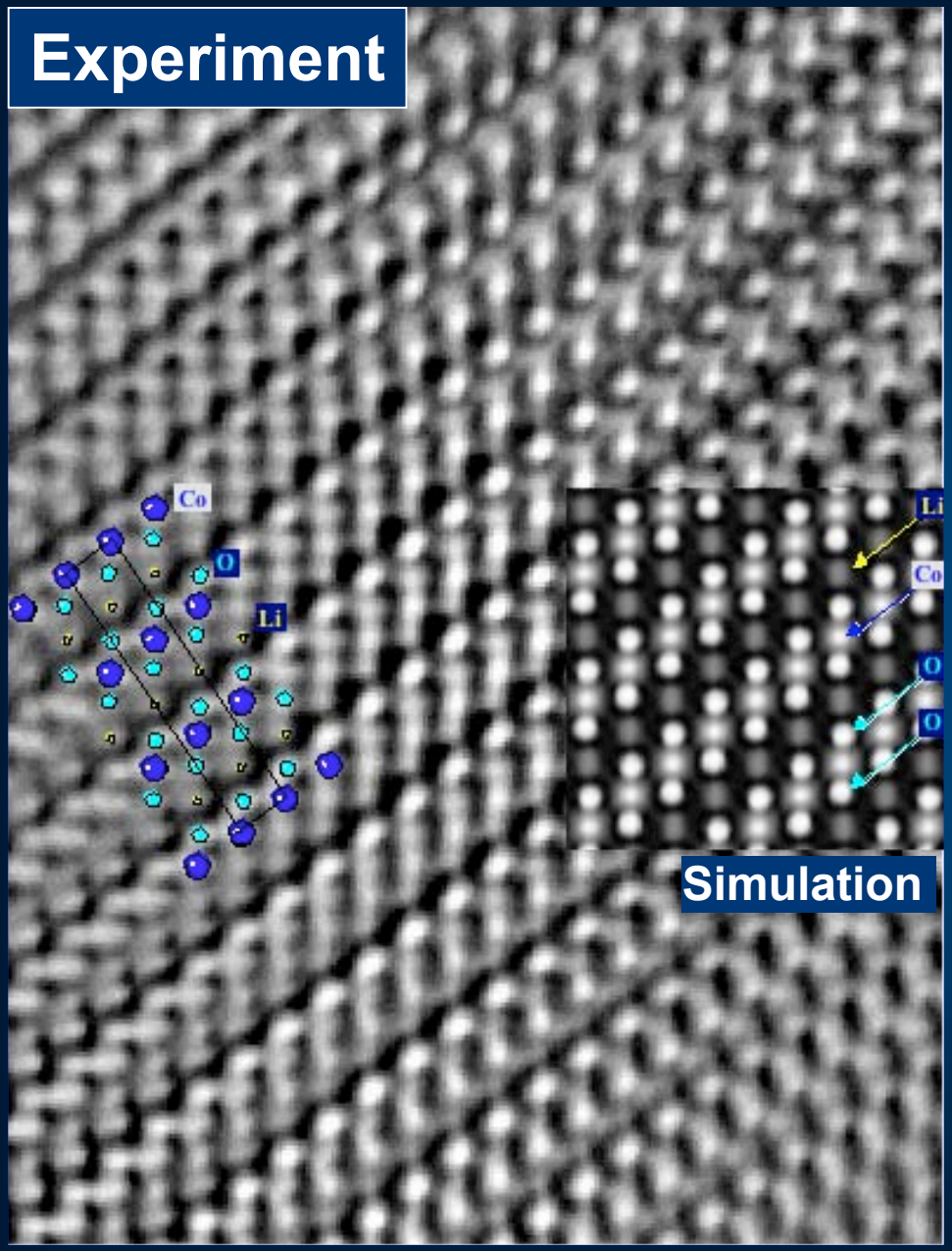

OÅM Image of LiCoO2 shows lithium atoms

Comparison of simulated and experimental ESWs shows that Li atom columns are visible at 0.9Å resolution in the OÅM.

O is strong
Co is "fuzzy"
Li is weak

The reconstructed exit-surface wave shows that the specimen is tilted away from exact [110] zone axis orientation and also reveals buckling and possible electron beam damage.

"Sub-Ångstrom Atomic-Resolution Imaging from Heavy Atoms to Light Atoms", Michael A. O'Keefe & Yang Shao-Horn, *Microscopy & Microanalysis* **10** (2004) 86-95.

Information Delocalization

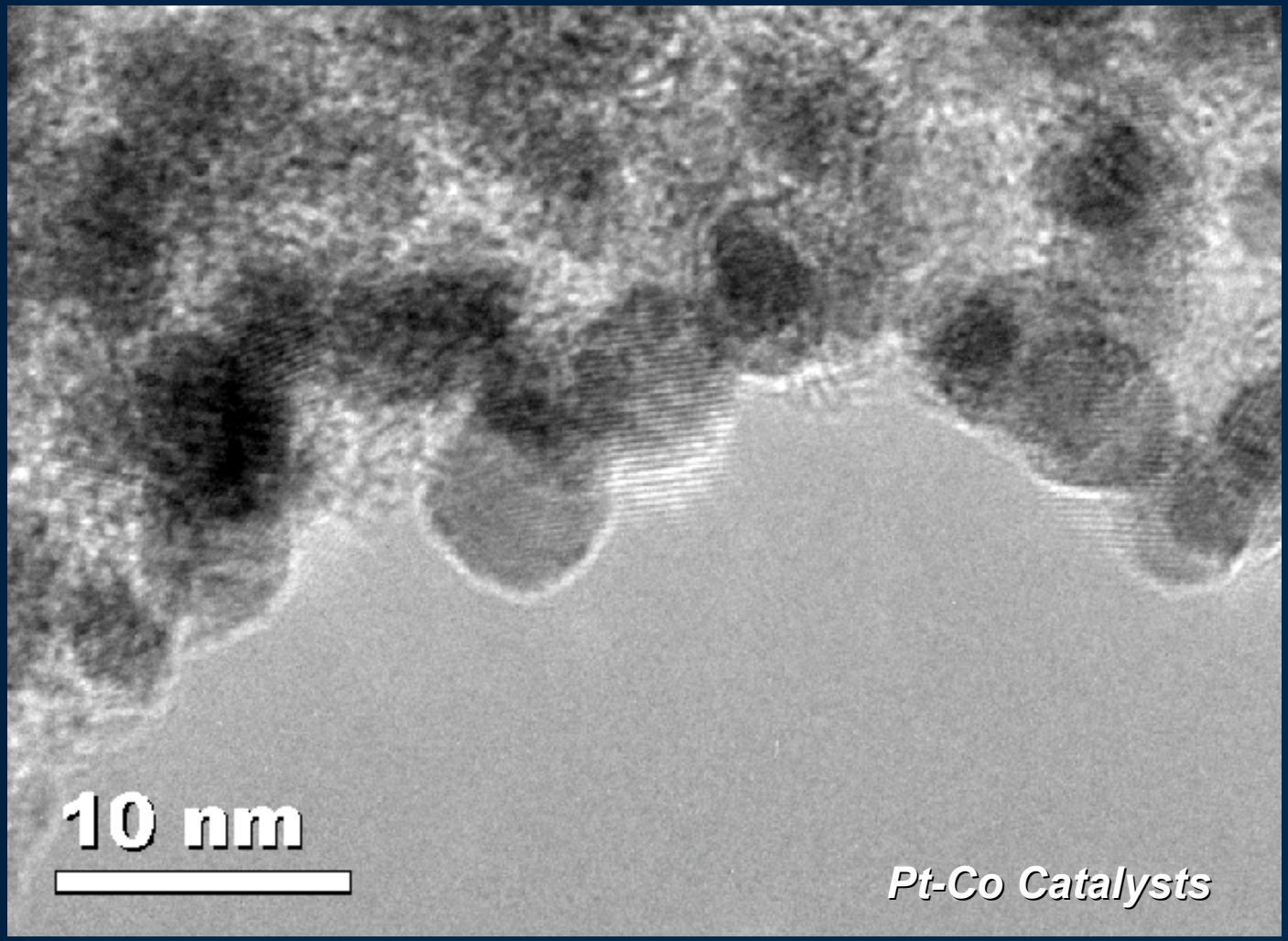

$$Delocalization : R = | C_5 \lambda^5 g^5 + C_3 \lambda^3 g^3 + \lambda \Delta f g |_{max}$$

What are the limitations in HREM ?

Aberrations

- Spherical
- Chromatic

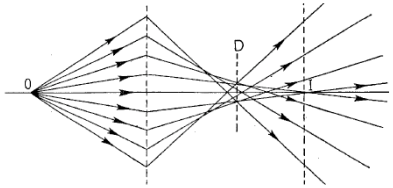

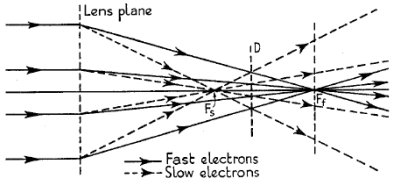

$$r_{sph} = C_s \beta^3$$

$$r_{chr} = C_c \frac{\Delta E}{E} \beta$$

The source and solution to "resolution limitations" has been known for nearly 50 years

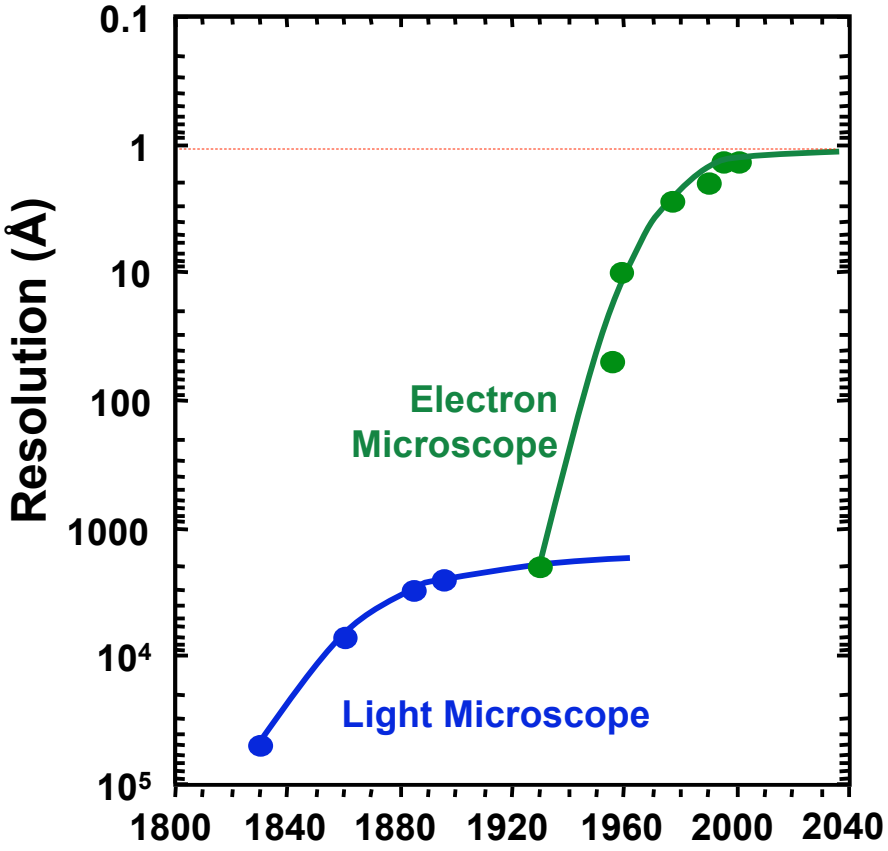

Challenge #1 : High Resolution Imaging
Requirements: ~ 0.1 nm, 0.1 na , 0.1 eV

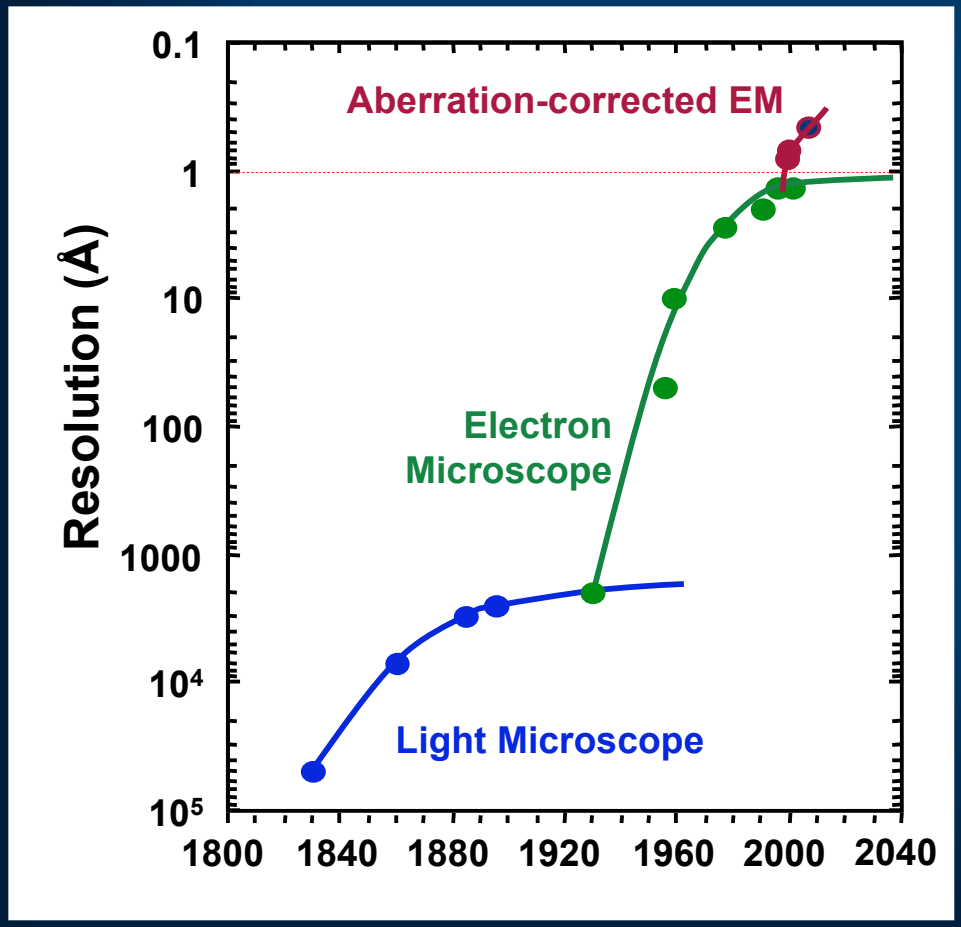

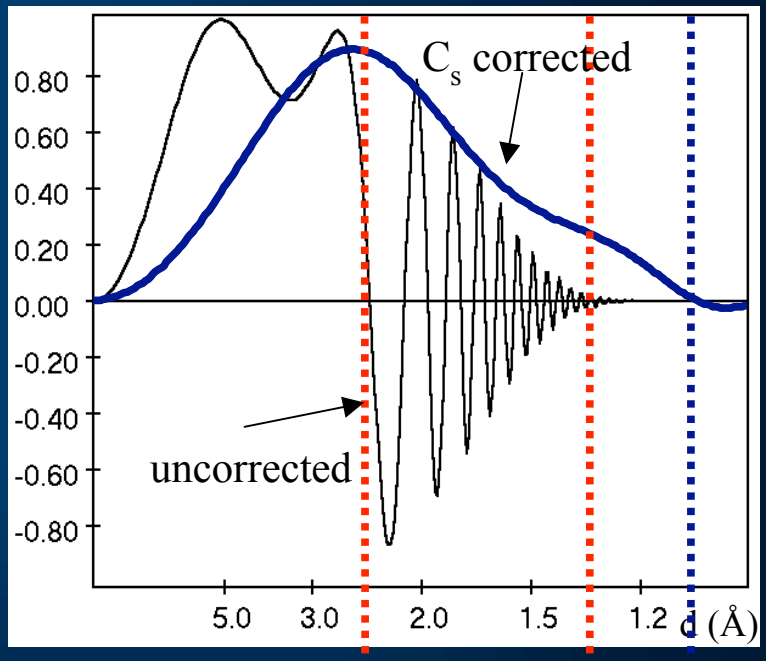

point res.

First Generation Corrected Instruments

Challenge #5 : *In-situ Liquid/Gaseous*

Requirements: *~0.1 nm, + ???*

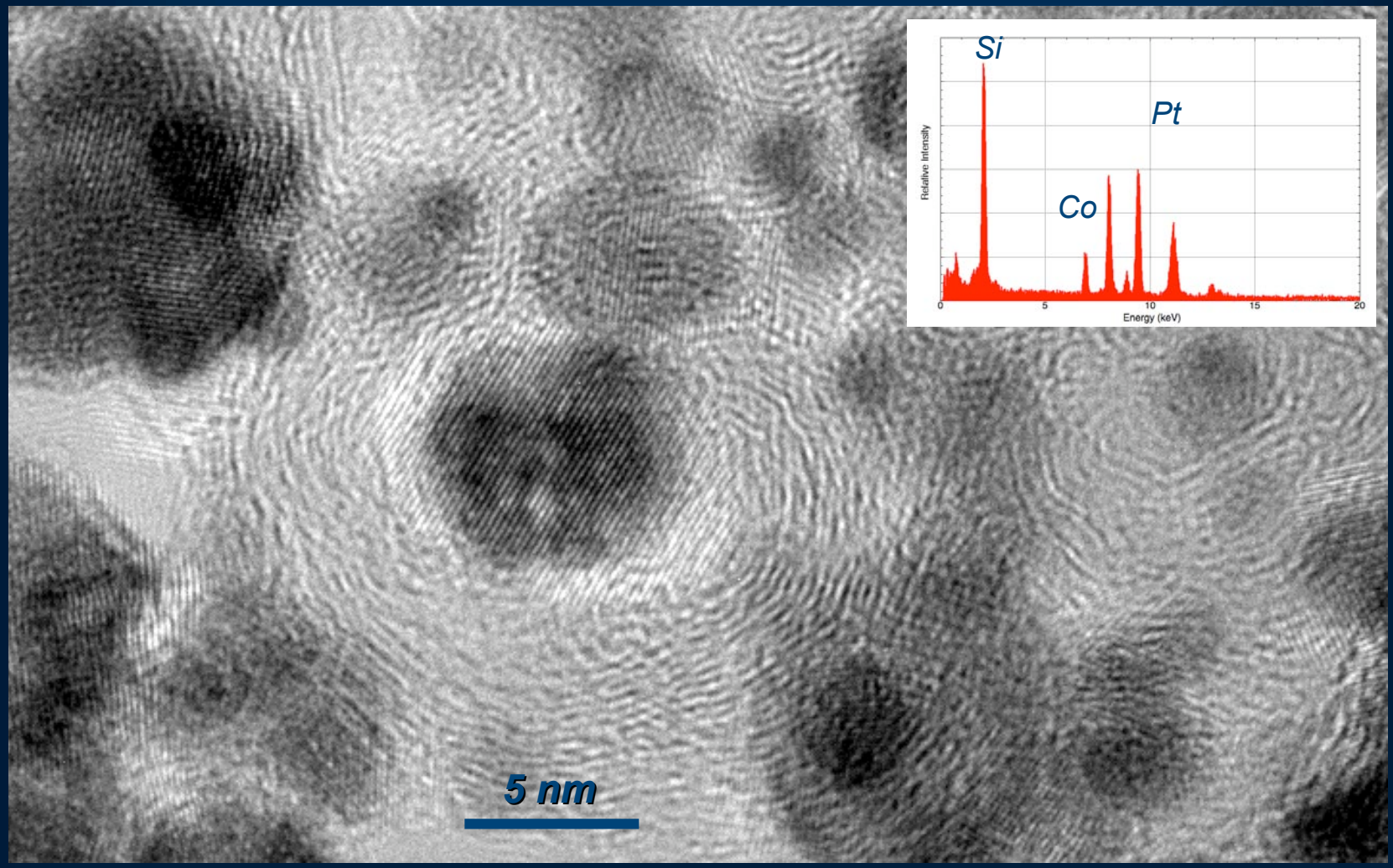

C_S Correction is Phase Correction

- To get information beyond Scherzer resolution requires a “correction” of the phase changes introduced by spherical aberration.
- Correction may be by hardware, or by software such as focal-series reconstruction of the exit-surface wave.
- Early focal-series reconstruction methods used simple linear combinations of image intensities at different spatial frequencies to correct for spherical aberration and extend microscope resolution.
- Aberration correction from a five-member focal series improved the resolution of a JEOL ARM-1000 from 1.6Å resolution to 1.38Å and allowed the oxygen atoms in staurolite to become visible [8].

[8] “Resolution of oxygen atoms in staurolite by three-dimensional transmission electron microscopy", Kenneth H. Downing, Hu Meisheng, Hans-Rudolf Wenk, Michael A. O'Keefe, *Nature* **348** (1990) 525.

HR-TEM on Gate oxide at 300kV

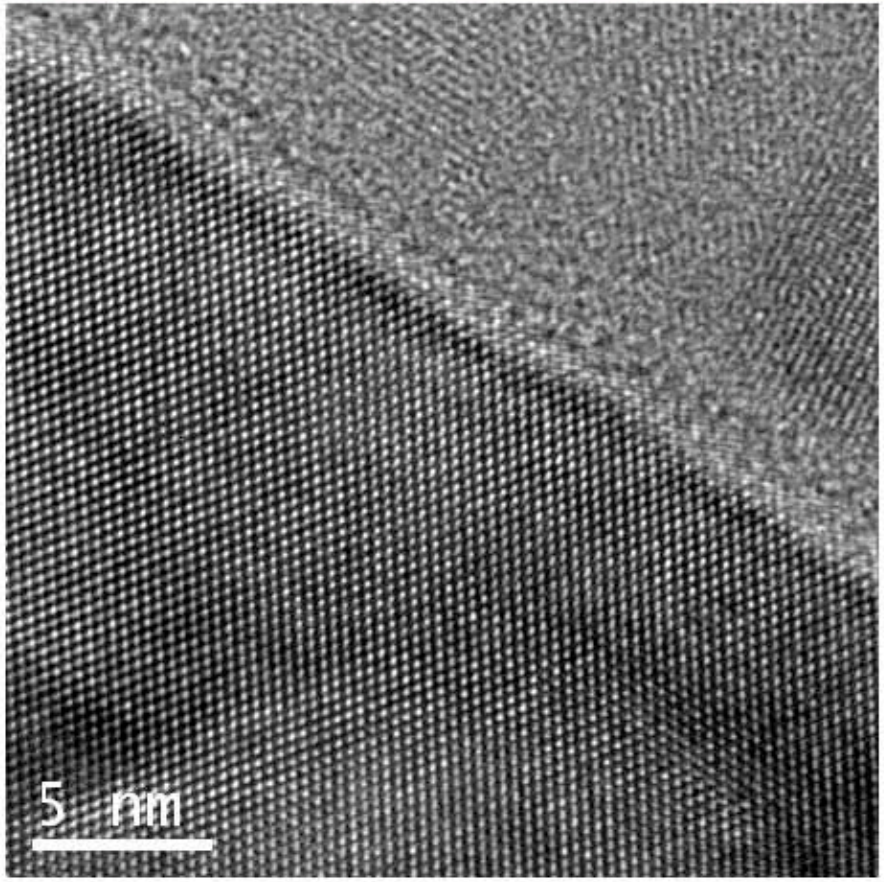

Images : B.Freitag

Cs –corrected HR-TEM and non Cs-corected HR-TEM images on the same area at 300kV

What Limits the ability to form a small probe?

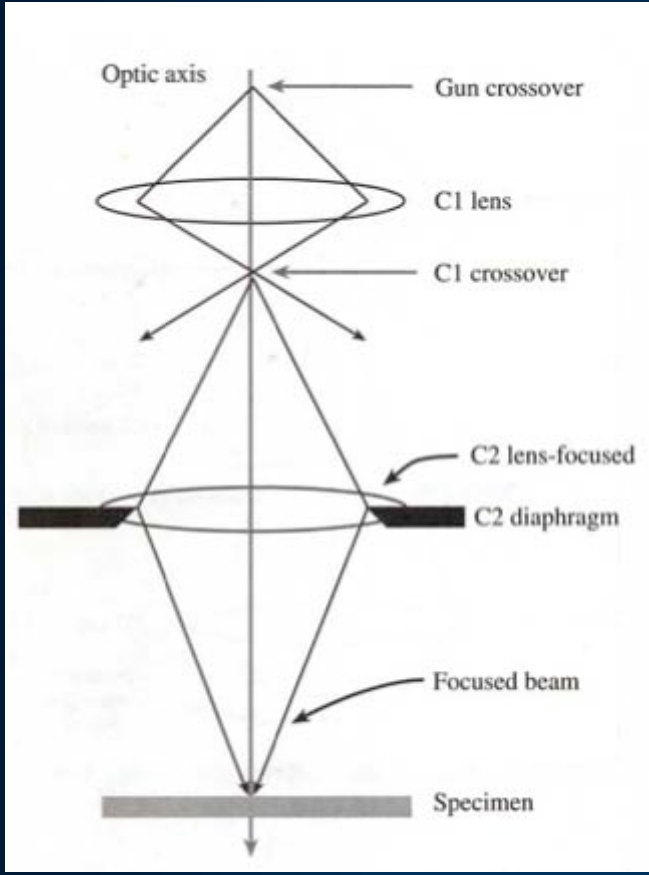

Aberrations

- Spherical

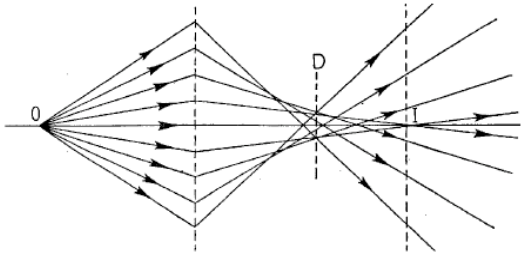

$$r_{sph} = C_s \beta^3$$

- Chromatic

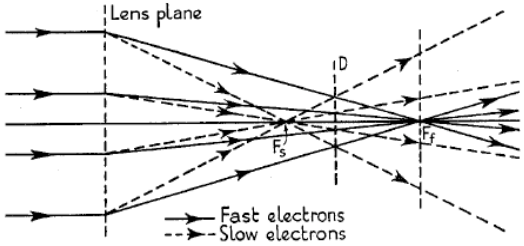

$$r_{chr} = C_c \frac{\Delta E}{E} \beta$$

Lens Aberrations

STEM Images

In a STEM the scattered electrons fall onto the ADF detector. This gives rise to a fundamental difference between the TEM and STEM DF modes:

- DF TEM images are usually formed by permitting only a fraction of scattered electrons to enter the objective aperture.
- STEM images are formed by collecting most of the scattered electrons on the ADF. Therefore, STEM ADF images are less noisy than TEM DF images.
- Because lenses aren't used to form the STEM image, the ADF images don't suffer aberrations (chromatic, spherical aberrations, for instance), as would the equivalent off-axis TEM DF image.
- STEM images generally only show better resolution than TEM images when thick specimens are being imaged. This is because the chromatic aberration effects from thicker specimens do not affect the STEM images.
- If contrast is more important than resolution, then a STEM is more useful. Indeed, in a STEM, you can study unstained polymer specimens which would show negligible contrast in a TEM.

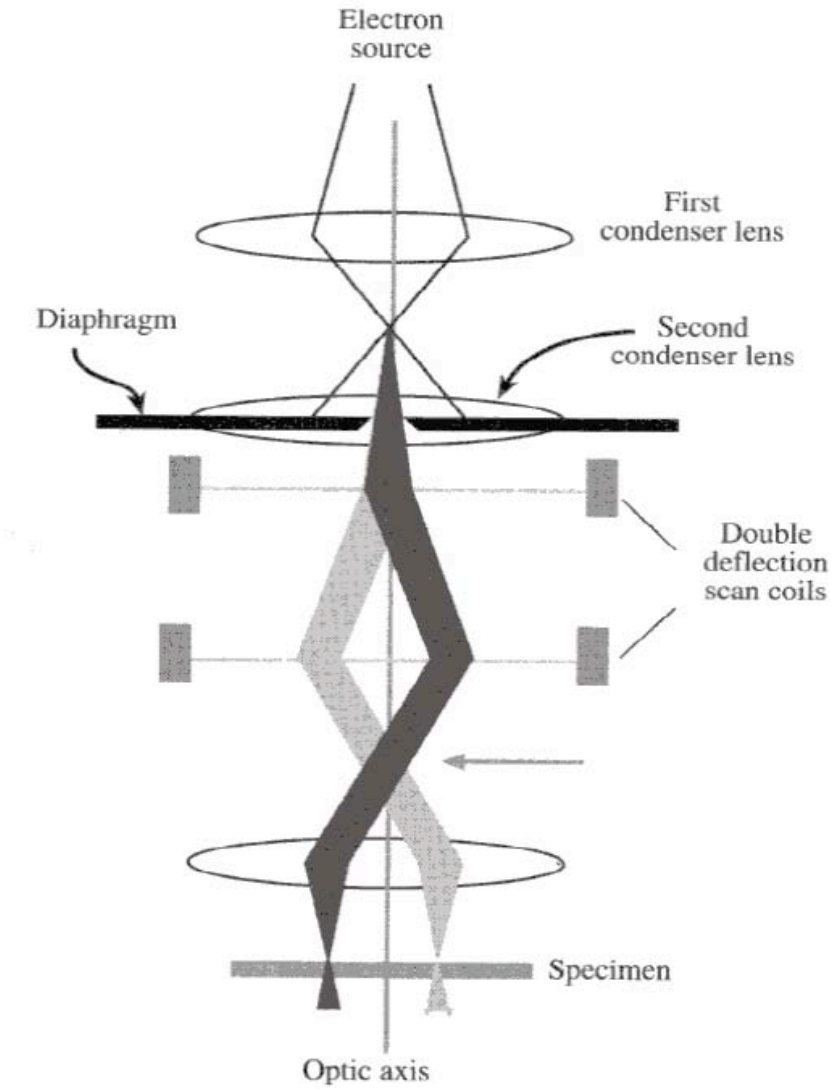

Figure 9.15. Scanning the convergent probe for STEM image formation using two pairs of scan coils between the C2 lens (usually switched off) and the upper objective polepiece. The probe remains parallel to the optic axis as it scans.

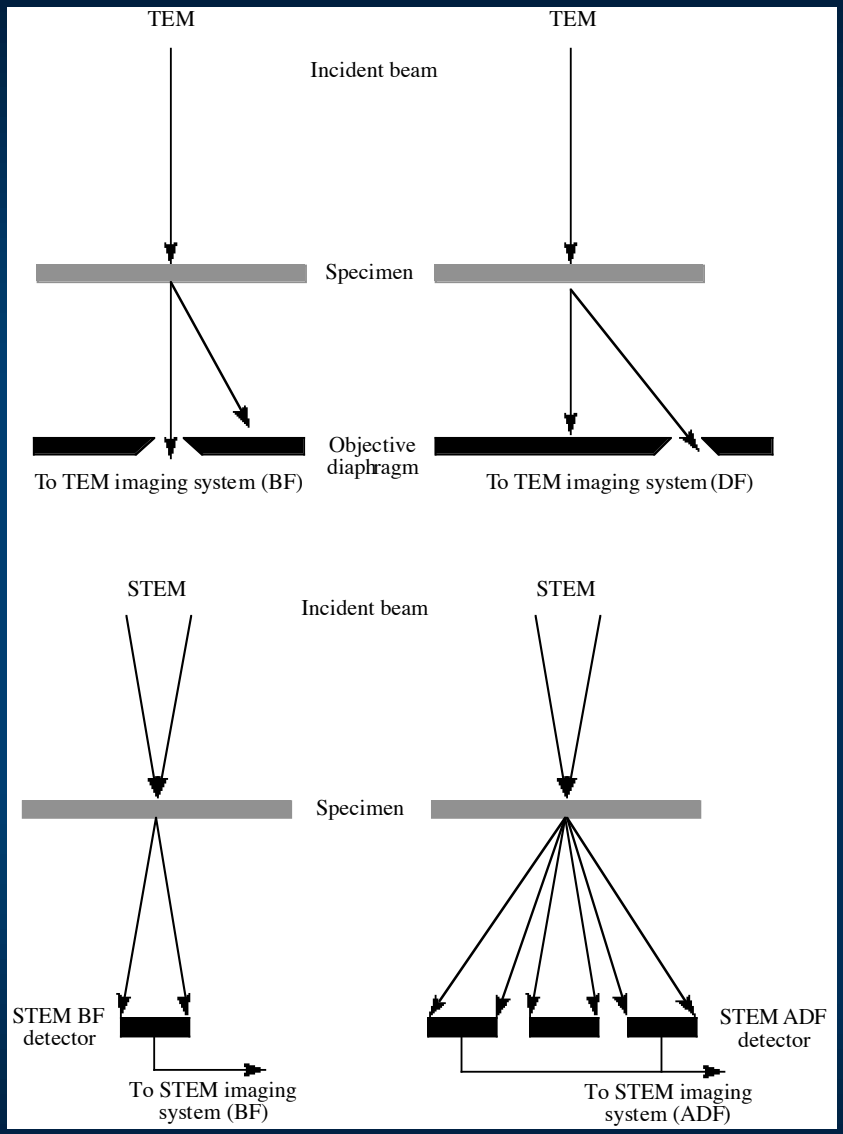
TEM
TEM
Incident beam
Specimen
Objective diaphragm
To TEM imaging system (BF)
To TEM imaging system (DF)
STEM
STEM
Incident beam
Specimen
STEM BF detector
STEM ADF detector
To STEM imaging system (BF)
To STEM imaging system (ADF)

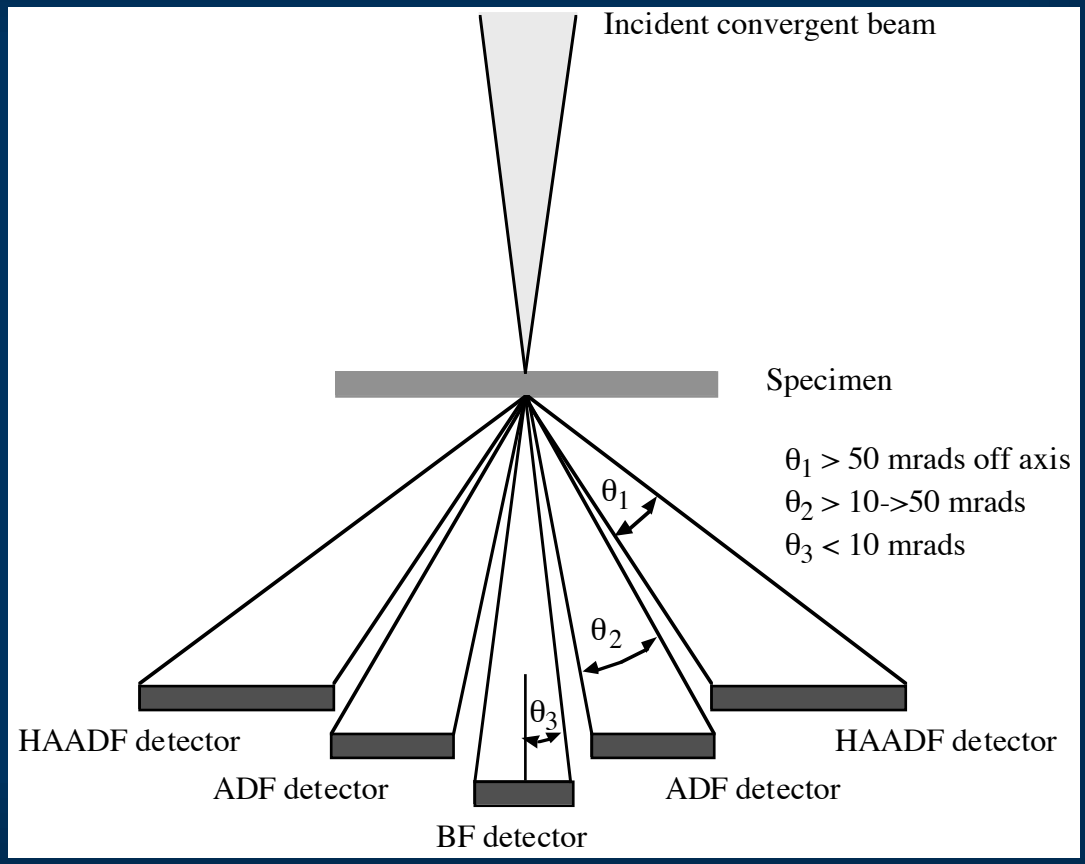
Incident convergent beam
Specimen
θ1 > 50 mrads off axis
θ2 > 10->50 mrads
θ3 < 10 mrads
θ1
θ2
θ3
HAADF detector
HAADF detector
ADF detector
ADF detector
BF detector

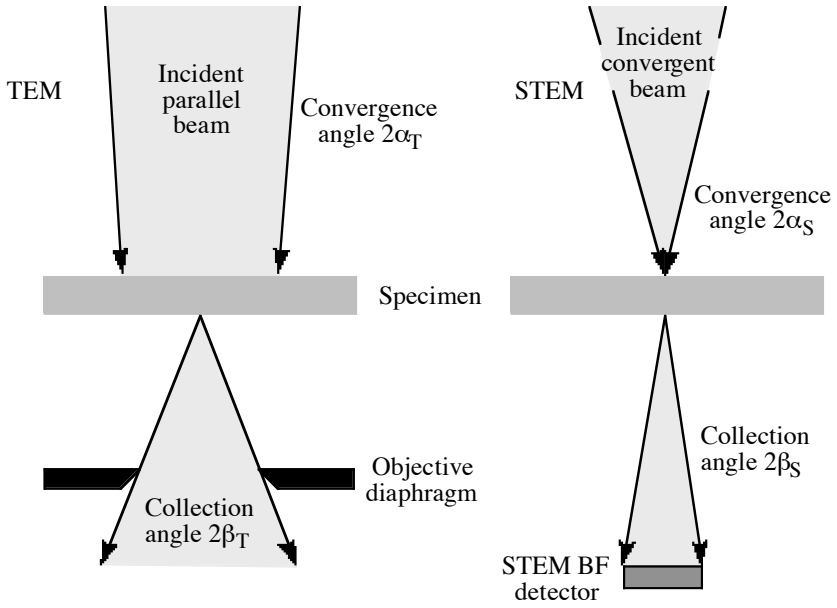

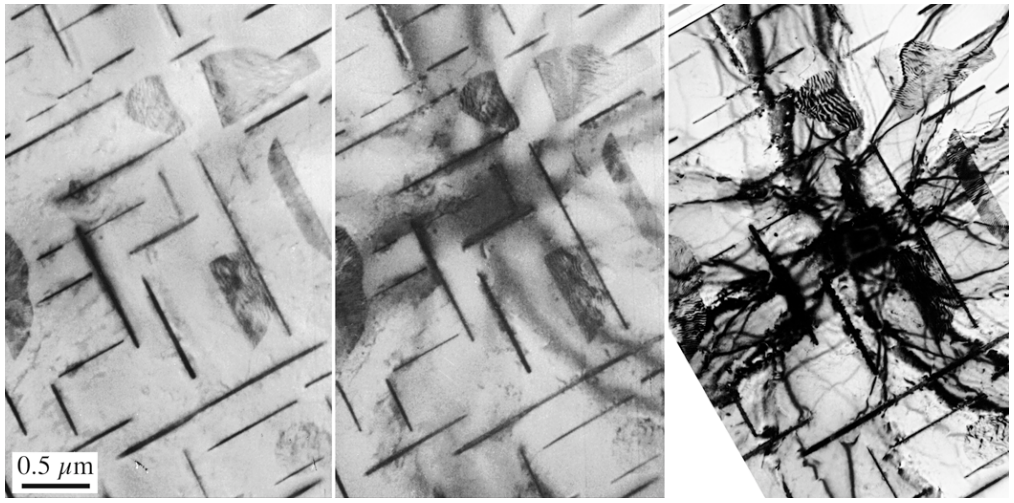

Regular STEM

STEM with smaller β

TEM

Z Contrast Image

- The method of Z-contrast imaging utilizes a post-specimen annular detector. This arrangement results in desirable effects in connection with the image contrast for crystalline specimens orientated close to their zone axes, or for small particles comprising elements of high atomic number. Many technologically interesting problems involve the interfaces and defects of such crystals and the knowledge of the size, spatial distribution and composition of such particles. Here, the Z-contrast image has important advantages over other image types. Intensities are easier to interpret in terms of the physical specimen structure and they are approximately proportional to the square of the atomic number (Z) of the elements present in each part of the specimen. Also, resolution approaches twice that of a bright-field phase-contrast image. The technique can be performed in parallel with other analytical experiments that yield complementary structural information.

The Rutherford scattering cross section for deflection through an angle greater than ϕ may be written [5]

$$\sigma(\phi) = 1.62 \times 10^{-14} \frac{Z^2}{E_0^2} \cot^2\left(\frac{\phi}{2}\right) \qquad (2.7)$$

Schematic of the HAADF detector set-up for Z contrast imaging in a STEM.

- The detector is called a high-angle ADF or HAADF detector.
- Z-contrast images are also termed HAADF images.

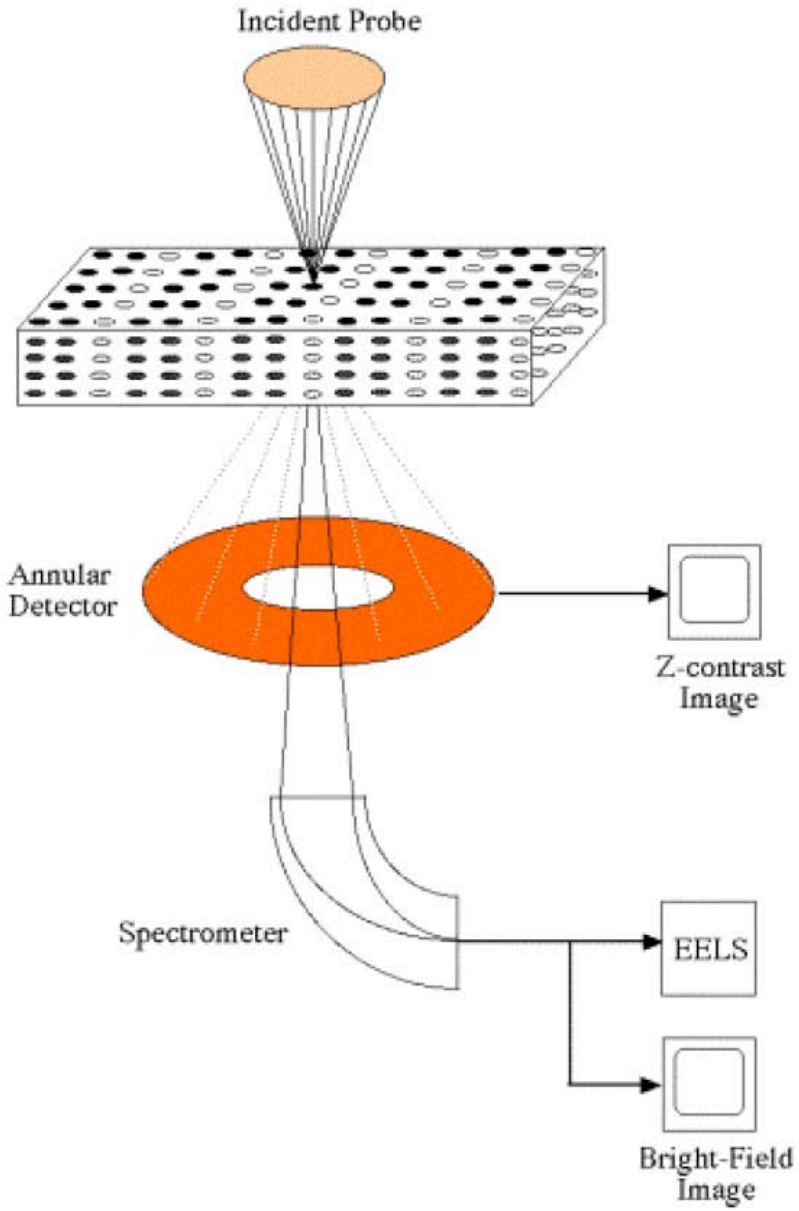

Alternative Fabrication: Nano Arrays with 1.4 nm NanoGold

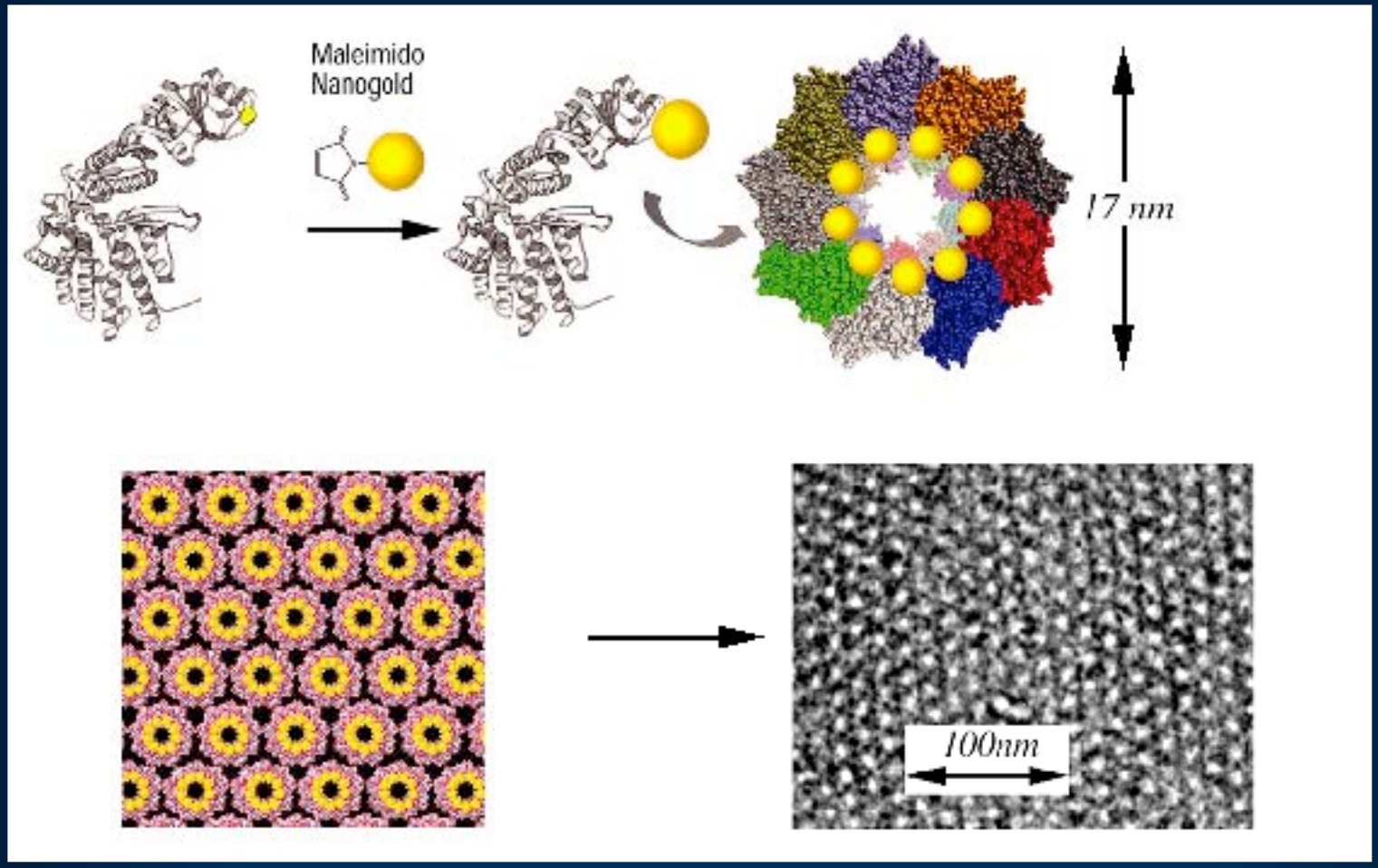

1. **covalent attachment of nanogold to subunits**
2. **self-assembly into rings**
3. **assembly into rings**

HAADF
&
XEDS
Identify Au

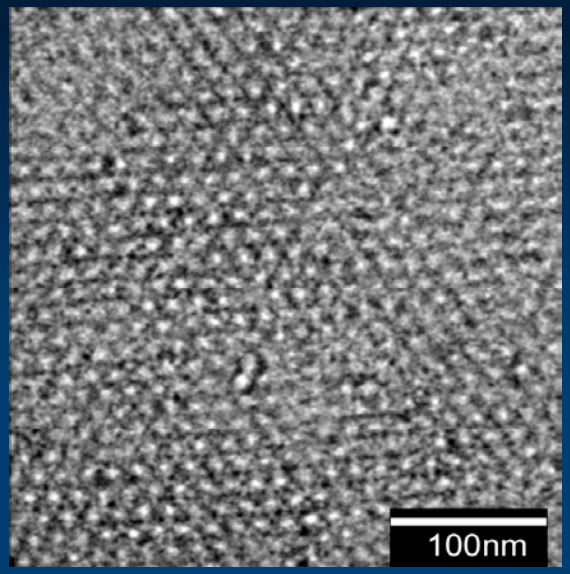

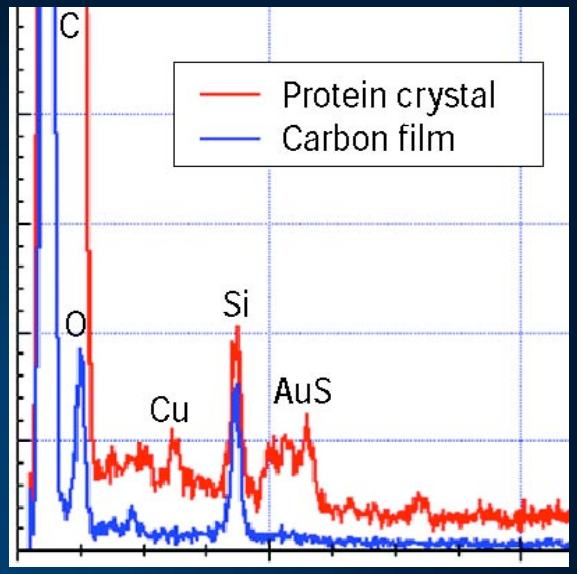

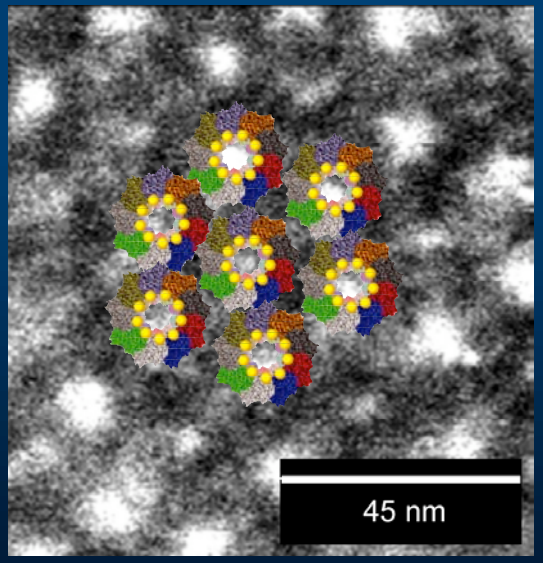

Nano Array

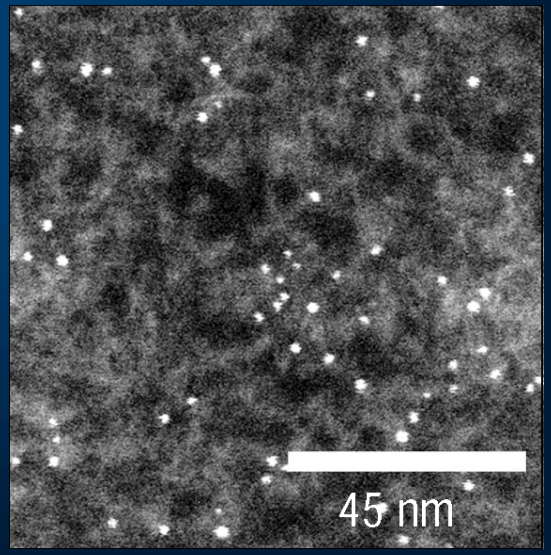

Isolated NanoAu

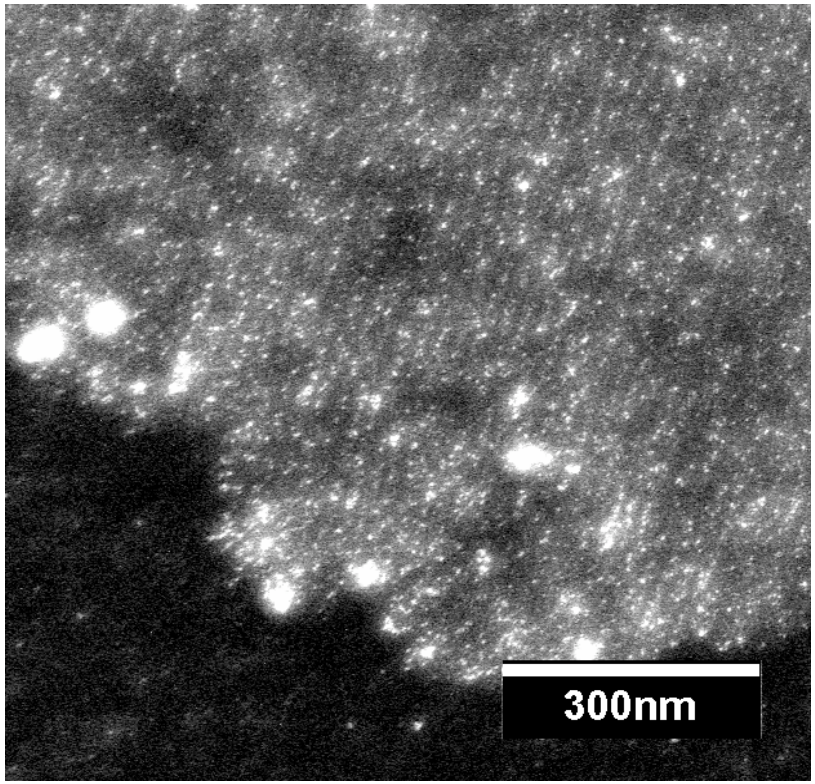
300nm

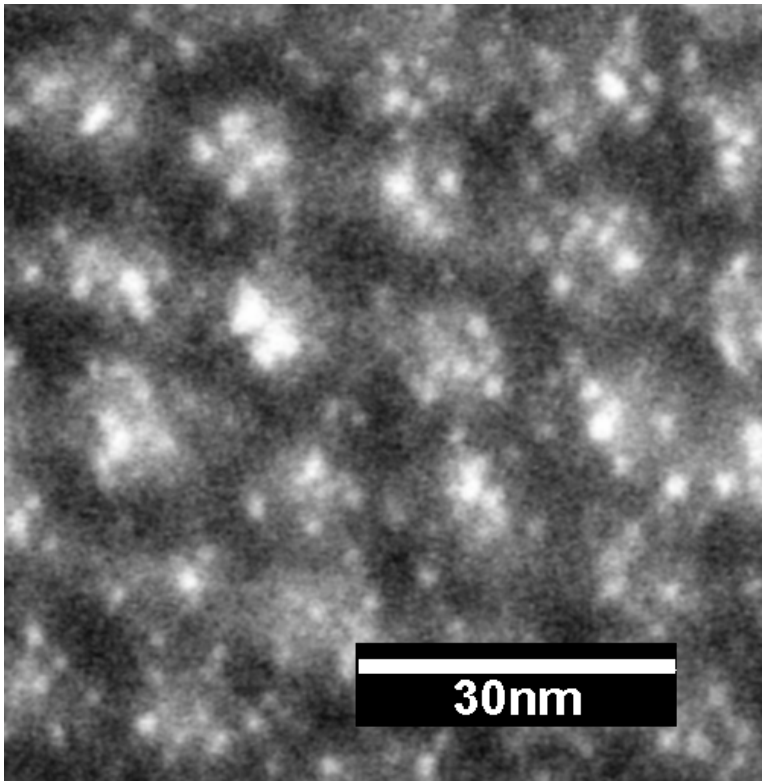
30nm

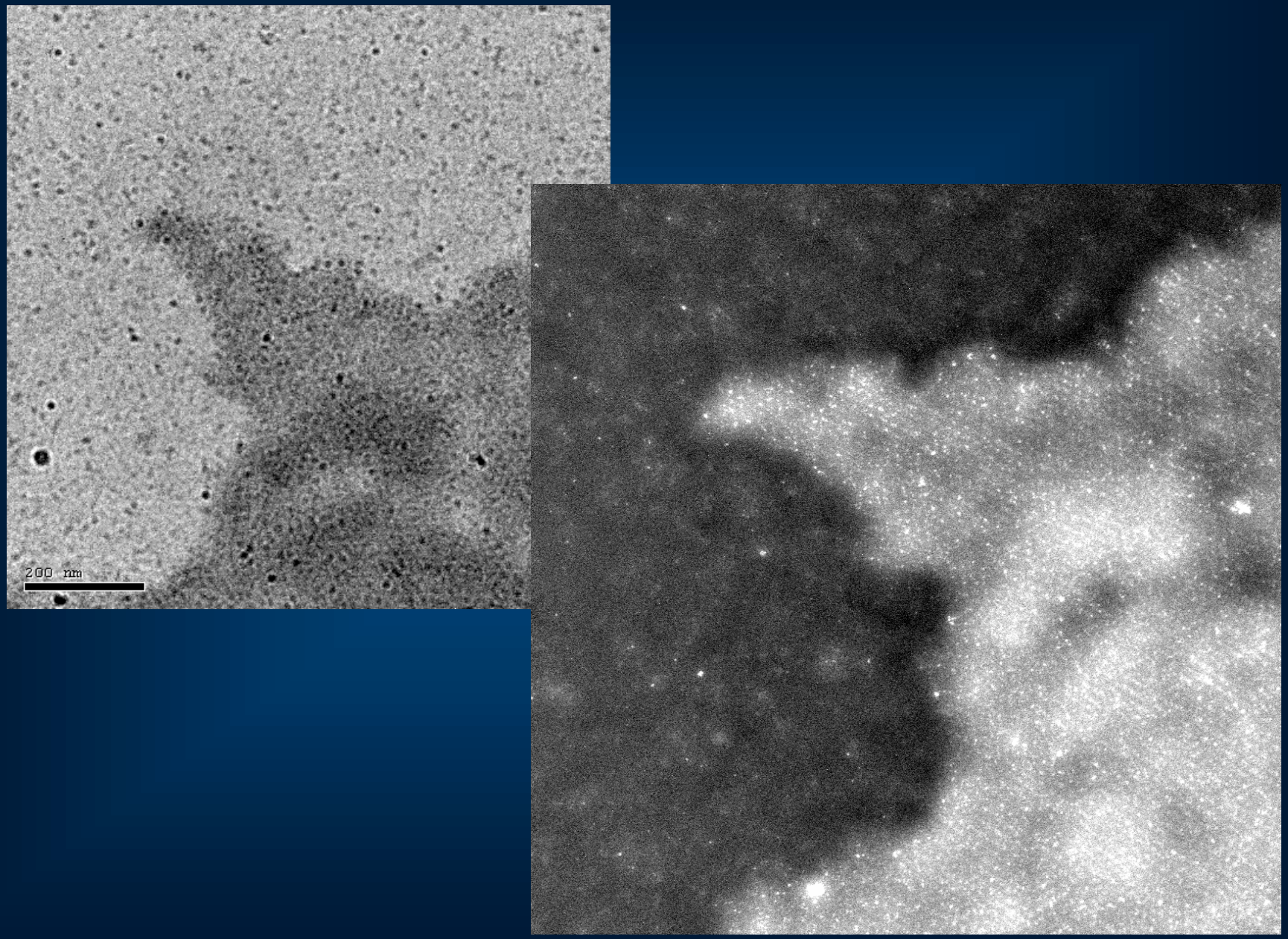
200 nm

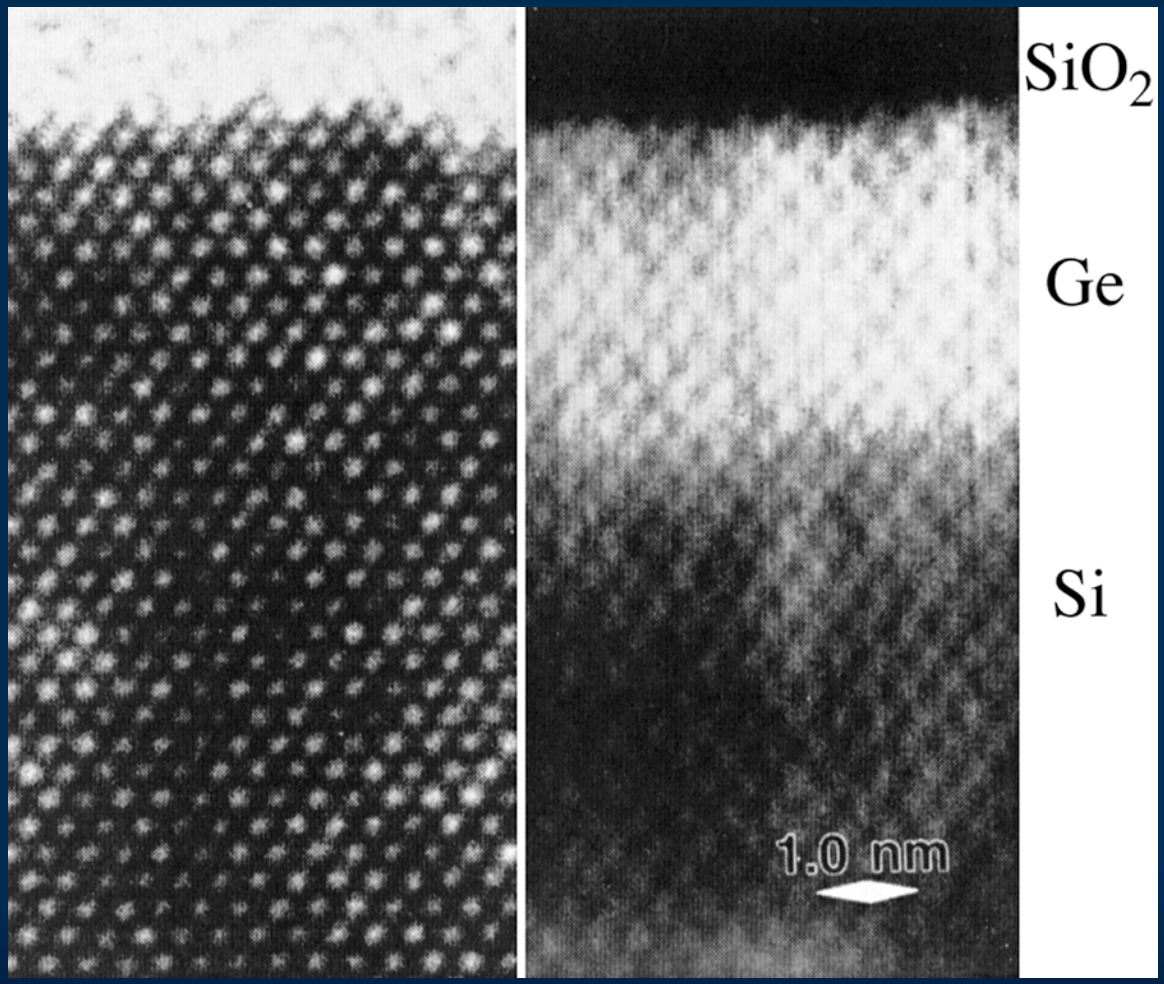
SiO_2
Ge
Si
1.0 nm

What are the Limits - Today?

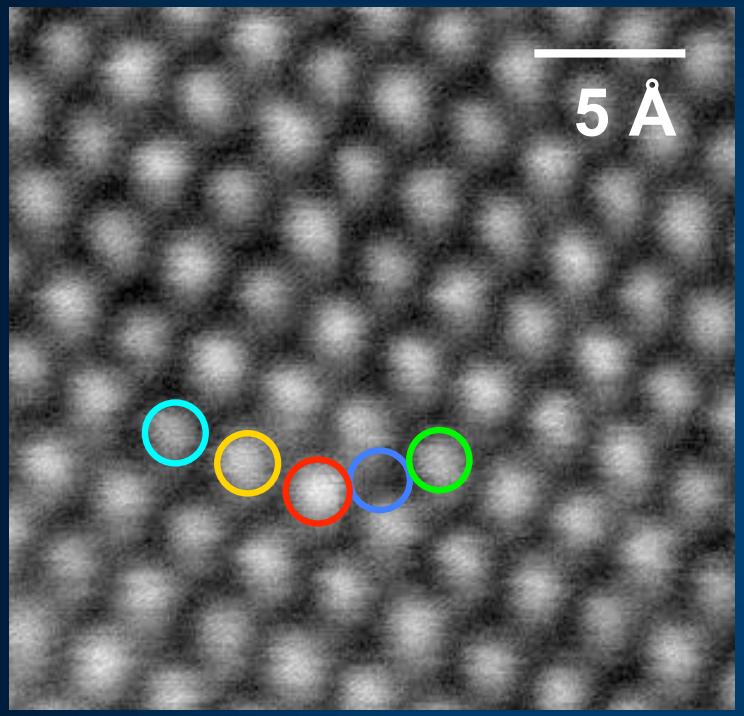

La in $CaTiO_3$ grown by MBE

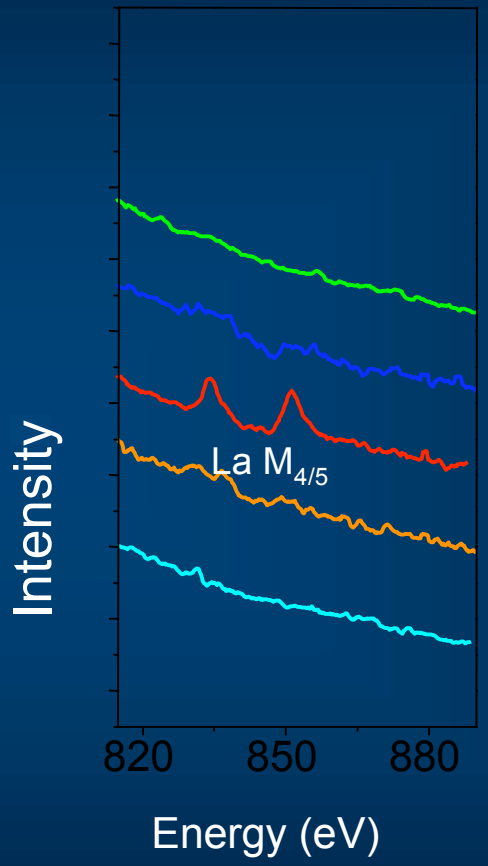

Spectroscopic identification at subnanometer resolution.

8% collection efficiency

S. Pennycook from the TEAM Project Report

Scanning Confocal Electron Microscopy
Depth Profiling

Aberration-correction allows for larger probe-forming aperture angles.As aperture angle increases, probe width decreases. Moreover "depth of focus"decreases, and even more rapidly.

By varying defocus, in additional to usual 2D raster scan, could now scan in 3D.Can still measure several signals simultaneously.